SPECTRUM-DEPENDENT PHOTOVOLTAIC ENERGY HARVESTING

by

Alan S. Teran

A dissertation submitted in partial fulfillment
of the requirements for the degree of
Doctor of Philosophy
(Electrical Engineering)
in The University of Michigan
2016

Doctoral Committee:

Professor Jamie D. Phillips, Chair
Professor David Blaauw
Professor Jay Guo
Professor Joanna Mirecki-Millunchick

To my parents.

ACKNOWLEDGMENTS

First and foremost, I would like to thank my research advisor, Professor Jamie Phillips, for giving me the opportunity to work alongside him throughout my career as a graduate student at the University of Michigan. I could not have had a better guide and mentor. From the day I met him he always treated me with respect and made sure I knew the door to his office would always be open for me. He provided tremendous inspiration for my research and helped me grasp the impact of my work. I am sincerely thankful for the encouragement and support he provided.

I would also like to acknowledge Professor David Blaauw, Professor Jay Guo, and Professor Joanna Mirecki-Millunchick for devoting significant time serving on my committee. My research work could not have been done without their feedback and guidance. It has been a priveledge collaborating with them.

Next, I would like to thank Professor Antonio Martí Vega for letting me spend time with him and his group at the Instituto de Energía Solar, Universidad Politécnica de Madrid. Professor Martí provided immesurable support and inspiration for my research work. I would also like to thank Estela Hernández Martín, Esther López Estrada, Iñigo Ramiro González, Irene Artacho, and David Fuertes Marrón for all of your help during my time in Madrid.

I would also like to thank the past and present members of the Phillips group for their camaraderie and incredible support. In particular, I would like to thank Dr. Chihyu

Chen, Dr. Justin Foley, and Dr. Jinyoung Hwang for their great mentorship. In addition, I would like to thank Connor Field, Eun Seong Moon, and Justin Easley for their insightful feedback.

Next, I would like to acknowledge the past and present members of the Bhattacharya group for their help and useful discussions. In particular, I would like to thank Bo Xiao, Dr. Saniya Deshpande, Dr. Sishir Bhowmick, Dr. Animesh Banerjee, Dr. Shafat Jahangir, Zunaid Baten, Thomas Frost, and Arnab Hazari. It has been a priveledge having them as collegues.

I would also like to acknowledge past and present members of the Blaauw, Guo, and Millunchick group. In particular, I would like to acknowledge Dr. Yoonmyung Lee, Dr. Inhee Lee, Dr. Gyouho Kim, and Wootaek Lim from the Blaauw group, Suneel Joglekar from the Guo group, and Matt Dejarld from the Millunchick group. They all provided incredible help towards my research work.

Next, I would like to thank the members of the Lurie Nanofabrication Facility for their help and insight. In addition, I would like to thank the members of the LNF User Committee for the useful discussions. The staff and users of the LNF provided a great working environment and collegial atmosphere.

I would also like to take this opportunity to thank my wonderful friends who have provided immesurable support throughout my time living in Ann Arbor. The memories they have helped me create will always fill me with joy.

Finally, my deepest gratitude goes to my loving family for their encouragement and love. Despite the distance, I always felt the support of my parents, siblings, and wife. I am sincerely thankful for the opportunities they have given me to succeed in all aspects of my life.

TABLE OF CONTENTS

LIST OF FIGURES

Figure

LIST OF TABLES

Table

ABSTRACT

Spectrum-Dependent Photovoltaic Energy Harvesting

by

Alan S. Teran

Chair: Jamie D. Phillips

Solar cells have garnered a lot of attention due to the rising cost of fossil fuels and the increasing global demand for renewable sources of energy. Heterojunctions based on II-VI materials can be used to increase the efficiency of multi-junction solar cells, and may also offer the opportunity to realize next generation approaches such as the intermediate-band solar cell (IBSC) based on highly-mismatched alloys or quantum dots. One material of particular interest is ZnTe:O where IB solar energy conversion has been demonstrated. Efficient doping in many II-VI materials, however, is often a major obstacle to achieving high-quality junction diodes. ZnTe is no exception, where efficient p-type doping is possible, but n-type doping is difficult to obtain. In this work, studies of n-ZnSe/p-ZnTe heterojunction solar cells grown by molecular beam epitaxy will be reported. Limitations on the open-circuit voltage of p-ZnTe/n-ZnSe heterojunction solar cells are studied via current-voltage (I-V) measurements under solar concentration and at variable temperature. The open-circuit voltage reaches a maximum value of 1.95 V at 77 K and 199 suns. The open-circuit voltage shows good agreement with the calculated built-in potential of 2.00 V at 77 K. These results suggest that the open-circuit voltage is limited

by heterojunction band offsets associated with the type-II heterojunction band lineup, rather than the bandgap energy of the ZnTe absorber material.

In addition to outdoor applications, indoor photovoltaic energy harvesting is a promising candidate to power millimeter (mm)-scale systems. Low-power photovoltaic energy harvesting allows for the deployment of fully autonomous small-scale sensors in environments not previously possible. Indoor lighting is one of those environments where the illumination intensity is typically below 1,000 lx and the spectrum is narrowly centered in the visible region. These conditions differ vastly from traditional solar cell testing conditions that have illumination intensities greater than 10,000 lx and contain significant ultraviolet and infrared light. Photovoltaics based on III-V compounds provide an outstanding choice for indoor lighting conditions due to their superior absorption, carrier transport, and corresponding high quantum efficiency in the visible spectrum. The theoretical efficiency and electrical performance of photovoltaics under typical indoor lighting conditions are analyzed. Commercial crystalline Si, amorphous Si, and fabricated GaAs and $Al_{0.2}Ga_{0.8}As$ photovoltaic cells were experimentally measured under simulated AM 1.5 solar irradiation and indoor illumination conditions using a white phosphor light-emitting diode to study the effects of input spectra and illuminance on performance. The $Al_{0.2}Ga_{0.8}As$ cells demonstrated the highest performance with a power conversion efficiency of 21%, with open0circuit voltages >0.65 V under low lighting conditions. The GaAs and $Al_{0.2}Ga_{0.8}As$ cells each provided a power density of ~100 nW/mm^2 or more at 250 lx, sufficient for the perpetual operation of present-day low-power mm-scale wireless sensor nodes. The path for achieving large light harvesting efficiencies will be discussed as well as the implementation of these photovoltaic cells for mm-scale sensing applications.

Chapter I

Introduction

Traditional photovoltaic research has been mostly focused on improving the efficiency and reducing the cost of solar cells. These efforts have been tailored towards large-scale applications in order to increase the deployment of solar energy technology and further reduce our societies dependence on non-renewable sources of energy. The improvements in traditional solar photovoltaics have opened the door to new, unique, applications that require their own research and development efforts. One of these applications is the need for high efficiency photovoltaics deployed in unconventional environments and requiring unique form factors.

Photovoltaic energy harvesting is the process of converting light energy into electrical energy from different light sources. The type of light source can have drastic effects on photovoltaic device performance. This is due to the differences in spectral content and intensity of each light source. The following chapters analyzes the behavior of photovoltaic devices under different light sources and explores ways of improving device performance and efficiency for a given light source.

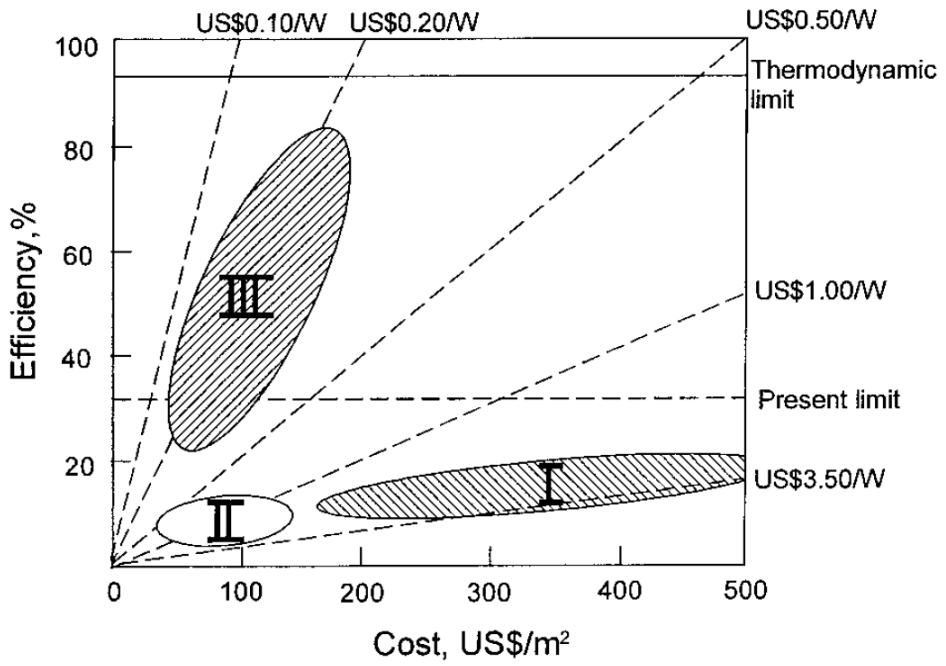

Figure 1.1. Efficiency and cost projections for photovoltaic technology (adopted from [1]).

1.1 Photovoltaics for Renewable Energy

In order to provide the lowest cost for electricity and to minimize the use of land area, higher efficiency solar cells are needed. Historically, there have been three generations of solar photovoltaic technology [1]. The first generation represents the matured Si solar cells that have been the staple of solar energy for many years. The second generation represents the thin-film technologies developed using low cost materials. The third generation represents advanced thin-film technologies that use novel photovoltaic physics to go beyond traditional efficiency limits. Figure 1.1 demonstrates the efficiency as a function of cost for the three generations of photovoltaic technology. Advances in the research and development of photovoltaic technology have led to a

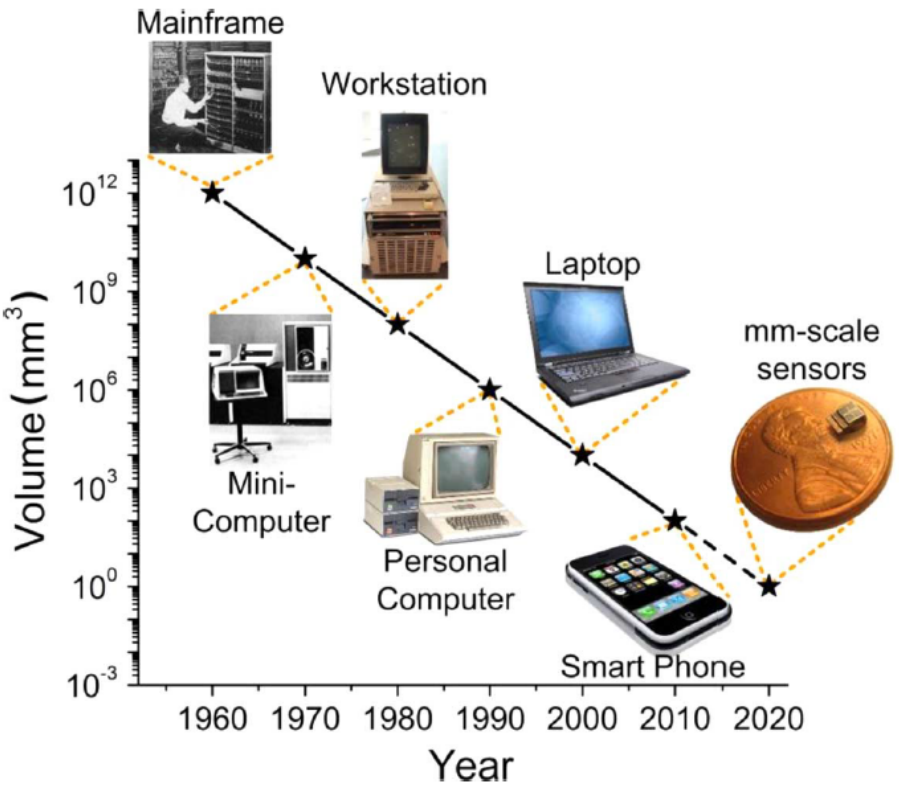

Figure 1.2. Bell's Law predicts the reduction in size of computing systems (adopted from [2]).

reduction in cost and an increase in efficiency. The research described in this thesis is part of the ongoing effort to improve third-generation photovoltaic technology.

1.2 Energy Harvesting for the Internet of Things

Computing systems have reduced in size exponentially with the development of low-power semiconductor technology. The scale of this reduction can be appreciated in Figure 1.2 which shows the logarithmic reduction in volume of computing systems with each decade. This trend is best known as Bell's Law and predicts a further reduction of all computing systems to the millimeter scale [2]. The advent of mm-scale computing

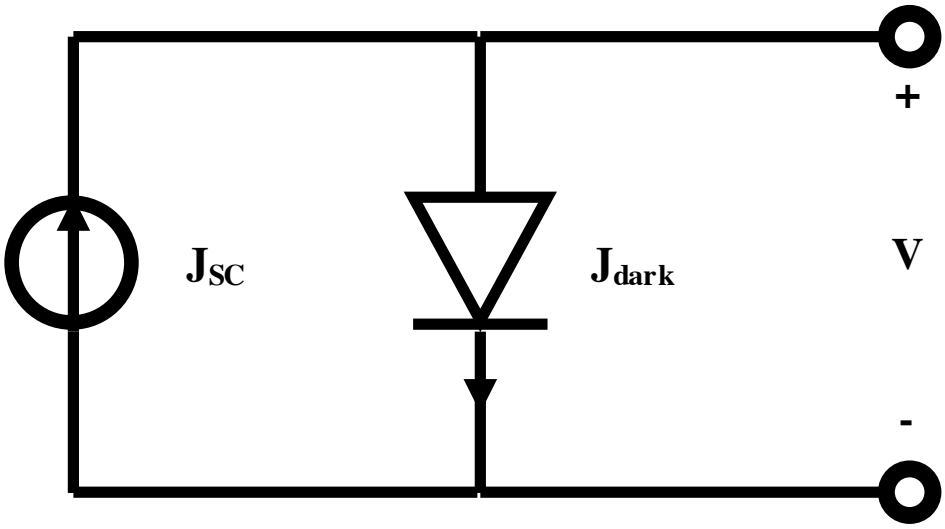

Figure 1.3. Equivalent circuit of an ideal photovoltaic cell.

systems allows for the development of the Internet of Things (IoT). The size of these systems forces researchers to consider new sources of energy for power requirements. As batteries shrink, more energy must be harvested from the environments these mm-scale systems are embedded in. Photovoltaic energy harvesting offers a possible solution.

1.3 Basic Characteristics of Photovoltaic Cells

Semiconductor photovoltaic devices are semiconductor diodes which have been optimized for light absorption, carrier separation, and carrier collection. The fundamental figures of merit for photovoltaic devices need to be understood in order to design them for optimal performance in a given environment. In the dark, diodes have a rectifying behavior which is described by the current density voltage relation

$$J_{dark}(V) = J_0 \left[\exp\left(\frac{qV}{kT}\right) - 1\right] \tag{1.1}$$

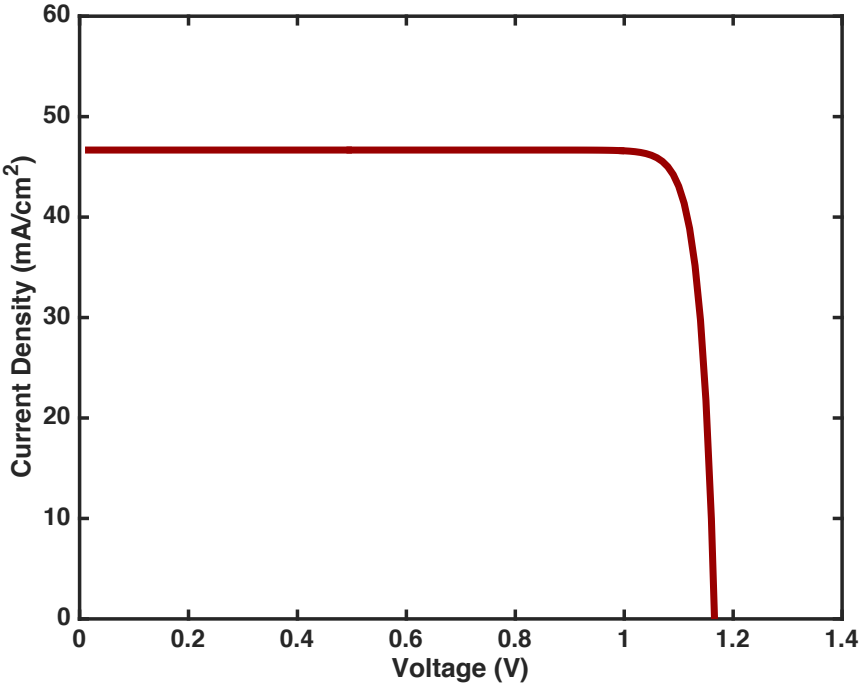

Figure 1.4. Photovoltaic response of an ideal diode exposed to light.

where J_{dark} is the dark current density, J_0 is the dark saturation current density, q is the electron charge, V is the voltage across the cell terminals, k is Boltzmann's constant, and T is the temperature. A photovoltaic cell is electrically equivalent to a current generator in parallel with a diode as shown in Figure 1.3. When the photovoltaic cell is exposed to light, a photocurrent is generated which flows in the opposite direction of the dark current. The total current density in the photovoltaic cell is therefore

$$J(V) = J_{SC} - J_{dark}(V) = J_{SC} - J_0\left[\exp\left(\frac{qV}{kT}\right) - 1\right] \tag{1.2}$$

where J is the total current density and J_{SC} is the photocurrent density (or short circuit current density). Equations 1.1 and 1.2 are only valid for ideal photovoltaic diodes. Non-idealities and parasitic behaviors will be studied in later chapters. The electrical

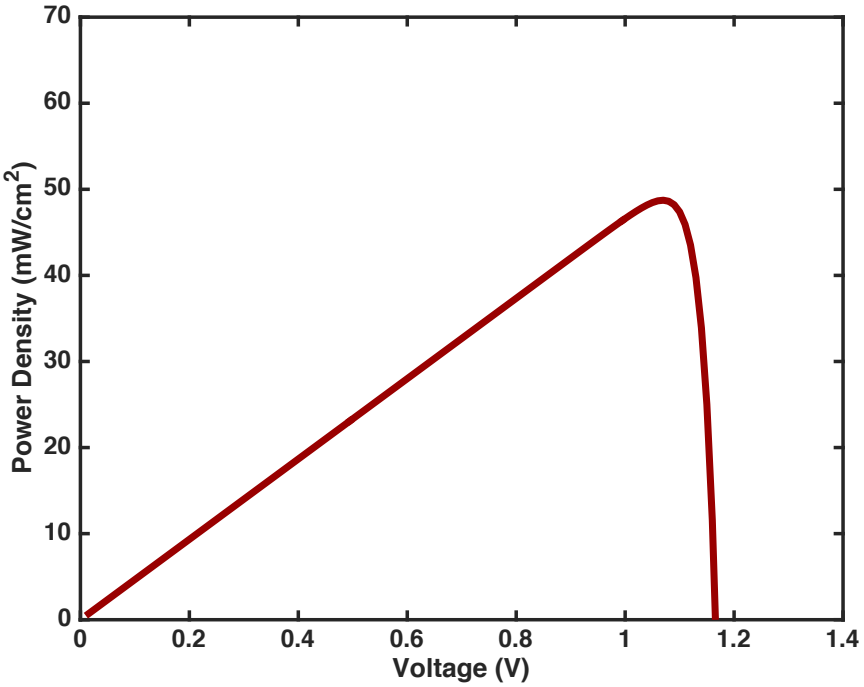

Figure 1.5. Power density as a function of voltage for an ideal diode exposed to light.

characteristics of a photovoltaic device is shown in Figure 1.4, demonstrating photovoltaic response when exposed to a light source. The open-circuit voltage (V_{OC}) is the voltage at which J_{SC} and J_{dark} cancel each other and Equation 1.2 equals zero. The resulting relationship is

$$V_{OC} = \frac{kT}{q} ln \left[\frac{J_{SC}}{J_0} + 1\right] \tag{1.3}$$

demonstrating a logarithmic relationship between open-circuit voltage and light intensity. The power density (P) of the photovoltaic cell is given by

$$P = JV \tag{1.4}$$

Equation 1.4 has a maximum value (P_{max}) corresponding to the maximum power point of the photovoltaic cell. Figure 1.5 demonstrates the power density of an ideal photovoltaic

cell as a function of voltage. The voltage and current density at the maximum power point is identified as V_m and J_m, respectively. The fill factor of a photovoltaic cell is a ratio that gives significant information about its efficiency. Fill factor (FF) is defined as

$$FF = \frac{J_m V_m}{J_{SC} V_{OC}} \tag{1.5}$$

The power conversion efficiency of a photovoltaic cell can be defined using the relations we have defined above. If the incident light power density is P_S, then the power conversion efficiency (η) is

$$\eta = \frac{J_m V_m}{P_S} = \frac{J_{SC} V_{OC} FF}{P_S} \tag{1.6}$$

FF and η have a maximum value of 1 and is often expressed as a percentage. J_{SC}, V_{OC}, FF, and η are the fundamental figures of merit for photovoltaic devices which will be used throughout this thesis.

1.4 Solar Irradiance

Light is composed of photons or packets of energy. Photons can be characterized in units of energy or wavelength. Energy of a photon has an inverse relationship with wavelength described by

$$E = \frac{hc}{\lambda} \tag{1.7}$$

where E is energy, λ is wavelength, h is Planck's constant, and c is the speed of light. The irradiance from a source of light is the amount of radiant energy received from the

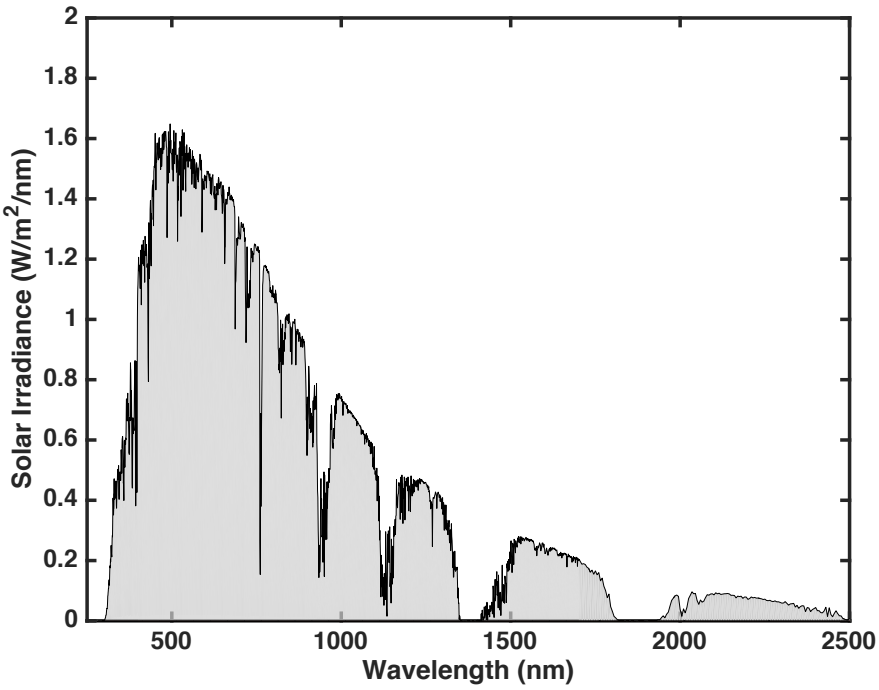

Figure 1.6. Solar irradiance at the surface of the earth as a function of wavelength.

source per unit area per unit time. The solar spectrum contains light with a range of wavelengths that span from the high energy ultraviolet to the low energy infrared. The solar irradiance is strongest in the visible range (400-700 nm) of the solar spectrum. This can be seen in Figure 1.6 which shows the solar irradiance at the surface of the earth as a function of wavelength.

The solar spectrum can be approximated as the spectrum of a black body. A black body emits photon with a distribution of energies, whose shape is determined by the characteristic temperature, T_S, of the black body. The T_S that best matches the solar spectrum is 5760 K. The spectral photon flux of a black body is given by

$$b_s(E) = \frac{2F_s}{h^3c^2}\left(\frac{E^2}{\exp\left(\frac{E}{kT_s}\right)-1}\right) \quad (1.8)$$

where F_s is a geometrical factor which describes the angular range from the black body to the surface. This value is $2.16 \times 10^{-5}\pi$ for the sun as seen from the earth. The irradiance of a black body is defined as

$$L(E) = Eb_s(E) \quad (1.9)$$

In order to determine the total power density emitted from a black body, Equation 1.9 must be integrated over the full energy range of the spectrum. The total power density at the surface of the sun is 62 MWm^{-2}. This value is reduced to 1353 Wm^{-2} just outside the atmosphere of the earth. The earth's atmosphere reduces this value further because it filters parts of the spectrum. The total power density at the surface of the earth is around 900 Wm^{-2}. For convenience, the standard solar spectrum that is used for determining figures of merit for photovoltaic devices is defined as the AM1.5 spectrum, whose integrated irradiance is 1000 Wm^{-2}. The outdoor efficiency values given in this thesis use the AM1.5 spectrum with 1000 Wm^{-2} incident light power density.

1.5 Indoor Illuminance

In addition to solar irradiance, photovoltaic devices can be used to harvest energy from indoor light sources. Indoor light sources have a much narrower spectra compared with the solar spectrum since they were designed to be efficiency light emitters in the visible region. Figure 1.7 shows the spectrum of a common indoor light source in comparison with the solar spectrum. The differences in spectrum shape between indoor

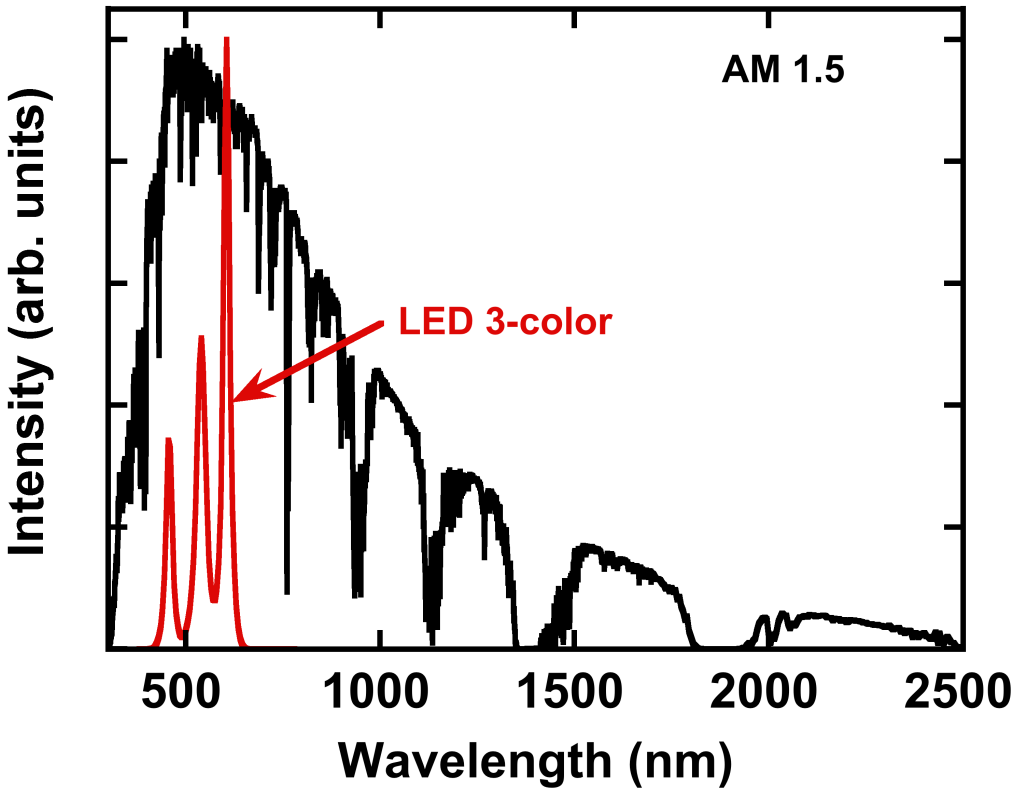

Figure 1.7. White LED spectrum compared with the solar spectrum.

and outdoor sources results in major differences in photovoltaic device performance and, therefore, design. The differences in design and performance of indoor photovoltaic devices is explored in later chapters.

Most present day indoor lighting sources fall into two categories, fluorescent bulbs and light emitting diodes (LEDs). There are two types of LEDs used for indoor lighting, phosphor-based and 3-color. All of these indoor light sources emit light in the visible region of the electromagnetic spectrum, primarily between 400-700 nm. The spectra for all three of these indoor lighting sources is shown in Figure 1.8.

In addition to the narrower spectra, indoor light is typically characterized by illuminance instead of irradiance. Illuminance is the total luminous flux incident on a

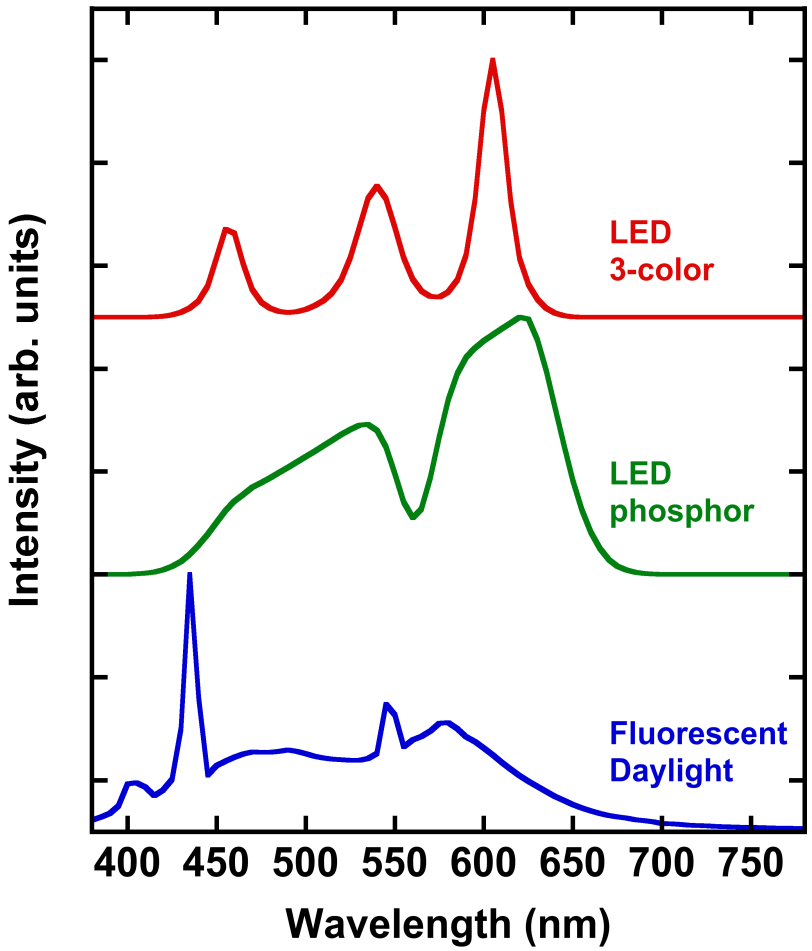

Figure 1.8. Spectra for three different indoor lighting sources.

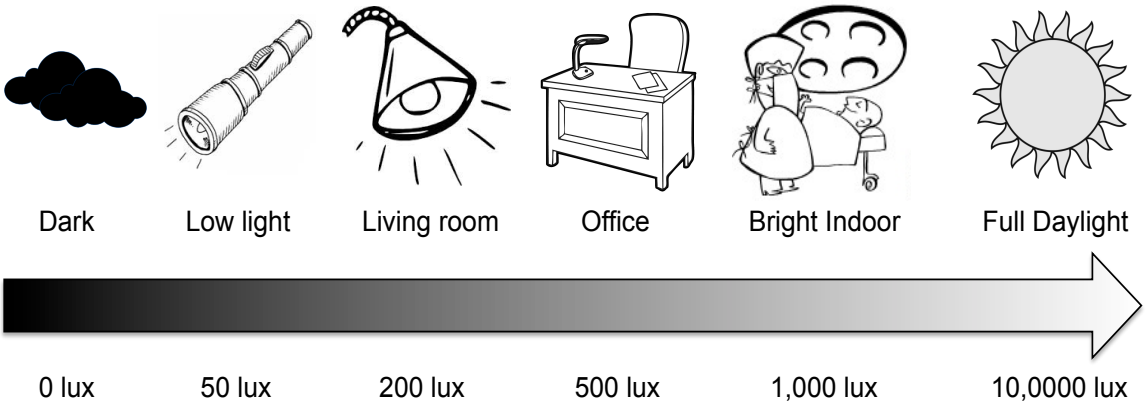

Figure 1.9. Range of illuminance from dark indoor conditions to bright outdoor conditions.

surface per unit area. Luminous flux is defined as

$$F = 683\frac{lm}{W}\int_0^\infty V(\lambda)L(\lambda)d\lambda \tag{1.10}$$

where F is the luminous flux in units of lumens, V(λ) is the luminosity function, and L(λ) is the irradiance of the light source as a function of wavelength. The luminosity function is the spectral response of the human eye, or the perceived brightness of different frequencies of light by a human eye. Illuminance has units of lux (lx) which is defined as lumens per unit area. Figure 1.9 gives a range of illuminance values for different lighting conditions. It is important to note the large difference in illuminance between indoor and outdoor light. Dim indoor lighting conditions have a strong effect on photovoltaic device performance and will be discussed in later chapters.

1.6 Detailed Balance Theory

The detailed balance theory for p-n junction solar cells was first introduced by Shockley and Queisser in 1961 [3]. This theory arises from the law of conservation of energy. In addition to absorbing photons, the photovoltaic cell also emits photons. When the device is not illuminated, the rate of photon absorption must be equal to the rate of photon emission in order to keep the concentration of charge carriers in the device constant at steady state. In the dark, the current density absorbed by the photovoltaic cell from the ambient is

$$j_{abs}(E) = q\big(1 - R(E)\big)a(E)b_a(E) \tag{1.11}$$

where a(E) is the probability of absorbing a photon of energy E, R(E) is the probability of

reflecting a photon, and $b_a(E)$ is the spectral photon flux from the ambient which can be calculated from Equation 1.8. The equivalent current density emitted from the photovoltaic cell is

$$j_{rad}(E) = q\big(1 - R(E)\big)\varepsilon(E)b_a(E) \tag{1.12}$$

where ε(E) is the probability of emitting a photon of energy E. Since the photovoltaic cell has the same temperature as the ambient, the spectral photon flux from the photovoltaic cell is also $b_a(E)$. At steady state, Equations 1.11 and 1.12 must be equal, leading to

$$a(E) = \varepsilon(E) \tag{1.13}$$

so the probability of absorption of a photon of energy E must be equal to the probability of emission of a photon of energy E.

When a photovoltaic cell is exposed to a source of light, the cell absorbs photons from the light source as well as the ambient. Equation 1.11 becomes

$$j_{abs}(E) = q\big(1 - R(E)\big)a(E)\left(b_s(E) + \left(1 - \frac{F_s}{F_e}\right)b_a(E)\right) \tag{1.14}$$

where the coefficient in front of b_a is the fraction of the incident ambient flux which has not been replaced by the incident flux from the light source. The equivalent current density emitted from the photovoltaic cell is also altered since the illumination increases the electrochemical potential energy of the cell. Equation 1.12 becomes

$$j_{rad}(E) = q\big(1 - R(E)\big)\varepsilon(E)b_e(E, \Delta\mu) \tag{1.15}$$

where Δμ is the electrochemical potential energy of the photovoltaic cell. The net equivalent current density is therefore

$$j_{net}(E) = j_{abs}(E) - J_{rad}(E)$$

$$= q\big(1 - R(E)\big)a(E)\left(b_s(E) + \left(1 + \frac{F_s}{F_a}\right)b_a(E) - b_e(E, \Delta\mu)\right) \qquad (1.16)$$

Equation 1.13 can be split into the photocurrent and radiative recombination current. The portion of Equation 1.13 that contributes to the photocurrent is

$$j_{sc}(E) = q\big(1 - R(E)\big)a(E)\left(b_s(E) - \frac{F_s}{F_e}b_a(E)\right) \qquad (1.17)$$

In order to calculate the total photocurrent Equation 1.14 must be integrated over the energy range of interest. The total photocurrent density is

$$J_{sc} = q\int_0^\infty QE(E)b_s(E)dE \qquad (1.18)$$

where QE is the quantum efficiency of the photovoltaic cell and is equivalent to the product of the collection and absorption efficiencies. QE is therefore the probability that an incident photon of energy E will deliver one electron to the external circuit. Equation 1.18 emphasizes the important of spectra on the performance of photovoltaic devices. The spectral photon flux can be very different depending on the content of the spectrum and the intensity of the light source. This part of Equation 1.18 limits the maximum photocurrent available for the photovoltaic device. QE determines how much of the available photocurrent will be provided to the external circuit. Exploiting this relationship is crucial to develop high-efficiency photovoltaic devise at high intensity as well as low intensity. The total photocurrent of photovoltaic cells of various materials will be calculated throughout this thesis using Equation 1.18 for outdoor and indoor illumination sources.

1.7 Thesis Organization

This thesis includes studies of photovoltaic energy harvesting for different light sources and their corresponding spectra and intensity. It is organized into the following five chapters.

Chapter II provides an in-depth study of different ZnTe heterojunction solar cells and their effectiveness as a base structure for the ZnTeO intermediate band solar cell. Studies of the p-ZnTe/n-GaAs, n-ZnSe/p-ZnTe/p-GaSb, and p-ZnTe/n-ZnSe/n-GaAs heterojunctions are presented and their limitations are discussed.

Chapter III introduces indoor photovoltaic energy harvesting with GaAs-based photovoltaic devices. Theoretical limits on performance are studied as well as experimental results.

Chapter IV explores the different sources of loss in indoor photovoltaic devices. The effects of external quantum efficiency, dark current, and shunt resistance are presented. Methods of mitigating these degradations in performance are discussed.

Chapter V summarizes the research in this dissertation and provides future direction of study including indoor photovoltaic energy harvesting with InGaP cells, modular photovoltaic device design, and subcutaneous light harvesting using GaAs photovoltaic devices.

Chapter II

ZnTe Solar Cell

2.1 Introduction

The ultimate power conversion efficiency of a solar cell is limited by the current generation from solar photons and voltage provided by the energy of extracted electrons. The maximum voltage attainable for a diode solar cell (open-circuit voltage; V_{OC}) is limited to the bandgap energy E_G of the material, where voltage is further reduced below E_G/q due to non-radiative losses, mismatch between the acceptance angle of spontaneous emission and the solid angle subtended from the sun, and energy losses from electrical contacts. Experimentally, the open-circuit voltage of a solar cell has been observed to match E_G/q when operating at low temperature under solar concentration [4].

Another mechanism for open-circuit voltage reduction is band offset in heterojunction device architectures. Heterojunctions have emerged as important in next generation solar cells in order to facilitate charge separation and collection, including organic solar cells, thin-film solar cells, and intermediate band solar cells (IBSCs). An intermediate band solar cell is a photovoltaic device that uses electronic states in between the conduction band and valence band of a semiconductor to efficiently absorb photons

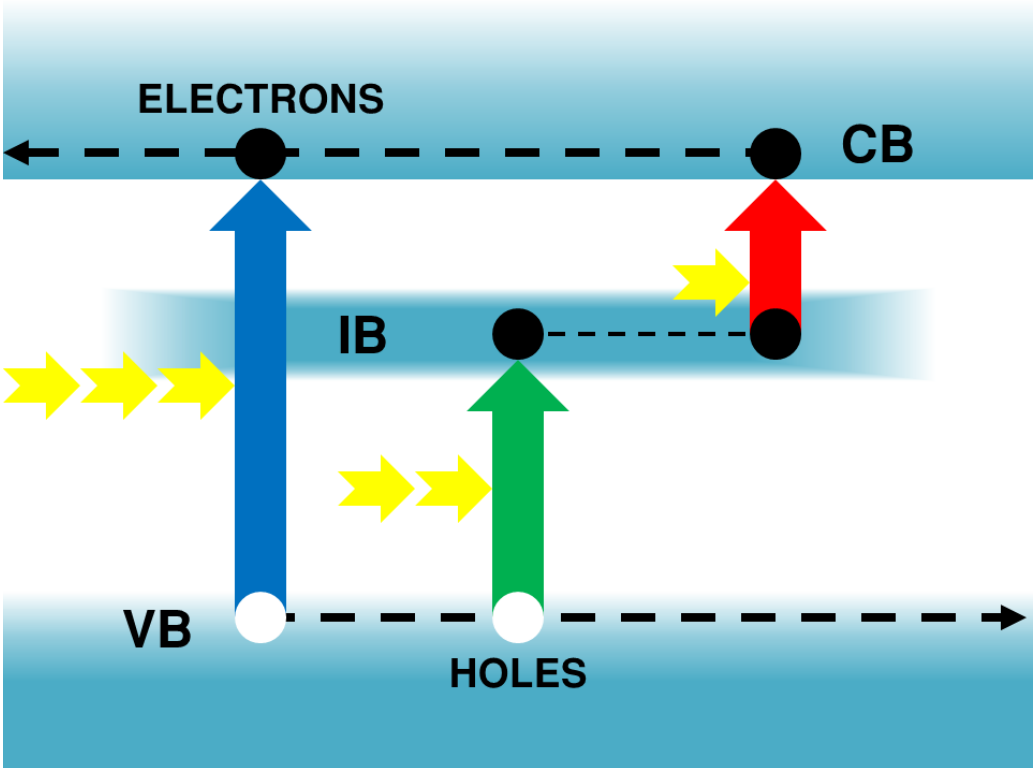

Figure 2.1. Energy band diagram of an intermediate band solar cell.

of three different energy ranges as shown in Figure 2.1. Since more of the solar spectrum can be absorbed as shown in Figure 2.2, IBSCs allow power conversion efficiencies to exceed the theoretical limits of conventional single-junction solar cells. The theoretical maximum power conversion efficiency of an intermediate band solar cell can be calculated by considering the circuit model of an intermediate band solar cell as shown in Figure 2.3. The IBSC can be modeled as a current source and diode in parallel with two other current source-diode pairs in series. The current sources represent the generation of photocurrent from excited carriers from the valence band to the conduction band, valence band to the intermediate band, and intermediate band to the conduction band. The diodes represent the recombination mechanisms from the conduction band to the valence band,

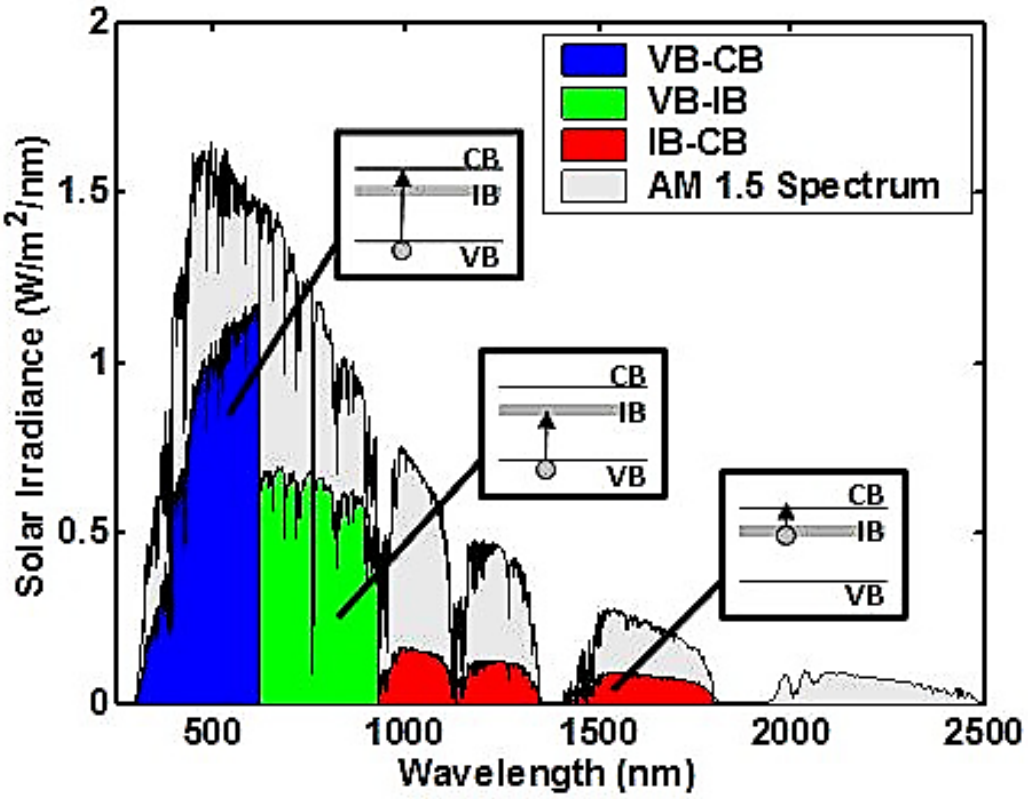

Figure 2.2. The solar spectrum split into three wavelength ranges for efficient power collection from an intermediate band solar cell.

conduction band to intermediate band, and intermediate band to valence band. Using this circuit model and detailed-balance theory, the maximum efficiency for an intermediate band solar cell can be calculated. Figure 2.4 demonstrates a contour plot of the peak efficiencies for an intermediate band solar cell as a function of bandgap energy and intermediate band location. The intermediate band location is referring to the energy gap generated between the conduction band and the intermediate band. The limiting theoretical power conversion efficiency for an IBSC is 63% for a material with a bandgap of 1.95 eV and intermediate band location of 0.7 eV. Figure 2.4 also reveals the possibility of high-efficiency photovoltaics for materials of a wide range of bandgap

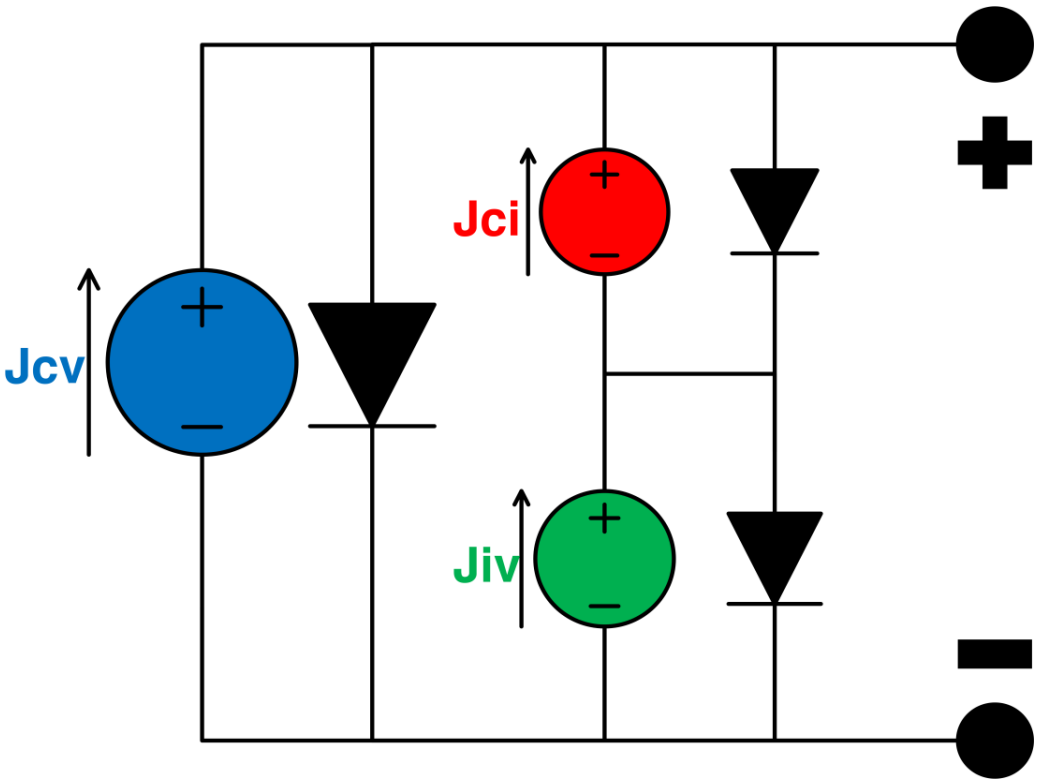

Figure 2.3. Circuit model of an intermediate band solar cell.

energies.

Heterojunctions also facilitate the formation of a p-n junction in cases where the semiconductor of interest cannot be selectively doped n-type or p-type. ZnTe is an example of such a case where n-type doping is difficult to achieve due to the self-compensation from the native antisite defect in ZnTe [5], requiring the use of heterojunctions with n-type semiconductors, such as GaAs, ZnO, and ZnSe with lattice mismatch 7%, 25%, and 8%, respectively [6]-[13]. All of these cases have a large lattice mismatch, resulting in the formation of threading dislocations, degrading device performance. Efficient solar cells require dislocation densities less than 10^6 cm^{-2} to preserve minority carrier lifetime [14].

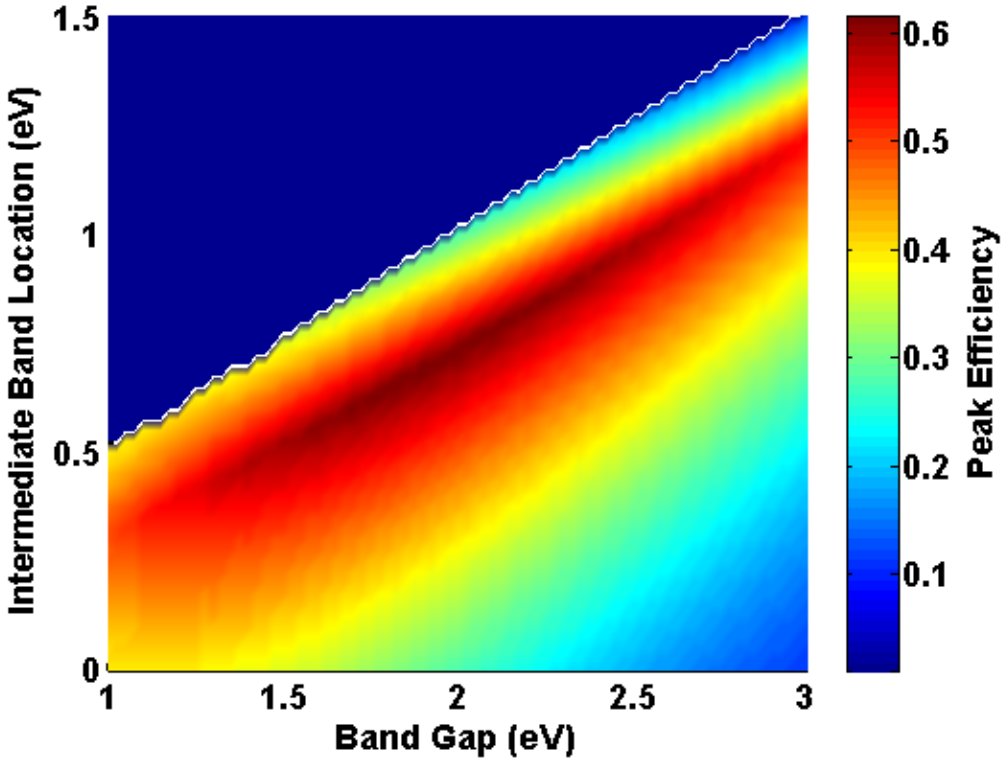

Figure 2.4. Contour plot of peak efficiency as a function of intermediate band location and bandgap energy.

ZnTe is a promising material for solar photovoltaics, where dilute incorporation of oxygen to form ZnTeO alloys can provide a bulk material for intermediate band solar cells [7], [9], [10], [12], [13], [15]-[17]. Sub-bandgap photocurrent response due to multi-photon transitions has been demonstrated, but the voltage generated in these devices is still below expectations. So far, the highest V_{OC} achieved for the ZnTeO solar cell is approximately 1 V using a p-ZnTe/n-ZnSe heterojunction [12]. The low V_{OC} can be attributed to both defects in the ZnTe material and heterojunction band offsets. The theoretical photovoltaic response of a ZnTeO IBSC is shown in Figure 2.5 alongside the photovoltaic response of a ZnTe single-gap solar cell and an ideal IBSC solar cell. The theoretical open-circuit voltage for a ZnTe solar cell is 2 V. The discrepancy between

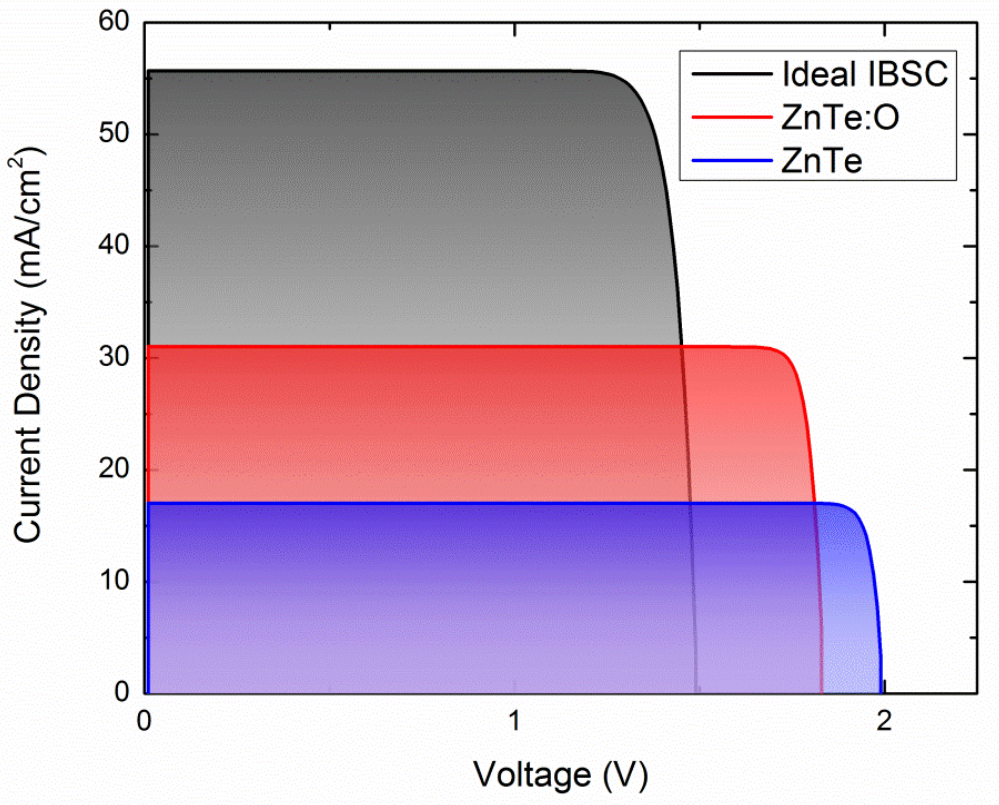

Figure 2.5. Plot of I-V for ideal IBSC, ZnTe:O IBSC, and single gap ZnTe solar cell.

theoretical and measured open-circuit voltage motivates further investigation into V_{OC} reduction mechanisms and methods of improvement.

This chapter explores three different ZnTe heterojunction solar cells including p-ZnTe/n-GaAs, n-ZnSe/p-ZnTe/p-GaSb, and p-ZnTe/n-ZnSe/n-GaAs. The performance and limitations of all three heterostructures are studied including their viability as device structures for a ZnTeO intermediate band solar cell. The author fabricated and characterized the n-ZnSe/p-ZnTe/p-GaSb and p-ZnTe/n-ZnSe/n-GaAs solar cells.

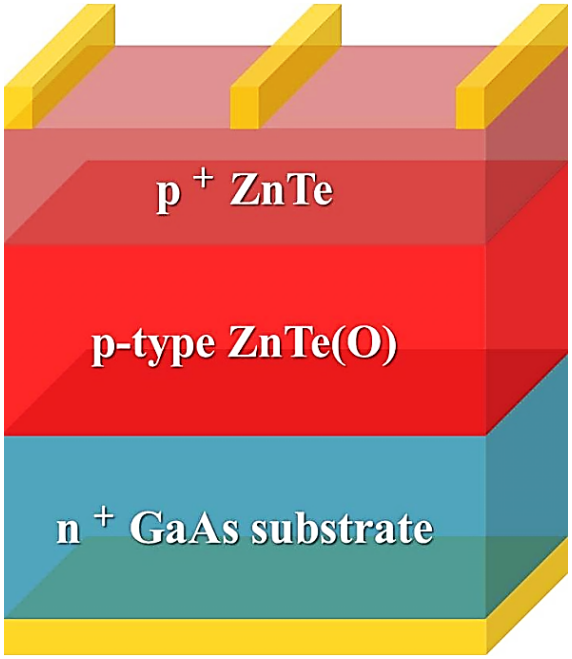

Figure 2.6. p-ZnTe/n-GaAs heterojunction solar cell device structure.

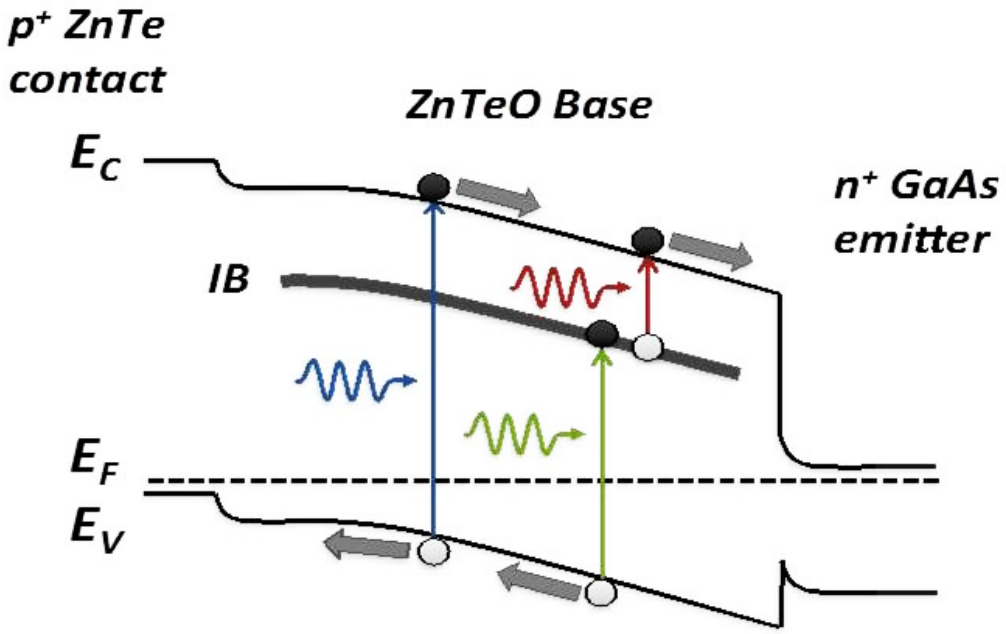

Figure 2.7. p-ZnTe/n-GaAs heterojunction solar cell band lineup.

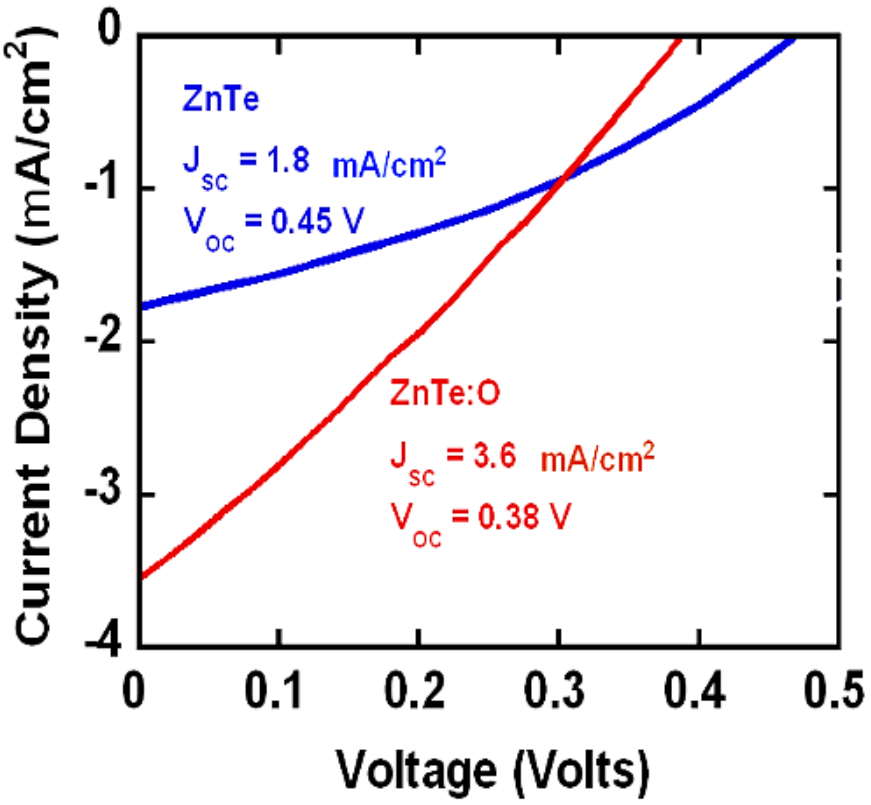

Figure 2.8. Current density versus voltage for a p-ZnTe/n-GaAs solar cell and a p-ZnTe:O/n-GaAs solar cell under halogen illumination (adopted from [7]).

2.2 p-ZnTe/n-GaAs Heterojunction Solar Cell

The first ZnTeO IBSC was developed by Wang et al. [7] using a p-ZnTe/n-GaAs heterostructure. The devices were grown by molecular beam epitaxy (MBE) on n-GaAs substrates as shown in Figure 2.6. Two devices were grown, one with a ZnTeO intermediate layer and a control sample. The resulting electronic band lineup is shown in Figure 2.7 for the sample with the ZnTeO intermediate layer, illustrating the three photon energy ranges the photovoltaic device can absorb using the intermediate band in the ZnTeO base. For these samples, the n-GaAs substrate serves as the emitter for the device. The large lattice mismatch of 7% produces threading dislocations at the junction. The

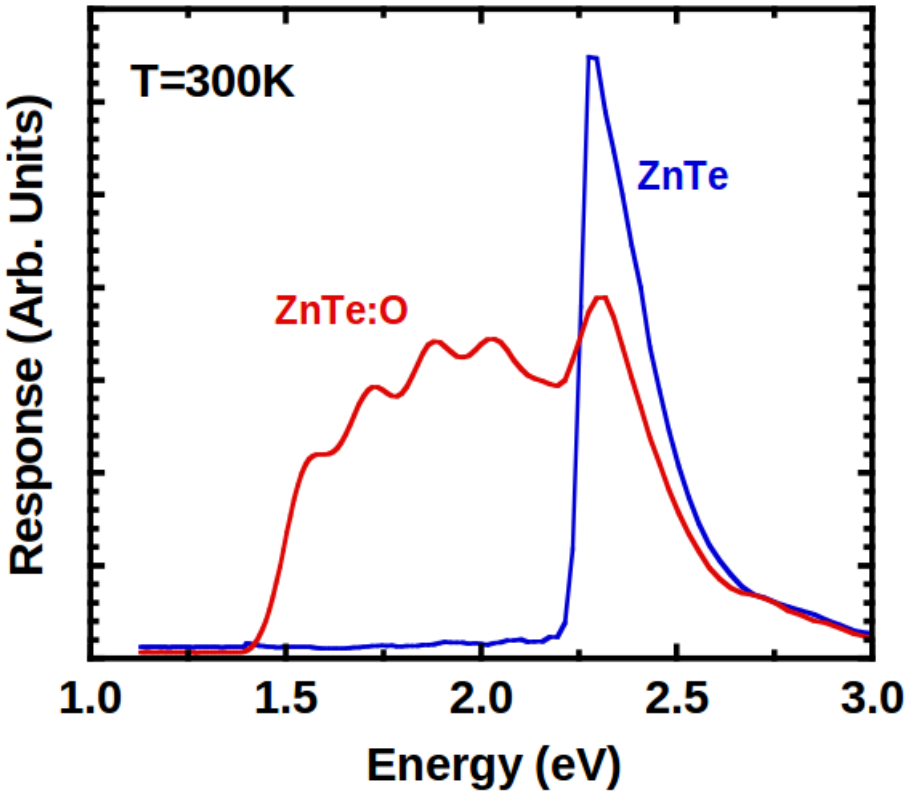

Figure 2.9. Photoluminesense for a ZnTe sample and ZnTeO sample (adopted from [7]).

bad quality of the junction results in poor photovoltaic response. Figure 2.8 shows the photovoltaic response of the ZnTe control sample and ZnTeO IBSC sample under halogen illumination. The ZnTeO sample demonstrates a 100% improvement in short-circuit current and a 15% reduction in open-circuit voltage. Overall, the improvement in efficiency of the ZnTeO IBSC sample over the ZnTe control sample was approximately 50%. Despite this improvement, the overall efficiency of both photovoltaic devices was very poor, less than 1% power conversion efficiency. The main reason for the poor performance is the low open-circuit voltage. The low V_{OC} is indicative of the quality of the junction between the p-ZnTe base and n-GaAs emitter.

Even though the overall performance was low, this device structure allows us to

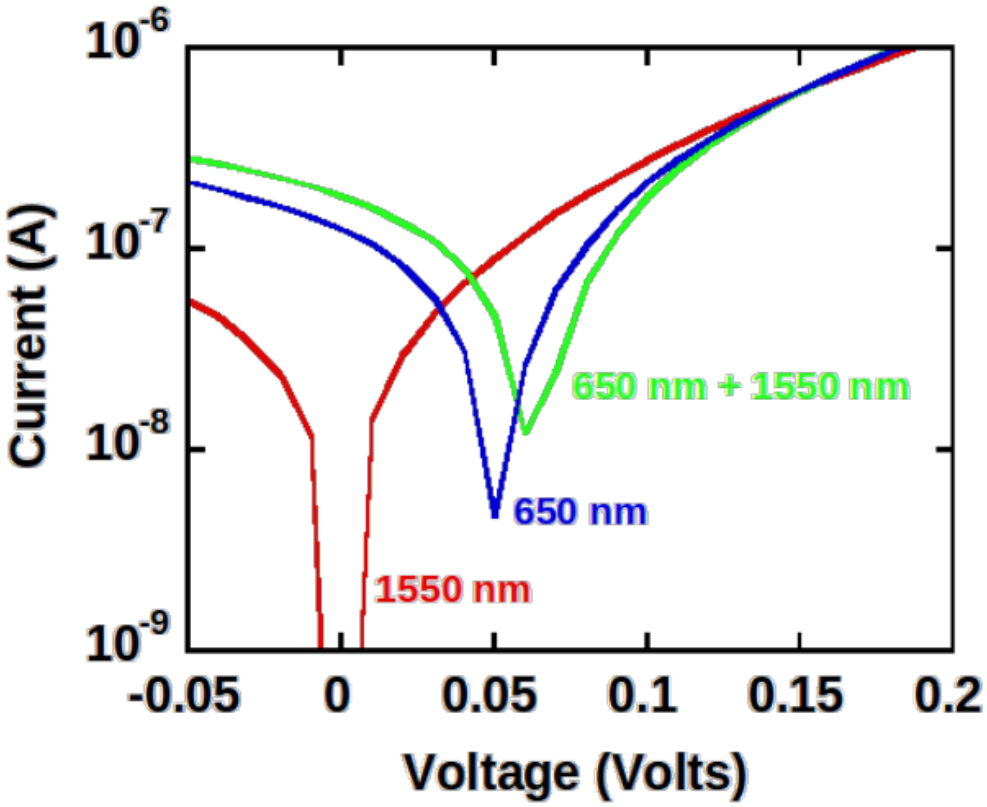

Figure 2.10. Subbandgap response for a p-ZnTe:O/n-GaAs solar cell (adopted from [7]).

study the sub-bandgap behavior of the ZnTeO IBSC. One method to study this behavior is using photoluminescence. Figure 2.9 demonstrates the photoluminescence spectra of the ZnTeO sample compared with the control ZnTe sample. The ZnTe control samples shows a sharp bandedge response near 2.3 eV and no sub-bandgap response. On the other hand, the ZnTeO IBSC sample has a spectral response that ranges from 1.6 eV up to the bandgap near 2.3 eV. The spectral response at lower energy levels is a result of the intermediate band electronic states that allows for radiative emission at sub-bandgap energies.

Another way to study sub-bandgap response is by exciting the ZnTeO IBSC

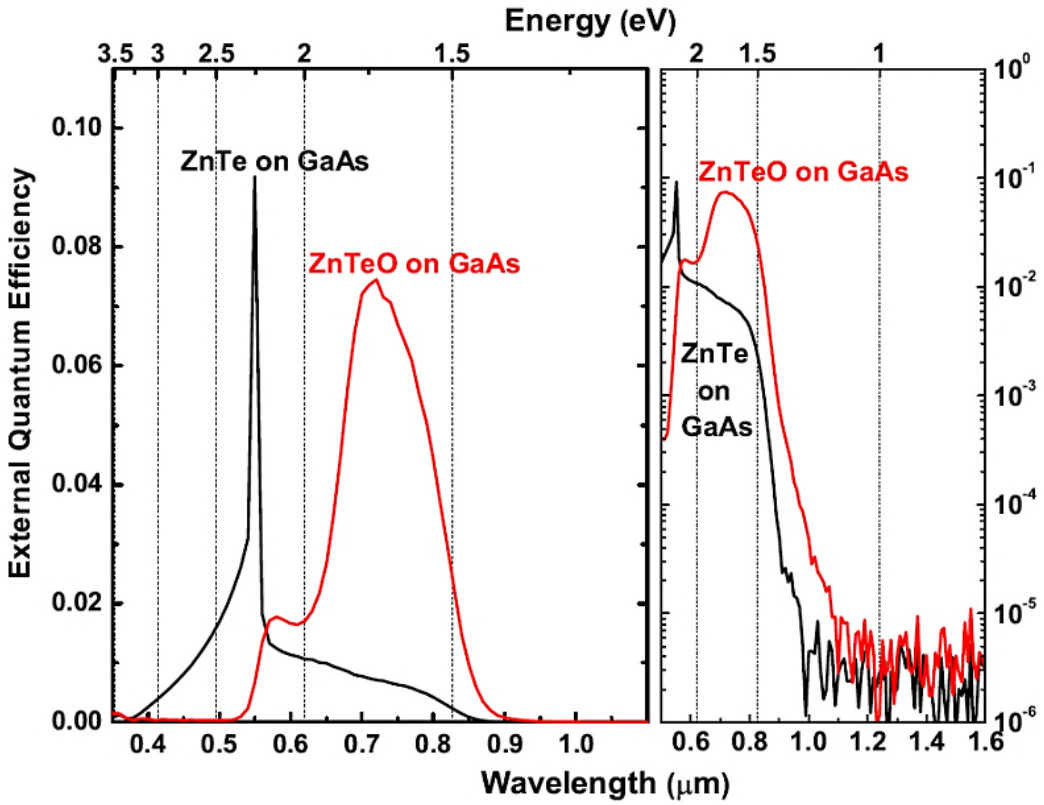

Figure 2.11. External quantum efficiency for a p-ZnTe/n-GaAs solar cell and a p-ZnTeO/n-GaAs solar cell.

sample with lasers of different energy and observing the photocurrent. This method demonstrates the multiphoton process that is vital to high-efficiency intermediate band solar cells. Figure 2.10 shows the current-voltage characteristics of the ZnTeO IBSC sample under excitation from a 1550 nm and 650 nm laser. The excitation from the 1550 nm laser did not give any photovoltaic response because the laser photon energy is too small to create an electronic transition in the material. The excitation from the 650 nm laser was enough to excite electrons from the valence band to the intermediate band and also from the intermediate band to the conduction band. When both lasers are exciting the sample at the same time the photocurrent increases because the 1550 nm laser is

augmenting the transitions from the intermediate band to the conduction band.

External quantum efficiency (EQE) provides further information about the absorption of photons and collection of carriers as a function of wavelength. Figure 2.11 demonstrates the external quantum efficiency of a p-ZnTe/n-GaAs cell and a p-ZnTeO/n-GaAs cell. The ZnTeO photovoltaic cell shows strong sub-bandgap EQE between 1.5 eV and 2 eV compared with the ZnTe control cell. Both cells have poor overall EQE due to poor collection of carriers near the top surface and near the junction of the cells. Both of these samples do not have a window layer to protect carriers from surface recombination. Also, the threading dislocations near the junction prevents carriers from moving towards the contacts, recombining non-radiatively.

This section summarized previous work done on p-ZnTe/n-GaAs and p-ZnTeO/n-GaAs solar cells and illustrates the need for a different junction technology in order to improve overall photovoltaic performance and efficiency.

2.3 n-ZnSe/p-ZnTe/p-GaSb Heterojunction Solar Cell

In this section the performance of the n-ZnSe/p-ZnTe/p-GaSb heterojunction solar cell is studied in order to observe the effects of a window layer and improved lattice matched substrate. Figure 2.12 and Figure 2.13 illustrate the device structure and electronic band lineup for the n-ZnSe/p-ZnTe/p-GaSb solar cell respectively. The larger bandgap n-ZnSe emitter serves as a window layer, preventing carriers from recombining at the surface of the device. The GaSb substrate is lattice matched to ZnTe resulting in less threading dislocations during growth than on GaAs substrates.

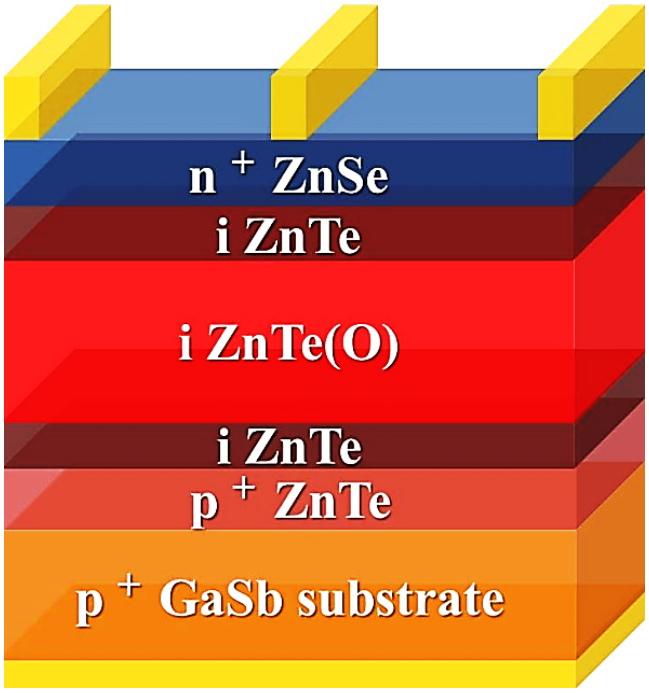

Figure 2.12. n-ZnSe/p-ZnTe heterojunction solar cell device structure.

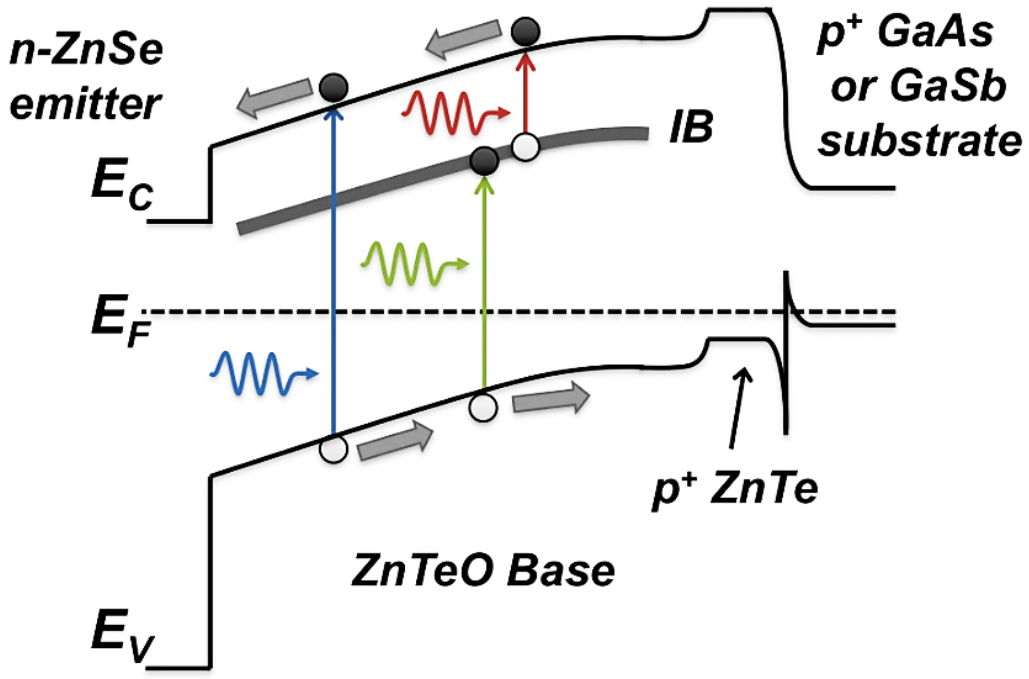

Figure 2.13. n-ZnSe/p-ZnTe heterojunction solar cell band lineup.

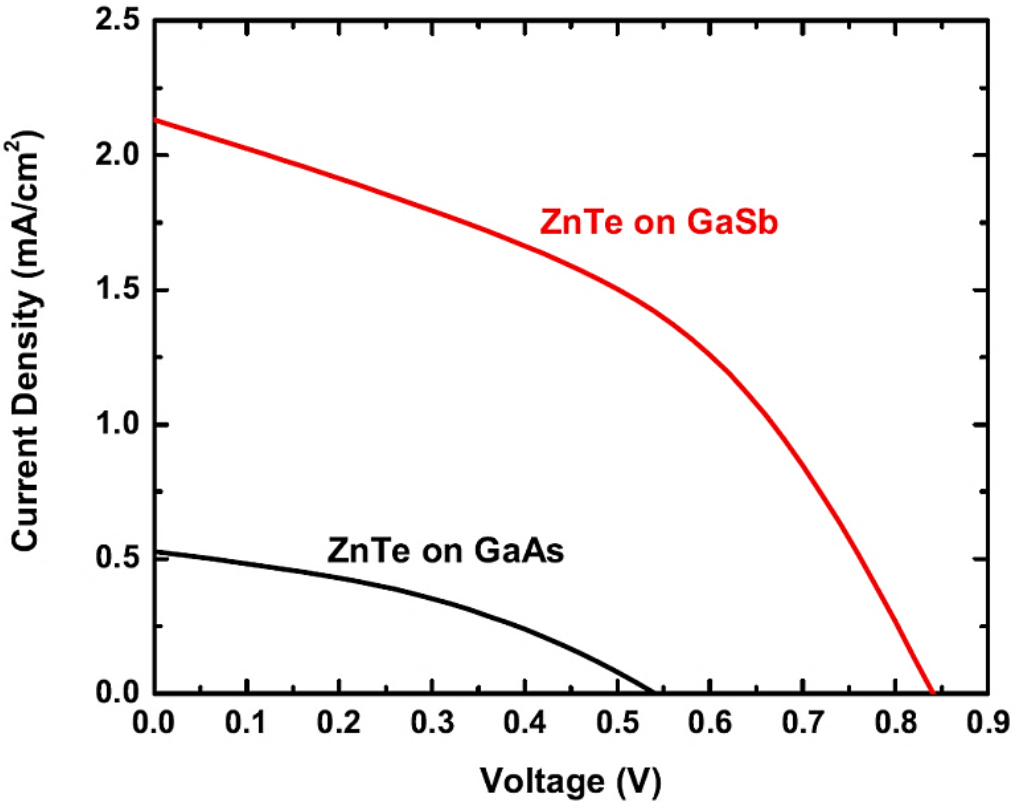

Figure 2.14. Current density versus voltage for a n-ZnSe/p-ZnTe/p-GaAs solar cell and a n-ZnSe/p-ZnTe/p-GaSb solar cell under halogen illumination.

The improvement in photovoltaic response due to the GaSb substrate is shown in Figure 2.14 where the current density versus voltage of a n-ZnSe/p-ZnTe/p-GaAs solar cell is compared with a n-ZnSe/p-ZnTe/p-GaSb solar cell under halogen illumination. Both open-circuit voltage and short-circuit current improve substantially. V_{OC} increased approximately 55% and J_{SC} increased approximately 300%. Despite the improvements in photovoltaic performance, the overall efficiency of the n-ZnSe/p-ZnTe/p-GaSb solar cell is substantially lower than theoretically predicted. The primary reason is the low open-circuit voltage. The V_{OC} needs to be more than twice the current amount in order for efficient photovoltaic response. The reasons for the low V_{OC} will be further discussed in

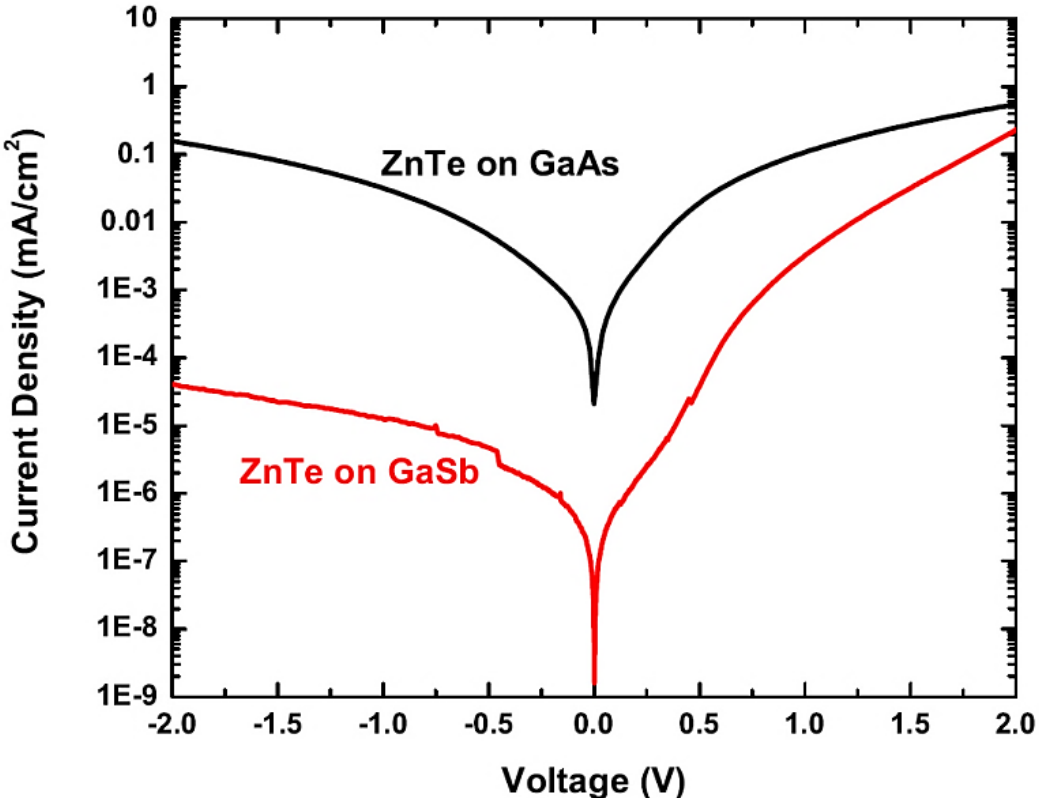

Figure 2.15. Dark current density versus voltage for a n-ZnSe/p-ZnTe/p-GaAs solar cell and a n-ZnSe/p-ZnTe/p-GaSb solar cell.

the section 2.5.

The increase in open-circuit voltage and short-circuit current is due to a large reduction in dark current. Figure 2.15 shows the dark current density versus voltage for a device grown on a GaAs substrate and a device grown on a GaSb substrate. The n-ZnSe/p-ZnTe/p-GaSb solar cell has a reverse saturation current four orders of magnitude lower than the n-ZnSe/p-ZnTe/p-GaAs solar cell. The sample grown on GaSb also shows improved forward biased behavior with improved ideality factor.

The improvement in open-circuit voltage can be further analyzed by measuring the behavior of V_{OC} at low temperatures. Figure 2.16 shows the open-circuit voltage

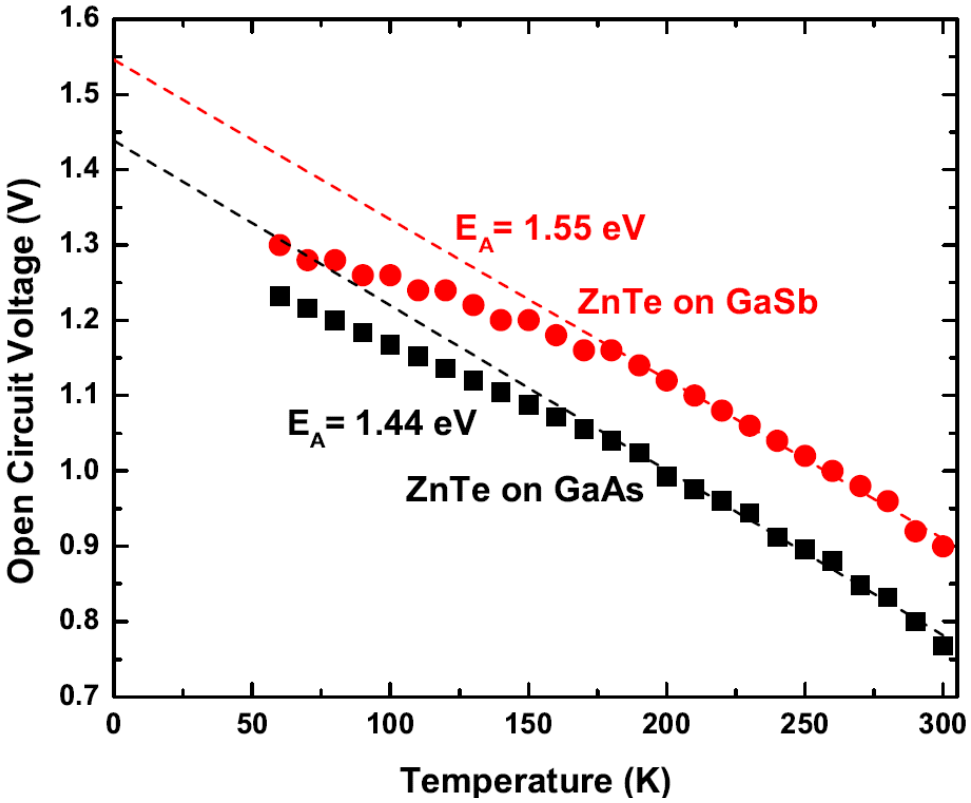

Figure 2.16. Open circuit voltage versus temperature for a n-ZnSe/p-ZnTe/p-GaAs solar cell and a n-ZnSe/p-ZnTe/p-GaSb solar cell.

versus temperature for a n-ZnSe/p-ZnTe/p-GaAs solar cell and a n-ZnSe/p-ZnTe/p-GaSb solar cell. As temperature decreases, the V_{OC} increases for both solar cells due to a reduction in non-radiative recombination rates. Defects in the devices are effectively "frozen out" and results in improved photovoltaic response. The activation energy or maximum open-circuit voltage can be extrapolated from the intersection of the linear portion of the curve at 0 K. The sample grown on GaSb demonstrated a 10% improvement in activation energy. This is indicative of the reduced concentration of defects in the photovoltaic cell due to the improved interface between ZnTe and the substrate. The temperature dependence of V_{OC} and its implications will be further

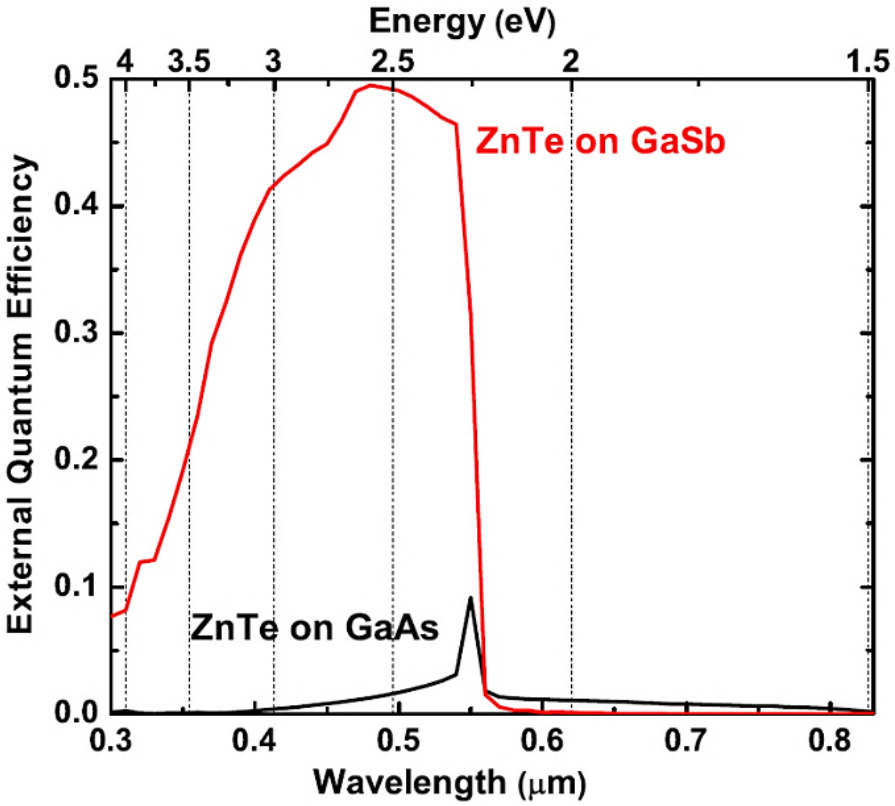

Figure 2.17. Quantum efficiency for a p-ZnTe/n-GaAs solar cell and a n-ZnSe/p-ZnTe/p-GaSb solar cell.

discussed in section 2.5.

The larger short-circuit current can be attributed to an improvement in above bandgap quantum efficiency. The external quantum efficiency for a p-ZnTe/n-GaAs solar cell and a n-ZnSe/p-ZnTe/p-GaSb solar cell is shown in Figure 2.17. The EQE above the bandgap for the cell grown on GaSb is dramatically improved over the cell grown on GaAs. This is due to the inclusion of an n-ZnSe window layer that separates excited carriers from high energy photons away from the surface of the cell.

In order to realize a high-efficiency ZnTeO IBSC, improvements are necessary in material quality and device design. This section showed improvements in ZnTe

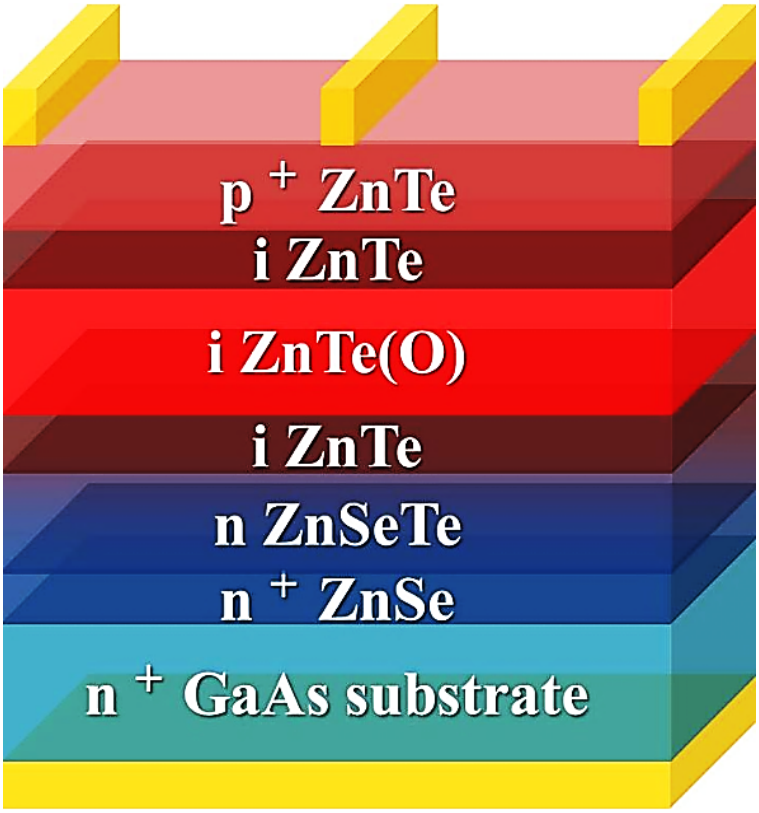

Figure 2.18. p-ZnTe/n-ZnSe heterojunction solar cell device structure.

photovoltaic response due to a lattice-matched substrate and a larger bandgap window layer.

2.4 p-ZnTe/n-ZnTeSe/n-GaAs Heterojunction Solar Cell

The other heterostructure that was studied was the p-ZnTe/n-ZnSe/n-GaAs so cell. The solar cell device structure and band lineup is illustrated in Figure 2.18 and Figure 2.19 respectively where ZnTe serves as the p-type contact and base layer and n-ZnSe is the emitter. The device was grown on an n-GaAs substrate since ZnSe is lattice-matched to GaAs. The effects of grading the junction between the ZnTe base layer and

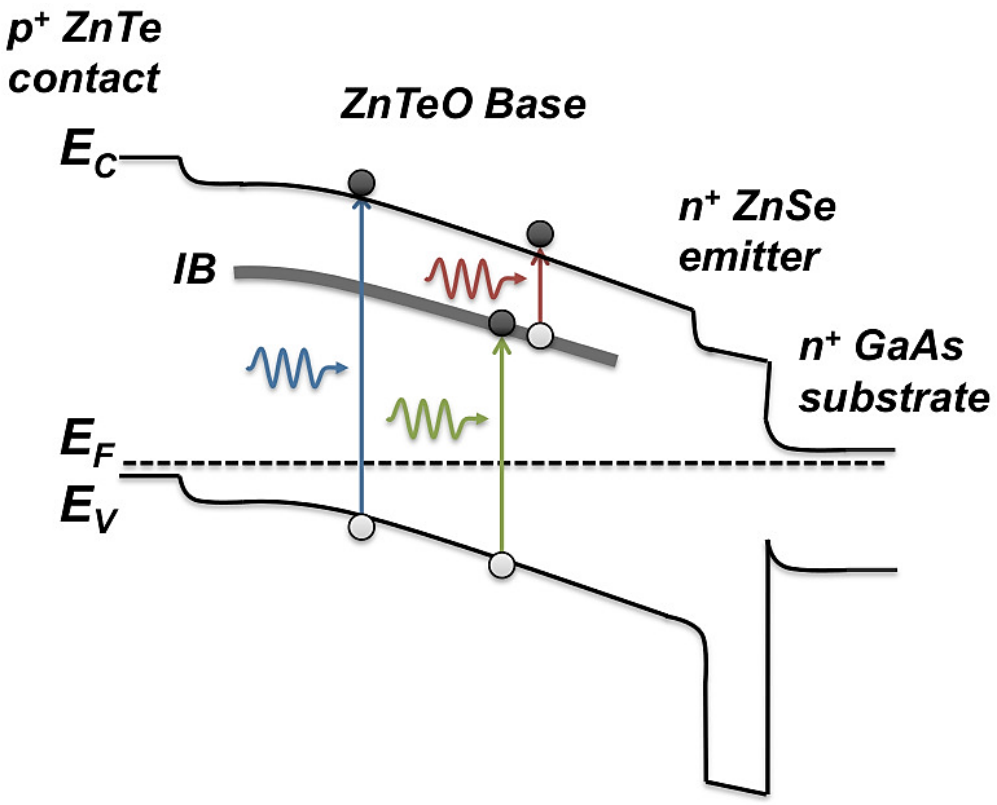

Figure 2.19. p-ZnTe/n-ZnSe heterojunction solar cell band lineup.

ZnSe emitter was studied.

Figure 2.20 shows the current density versus voltage for a p-ZnTe/n-ZnSe solar cell with an abrupt junction and one with a graded junction. The photovoltaic device with a graded junction demonstrate an improvement in short-circuit current of more than an order of magnitude compared with the photovoltaic device with an abrupt junction. The open-circuit voltage of the sample with the abrupt junction was slightly larger the the open-circuit voltage of the graded sample. The vast improvement in photovoltaic response allows for better studies of ZnTeO IBSCs.

The current density versus voltage for a ZnTe/GaSb solar cell and a ZnTeO/GaAs solar cell with a graded junction under AM1.5 illumination is shown in Figure 2.21. The

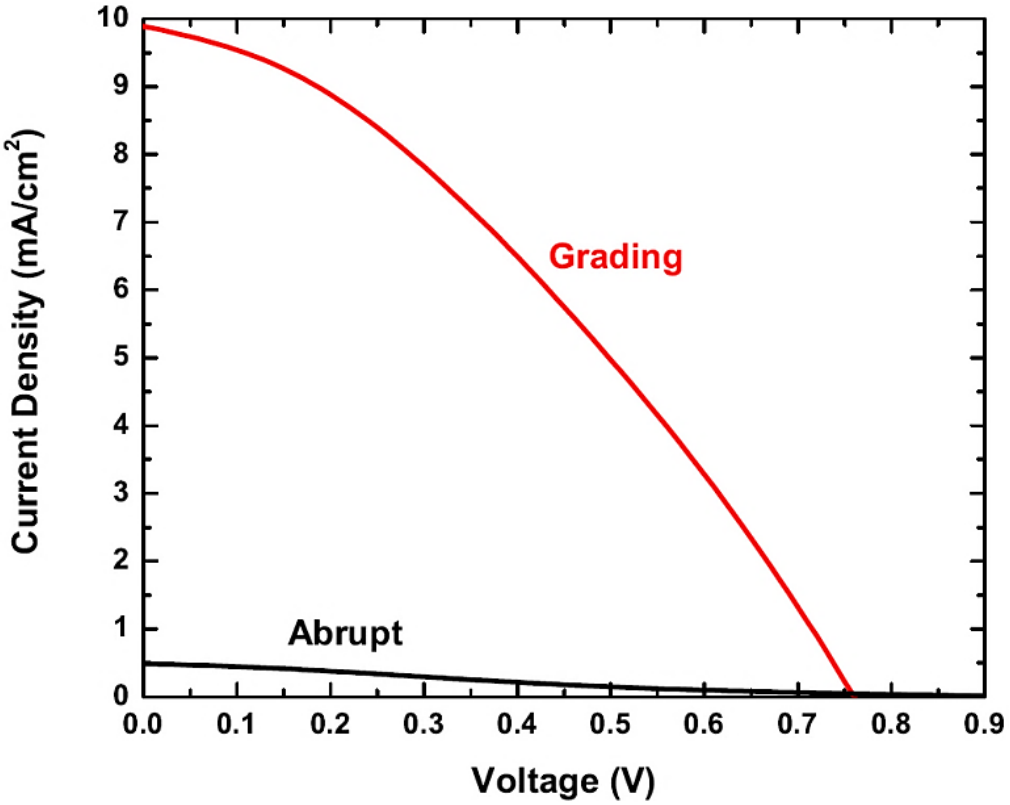

Figure 2.20. Current density versus voltage for two p-ZnTe/n-ZnSe solar cells with an abrupt junction and graded junction under halogen illumination.

graded sample has a better overall photovoltaic response compared with the sample grown on GaSb despite the inclusion of oxygen. The J_{SC} and V_{OC} is approximately 66% higher for the graded photovoltaic cell grown on GaAs compared with the abrupt junction cell grown on GaSb. This result emphasizes the importance of junction quality for optimal photovoltaic performance. The sample with a graded junction has a better quality junction due to a reduction in dislocation densities.

The sub-bandgap response of the ZnTeO graded solar cell was studied using multi-light source current-voltage measurements. The ZnTeO graded solar cell was measured in the dark, under halogen illumination, under 635 nm red laser illumination,

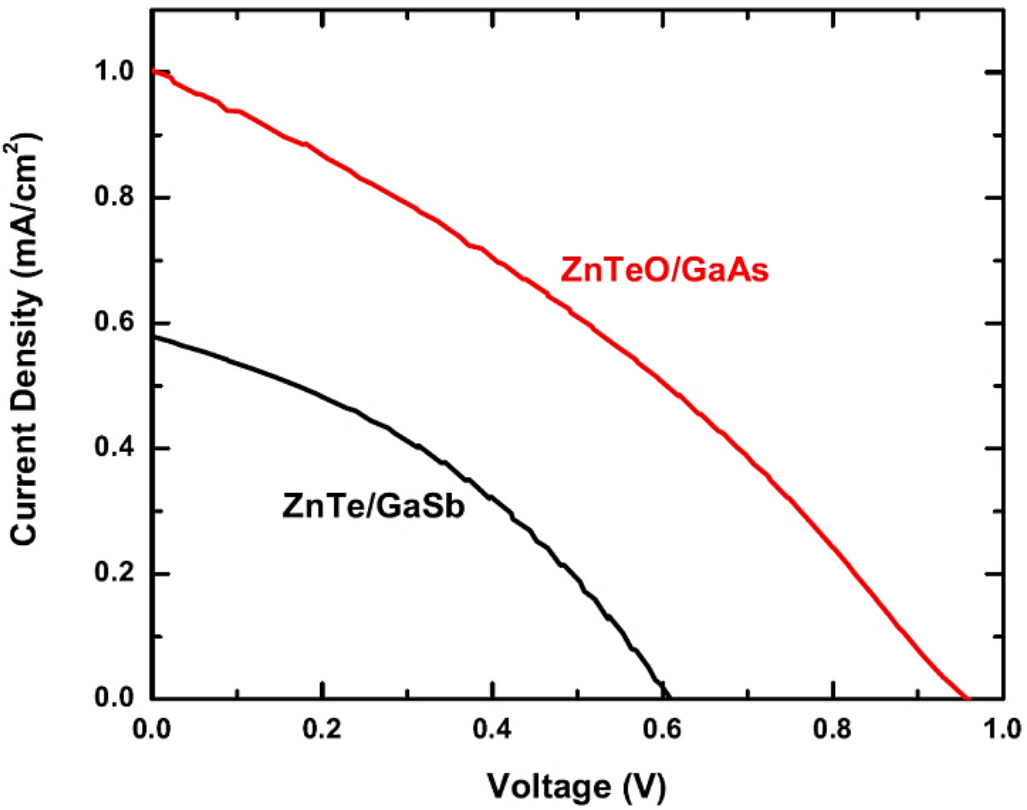

Figure 2.21. Current density versus voltage for a ZnTe/GaSb solar cell and a ZnTeO/GaAs solar cell under AM1.5 illumination.

and under both halogen and 635 nm red laser illumination. The resulting current density versus voltage is shown in Figure 2.22. A photovoltaic response can be observed for the 635 nm red laser illumination since the photon energy is enough to promote carriers from the valence band to the intermediate band and from the intermediate band to the conduction band. The response from illuminating the sample with both halogen lamp and 635 nm laser results in a slight improvement compared with just illuminating the sample with the halogen lamp. This is due to an increased in carrier population at the intermediate band from the 635 nm laser excitation.

When exciting the IBSC with increasing intensities of 635 nm laser excitation, the response saturates as shown in Figure 2.23. As the power density of the 635 nm laser is

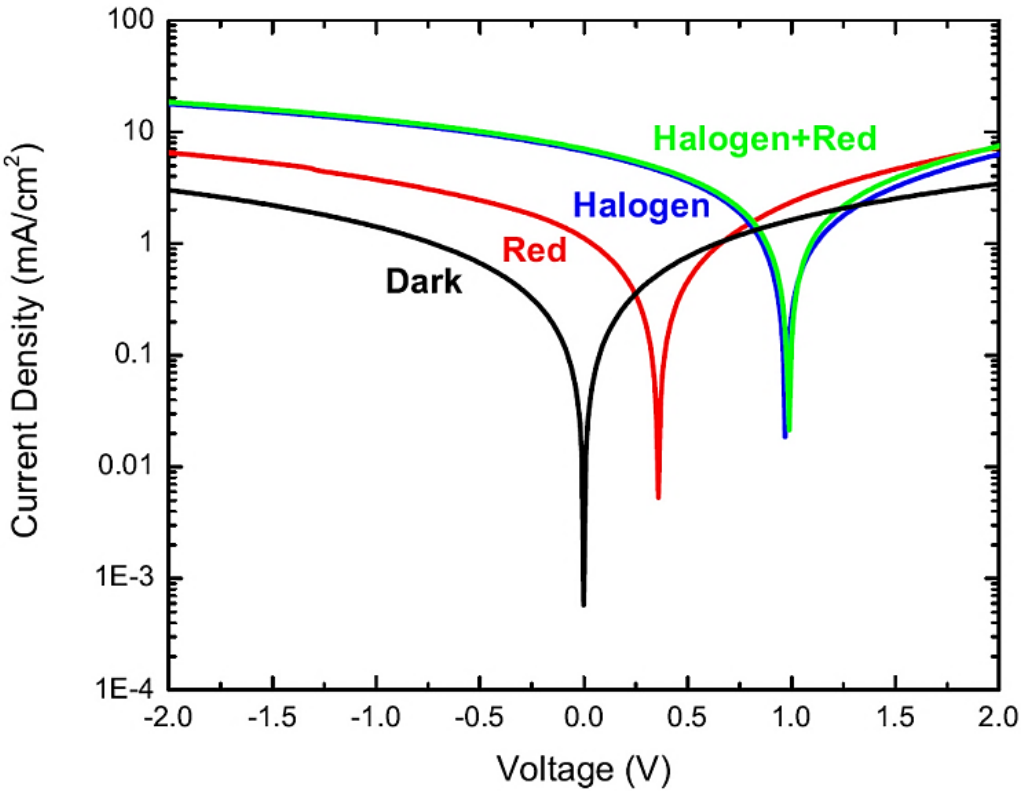

Figure 2.22. Subbandgap response for a p-ZnTeO/n-ZnSe solar cell.

increased, the current density from the sample increases linearly. At a high enough laser power density, the current density saturates. This indicates that the intermediate band has a finite amount of electronic states. Once the electronic states in the intermediate band are filled, the laser can no longer excite extra carriers and the current density stays constant. At that point, the rate of excitation of electrons is equal to the rate of recombination.

This section showed improvements in ZnTe photovoltaic response due to a graded junction with ZnSe. In addition, the saturation of states in the intermediate band was observed.

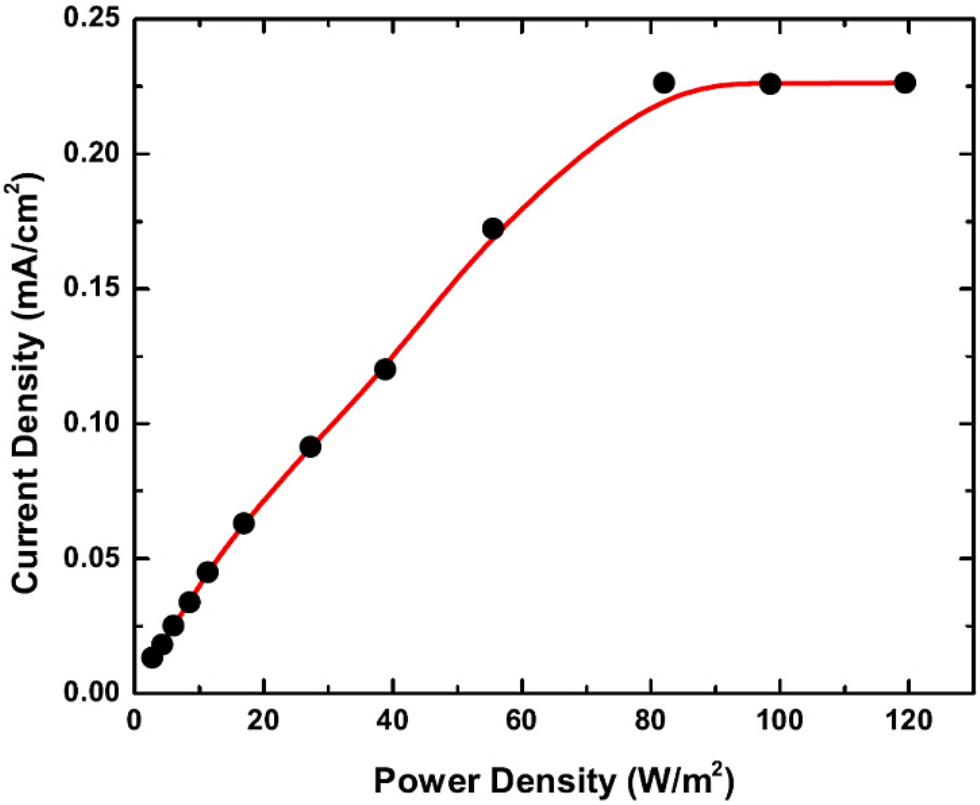

Figure 2.23. Power dependence of sub-bandgap response.

2.5 ZnTe/ZnSe Heterojunction V_{OC} Limitations

The influence of band offsets in II-VI heterojunction diodes on V_{OC} needs to be understood for proper interpretation of device behavior. In order to elucidate the influence of heterojunction band offsets on voltage generation, measurements under solar concentration and low temperature may be used to reduce the influence of material defects on device behavior. In this section, the characteristics of p-ZnTe/n-ZnSe/n-GaAs heterojunction diodes are studied at low temperature under solar concentration, where voltage is limited by band offsets rather than the fundamental bandgap of the ZnTe active

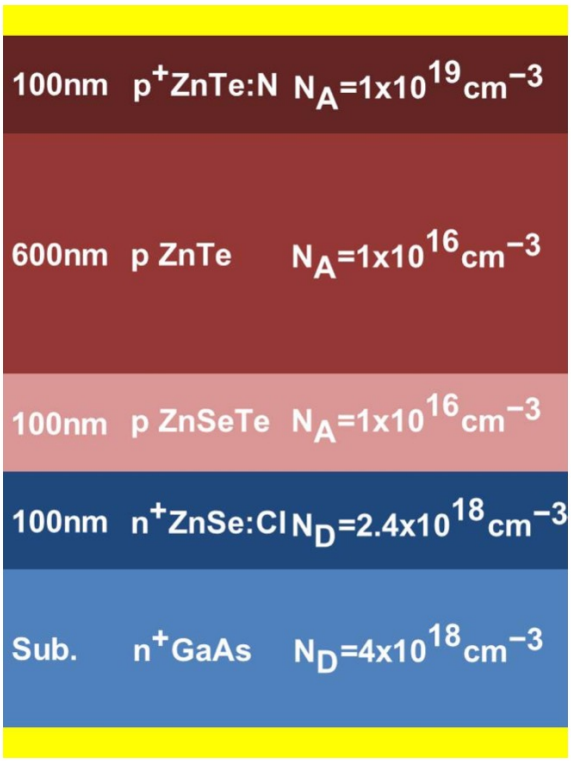

Figure 2.24. Schematic drawing of the p-ZnTe/n-ZnSe device structure and associated layer thickness and doping levels.

region of the device.

Materials were grown by molecular beam epitaxy using solid sources for Zn, Se, and Te on n-type GaAs (0 0 1) substrates. A nitrogen plasma source and solid source $ZnCl_2$ were used for p-type ZnTe:N and n-type ZnSe:Cl doping, respectively. Solar cell devices were fabricated using conventional photolithography, metallization, and etching techniques. The device structure consists of an n-ZnSe emitter layer, undoped ZnSeTe alloy intermediate layer, undoped ZnTe base layer, and p-ZnTe contact layer, as shown in Figure 2.24. The $ZnSe_xTe_{1-x}$ alloy was graded from x = 1 to x = 0 over 100 nm with

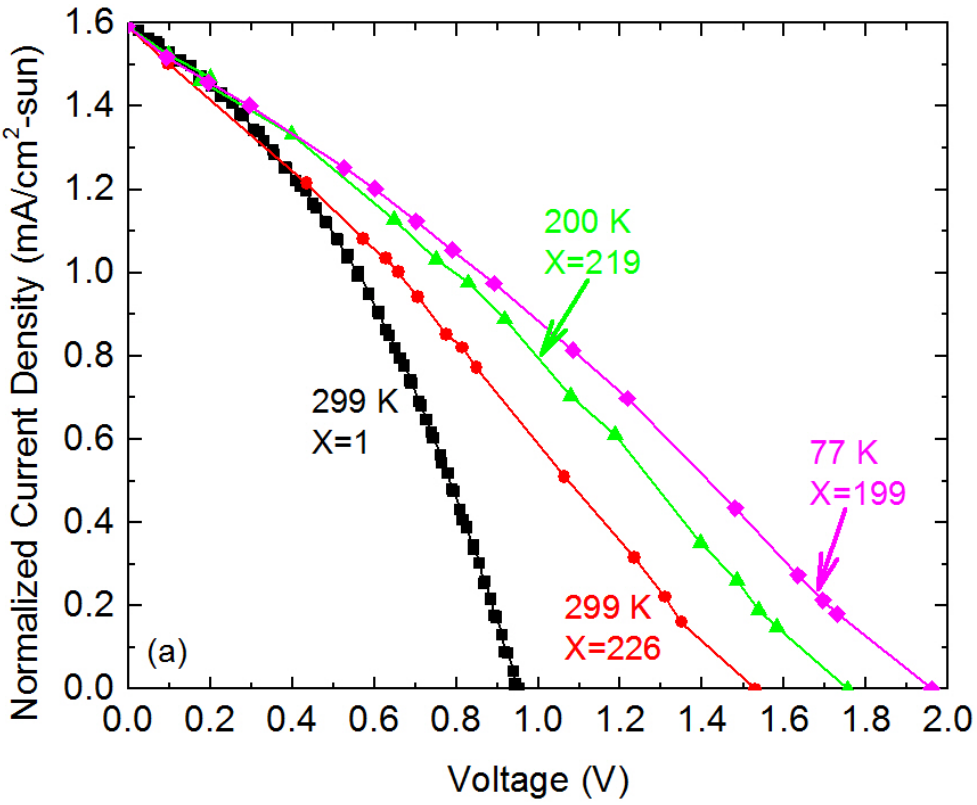

Figure 2.25. Normalized current density versus voltage characteristics under solar concentration and varying temperature. The solar concentration (X) values were calculated by dividing each J_{SC} by $J_{SC}^{AM1.5}$.

the intent of reducing dislocation density by grading the lattice constant [18]. The rate of lattice constant grading is not sufficient to achieve low dislocation density via metamorphic growth, but is necessary to achieve a reasonably abrupt electrical junction.

Current-voltage (I-V) measurements were conducted using a semiconductor device parameter analyzer. Solar concentration measurements were performed using a xenon flash lamp to illuminate the cells. Every point in the concentrated I-V curve was obtained by biasing the sample at a fixed voltage and illumination with a single flash. In order to ensure that every I-V couple was obtained under the same irradiance, a Si

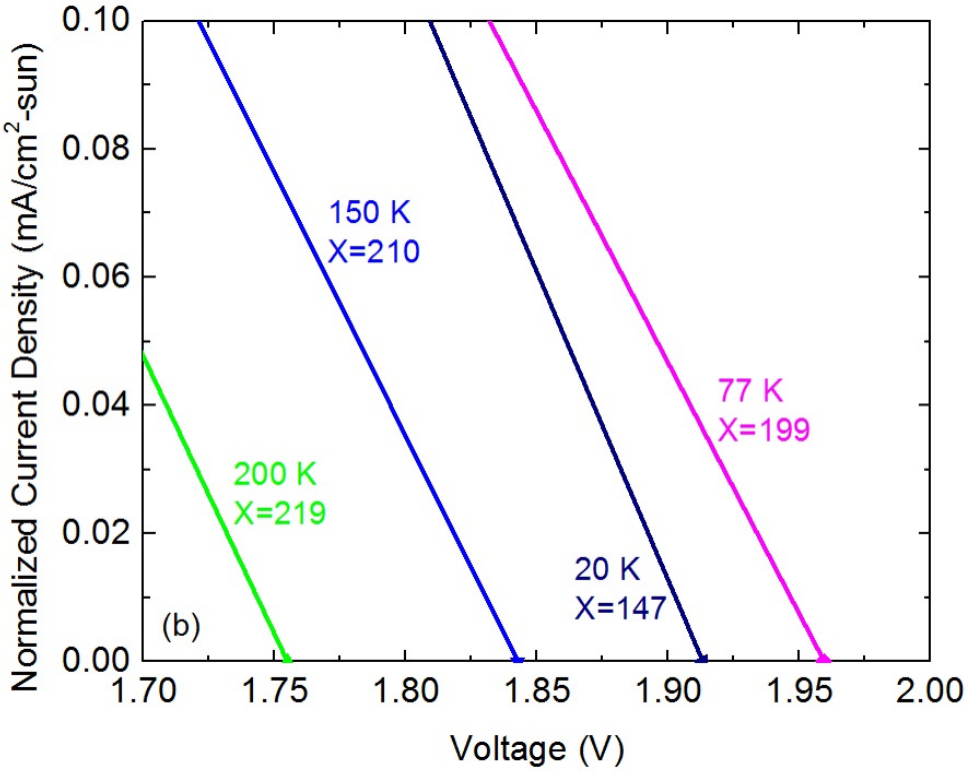

Figure 2.26. Magnified region of the low-temperature curves near V_{OC}.

detector was used to monitor the level of illumination. These measurements were carried out at temperatures ranging from room temperature to 20 K using a closed-cycle He cryostat. Device results were analyzed with the aid of energy band diagrams calculated numerically by finite element methods.

The current-voltage measurements under variable solar concentration and temperature are shown in Figure 2.25 and Figure 2.26. The short-circuit current density J_{SC} was normalized to the 1-sun J_{SC} in order to facilitate the interpretation. The solar concentration values X were calculated by dividing the J_{SC} at concentration by the J_{SC} at 1 sun. The J-V curves exhibit non-ideal fill factors with a shunt path near J_{SC} and parasitic series resistance near V_{OC}. This performance is consistent with past ZnTe diodes

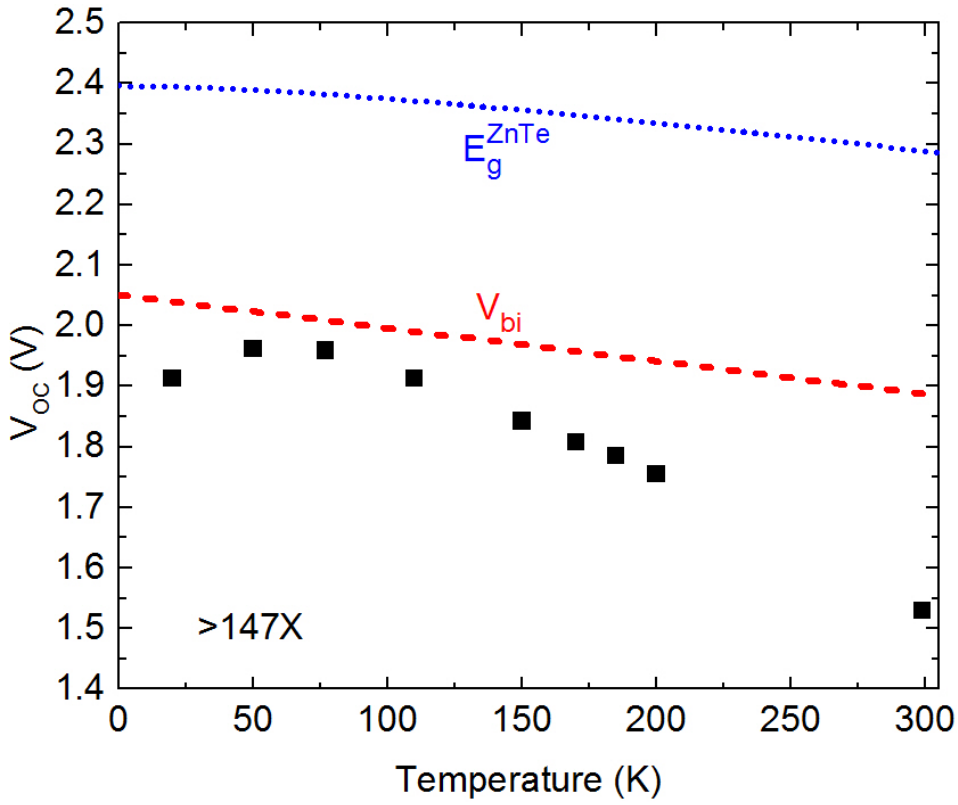

Figure 2.27. Measured V_{OC} versus temperature under solar concentration and comparison with the calculated values for built-in potential and ZnTe bandgap energy. The V_{OC} limit approaches the built-in potential rather than the bandgap energy.

that suffer from series and shunt resistance [6]-[13]. The shunt path is likely due to material defects in the vicinity of the electrical junction. Series resistance is likely limited by the doping level of the n-ZnSe:Cl or electrical contact to the p-ZnTe. As expected, the influence of series resistance is more pronounced at the higher current density under solar concentration. Under solar concentration, the open-circuit voltage increases dramatically, by more than 0.5 V in comparison to 1 sun. This voltage increase is beyond the expected logarithmic increase of voltage with solar concentration. The large V_{OC} increase under solar concentration may be attributed to the reduced influence of non-radiative processes

associated with material defects under high injection levels. The open-circuit voltage increases at reduced temperatures, as shown in Figure 2.27. The V_{OC} increases from 1.54 V at 299 K up to 1.95 V at 77 K. The V_{OC} maintains a value near 1.95 V to around 50 K and then decreases at temperatures near 30 K and below. The reduced V_{OC} at these lower temperatures may be explained by the degradation in charge carrier transport properties. At low temperatures, the increase in dislocation and impurity scattering rates reduces the minority carrier mobility, which reduces the current density [19].

The temperature dependence of V_{OC} can be described by the diode equation under illumination, which is given by

$$J = J_0 \exp\left(\frac{qV}{AkT}\right) - J_{SC} \tag{2.1}$$

where J_0 is the reverse saturation current, q is the electron charge, k is the Boltzmann constant, T is the temperature of the diode, and A is the diode ideality factor. Equation 2.1 can be expanded into

$$J = J_{00} \exp\left(-\frac{E_A}{AkT}\right) \exp\left(\frac{qV}{AkT}\right) - J_{SC} \tag{2.2}$$

where J_{00} is the reverse saturation current density at T = 0 K, and E_A is the activation energy corresponding to the energy barrier that minority carriers must overcome to generate the reverse saturation current. When operating at open circuit, Equation 2.2 can be written as

$$V_{OC} = \frac{AkT}{q} \ln\left(\frac{J_{SC}}{J_{00}}\right) + \frac{E_A}{q}. \tag{2.3}$$

The voltage V_{OC} is determined by the electron and hole quasi-Fermi level splitting, which becomes E_A as T approaches 0 K. In an ideal homojunction solar cell, E_A is the

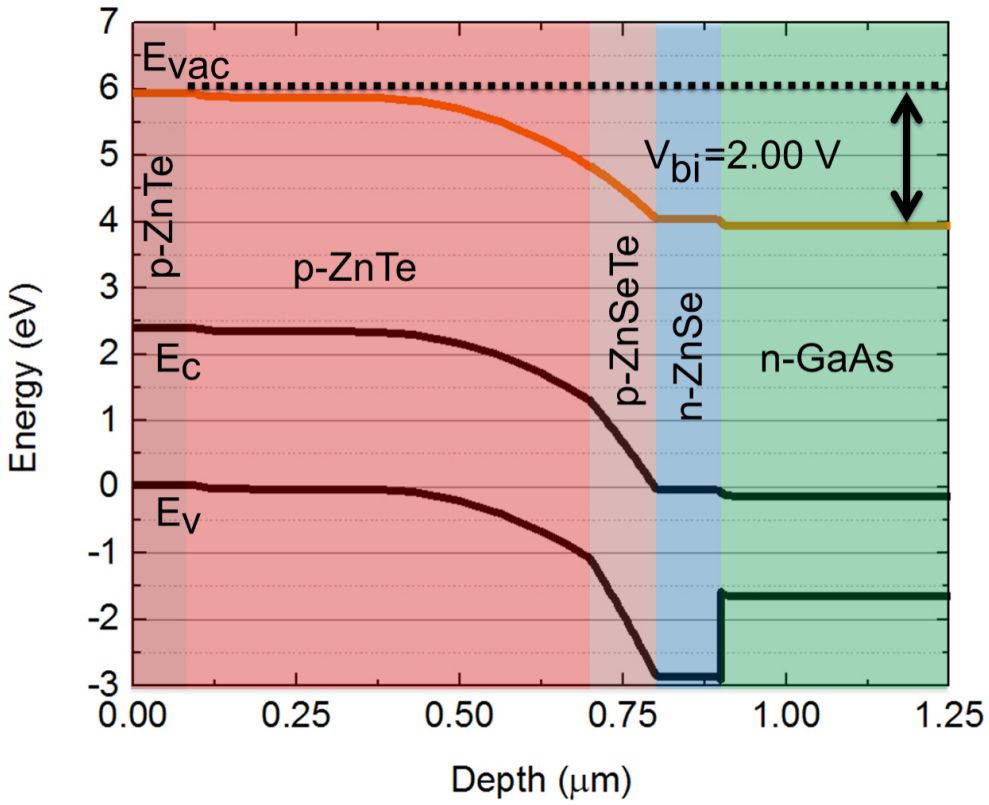

Figure 2.28. Calculated energy band diagrams at 77 K for short-circuit conditions with a built-in potential, as observed at the vacuum level of 2.00 V.

material bandgap E_G. In the case of heterojunction solar cells, the maximum voltage that can develop E_A/q can be limited by the conduction or valence band offset between the two semiconductor materials forming the heterojunction. The band lineup in a heterojunction will define the built-in potential in the conduction or valence band and corresponding limitation on the voltage and electron/hole quasi-Fermi level splitting.

The staggered band lineup for ZnTe/ZnSe results in a reduced built-in potential in the conduction band for a heterojunction in comparison to a homojunction. The calculated energy band diagrams at 77 K under short-circuit conditions and at forward bias near flat-band conditions are shown in Figure 2.28 and Figure 2.29. The built-in

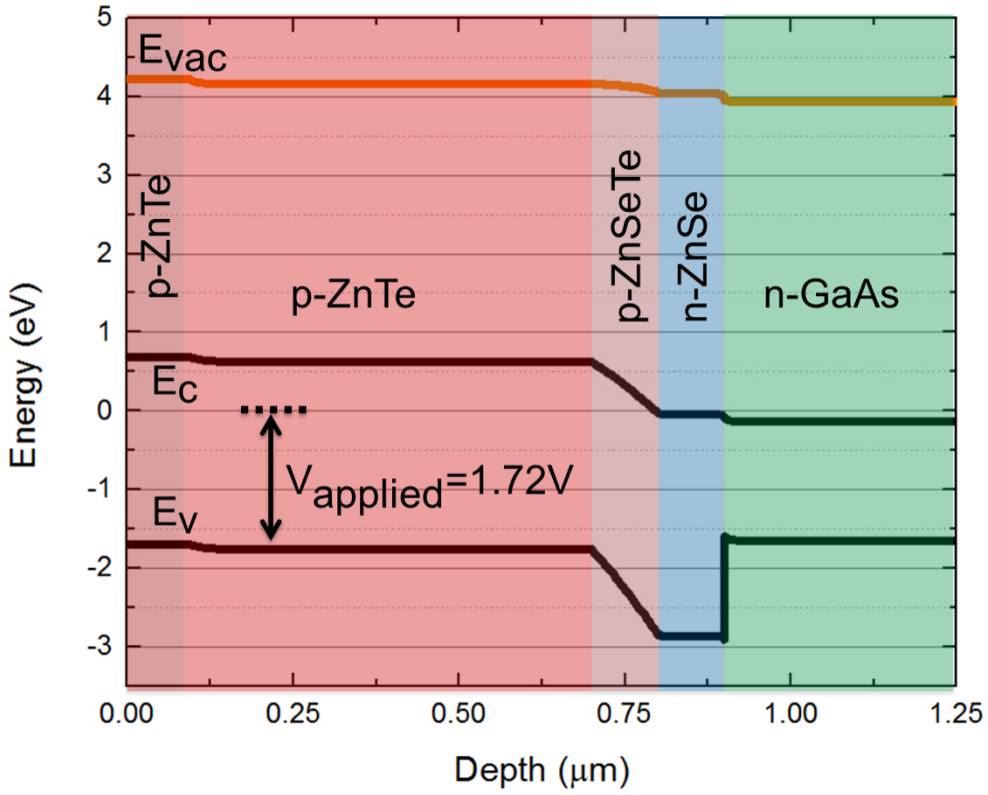

Figure 2.29. Calculated energy band diagrams at 77 K at forward bias of 1.72 V approaching flat-band conditions.

potential at the vacuum level, which will determine E_A and the limit for V_{OC}, is calculated from

$$qV_{bi} = E_g^{ZnTe} - (X^{ZnSe} - X^{ZnTe}) - \left(E_{fp}^{ZnTe} - E_V^{ZnTe}\right) - \left(E_C^{ZnSe} - E_{fn}^{ZnSe}\right) \qquad (2.4)$$

where V_{bi} is the built-in potential, E_G^{ZnTe} is the bandgap of ZnTe, X is the electron affinity, E_{fp}^{ZnTe} is the Fermi level on the p-ZnTe side, E_{fn}^{ZnSe} is the Fermi level on the n-ZnSe side, E_V^{ZnTe} is the top of the valence band on the p-ZnTe side, and E_C^{ZnSe} is the bottom of the conduction band on the n-ZnSe side. The temperature dependence of the built-in potential and ZnTe bandgap is plotted in Figure 2.27 using the Varshni parameters from [20] and the electron affinities for ZnTe and ZnSe from [21]. The

calculated V_{bi} of 2.00 V at 77 K is in strong agreement with the extracted V_{OC} value of 1.95 V from concentration measurements. The built-in voltage, extrapolated to 0 K, reaches a value of 2.05 V. This built-in potential represents the upper limit of V_{OC} for the ZnTe/ZnSe heterojunction solar cell. Prior analysis of organic heterojunctions has suggested that the open-circuit voltage could in fact exceed the built-in potential for device structures where there is an effective force-field barrier [22]. For this to occur, band inversion would be required, and would be unlikely for the case of ZnTe/ZnSe due to the large interface recombination loss at the heterojunction. The calculated energy band diagram under forward bias shown in Figure 2.29 illustrates the device approaching flat-band conditions and an upper limit for V_{OC}. It should be noted that as simulations further approach V_{bi}/V_{OC}, nonphysical results, such as local minima, are observed in the potential profile and are associated with the numerical methods implemented in the simulations.

2.6 Summary

In conclusion, low-temperature solar concentration measurements were performed on p-ZnTe/n-ZnSe solar cells. Increased solar concentration and reduced temperatures demonstrate significant enhancement in open-circuit voltage by overcoming limitations due to nonradiative processes, providing a means to study fundamental limits of the heterojunction device behavior. The limitations on V_{OC} show strong agreement with the calculated built-in potential, rather than the bandgap energy of the ZnTe base region. These experiments demonstrate that large V_{OC} may be demonstrated in ZnTe diodes that

is limited by built-in potential and underscores the importance of identifying heterojunctions with desirable energy band lineups, where low-defect density may be achieved.

Chapter III

GaAs/AlGaAs Indoor Photovoltaics

3.1 Introduction

Low-power electronic circuitry, including wirelessly interconnected sensor nodes, promises to be a transformational technology that can enable unsurpassed interconnectivity and a paradigm shift known as the Internet of Things or Internet of Everything. These low-power systems require a source of energy, ideally from ambient sources. Table 3.1 provides achievable power density levels using various energy harvesting sources. Ambient indoor lighting can provide sufficient energy for most of these applications, with a power density of ~1 $\mu W/mm^2$ under dim lighting conditions.

Power Source	**Power Density**
Photovoltaics (outdoors)	15,000 $\mu W/cm^2$
Photovoltaics (indoors)	10 $\mu W/cm^2$
Thermoelectric (5°C gradient)	40 $\mu W/cm^2$
Piezoelectric (shoe inserts)	330 $\mu W/cm^3$
Vibration (buildings)	300 $\mu W/cm^3$
Ambient radio frequency	< 1 $\mu W/cm^2$

Table 3.1. Energy harvesting sources (adopted from [23]).

Energy-autonomous operation of millimeter (mm)-scale sensors has been previously achieved using photovoltaic cells based on silicon CMOS [24]–[26]. The power requirements for mm-scale computers under active and standby operation are ~10 W and 0.5 nW, respectively [24]–[27]. Sunlight is more than adequate to meet these needs, providing 1 mW/mm^2 of power under full sun, or ~ 100 $\mu W/mm^2$ with a conversion efficiency of 10%. However, stray sunlight is not available in all locations, or at all times. Indoor lighting may also provide sufficient energy, though the intensity and spectral content are significantly different than sunlight. Today, efficient indoor lighting sources, such as light-emitting diodes (LEDs) and fluorescent lamps, provide a relatively narrow band of light in the visible spectral region with a power density on the order of 1 $\mu W/mm^2$ (for an illuminance of ~ 600 lx).

The optical spectrum for indoor lighting is primarily contained in a narrow spectral band in the visible region. The spectrum can also vary depending on the light source (e.g., incandescent, fluorescent, and LED) and color rendering (e.g., warm white and cool white). Fluorescent and LED lighting, in particular, have similar spectral content such that the photovoltaic response will be very similar in both cases. The optimal bandgap energy for a photovoltaic cell for indoor lighting will correspond to the edge of the visible spectrum, and will be larger than the optimal bandgap energy for solar illumination due to the absence of spectral content beyond the visible region. The larger bandgap energy will provide a larger voltage output while also absorbing the full spectrum provided from indoor lighting. Silicon, with bandgap energy of 1.1 eV corresponding to the IR spectral region, is, therefore, smaller than desired for efficient

energy harvesting under indoor lighting conditions. Alternatively, III–V compound semiconductor materials, such as GaAs, provide larger bandgap energy with proven high conversion efficiency and a wide range of accessible spectral windows. While the cost of photovoltaics based on III–V semiconductors is significantly higher than for silicon, and is currently prohibitive for large area solar energy production, the small power requirements and associated size requirements for indoor photovoltaic cells make these materials an affordable option for indoor applications.

Studies of indoor photovoltaics have been reported previously using various technologies, including crystalline silicon [28]–[41], amorphous silicon [28]–[31], [35], [37], [38], [41]–[43], GaAs [28]–[30], [37], [44], InGaP, CdTe [28]–[30], [37], [38], [41], copper indium gallium diselenide [28]–[31], [37], [45], organic [38], [41], [45], and dye-sensitized cells [28]–[30], [38], [41], [45]. Theoretical calculations suggest an optimal bandgap energy of 1.9–2 eV for indoor lighting sources [38], [41] in comparison with the Shockley–Queisser limit of 1.34 eV for AM 1.5 solar illumination [3]. However,

Photovoltaic Technology	**Indoor Efficiency (%)**
Crystalline Silicon	8.2
Amorphous Silicon	7.1
Gallium Arsenide	12.0
Indium Gallium Phosphide	15.8
Cadmium Telluride	10.9
Copper Indium Gallium Diselenide	2.7
Organic	3.6
Dye-Sensitized	6.8

Table 3.2. Indoor efficiency of various photovoltaic technologies.

the dependence of efficiency on lighting intensity, and ultimate energy/power harvesting for mm-scale systems has not been established. In addition to the bandgap energy of the material, which governs the fundamental absorption properties, output voltage, and dark current limitations, the parallel (shunt) resistance for a photovoltaic cell will have strong influence on performance under low-light conditions [28]–[32], [37], [38], [41]. In this chapter, the efficiency and power density limits for energy harvesting under indoor lighting conditions are evaluated, with particular emphasis on the dependence of performance on bandgap energy and illuminance. The design and experimental performance of gallium arsenide (GaAs) and aluminum gallium arsenide (AlGaAs) photovoltaic cells are reported under indoor lighting conditions and compared with crystalline silicon and amorphous silicon photovoltaic cells.

3.2 Efficiency and Power Density Limits

Maximum energy harvesting under indoor lighting conditions was calculated based on detailed balance theory assuming photovoltaic cells with full optical absorption for energy above the material bandgap, radiatively limited performance, and full collection of charge carriers. Three indoor lighting spectra were considered: 1) fluorescent source with daylight color rendering; 2) LED with phosphor; and 3) three-color LED, with spectra given in [46]–[48]. The resulting efficiency values versus bandgap energy are shown in Figure 3.1, comparing the AM 1.5 solar spectrum and various indoor lighting sources with 500 lx intensity. It should be noted that indoor lighting intensity is typically reported in photometric units of lumens or lux, rather than

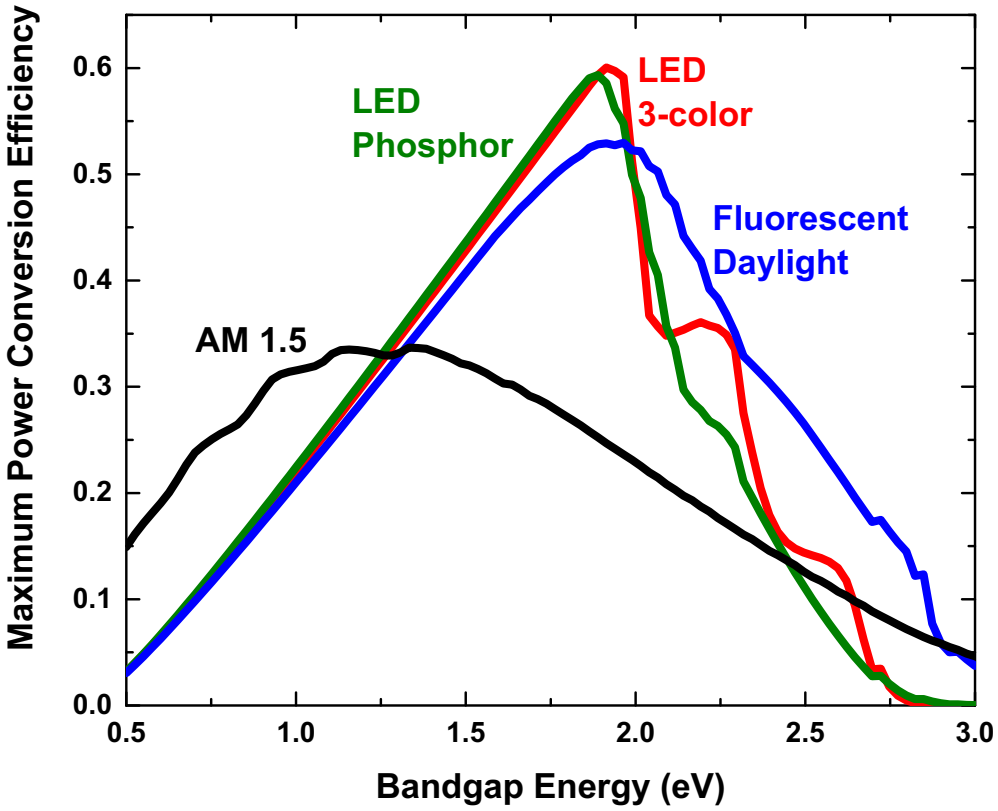

Figure 3.1. Calculated maximum power conversion efficiency versus material bandgap energy under various light sources revealing an ideal bandgap energy near 1.9 eV for indoor conditions.

radiometric units of watts or watts per unit area, respectively. Lighting conditions will be described in terms of lux throughout while also providing corresponding values of radiometric power density for comparison with values typically quoted for solar photovoltaics. Of the three spectra, the maximum efficiency can be obtained for a three-color LED corresponding to bandgap energy of 1.9 eV with an efficiency of 60%. Analysis to compare limiting efficiencies with variable indoor lighting sources has similarly been conducted in [38], where an optimal bandgap energy of 1.9–2 eV was determined. Higher efficiency may be obtained for indoor lighting sources in comparison

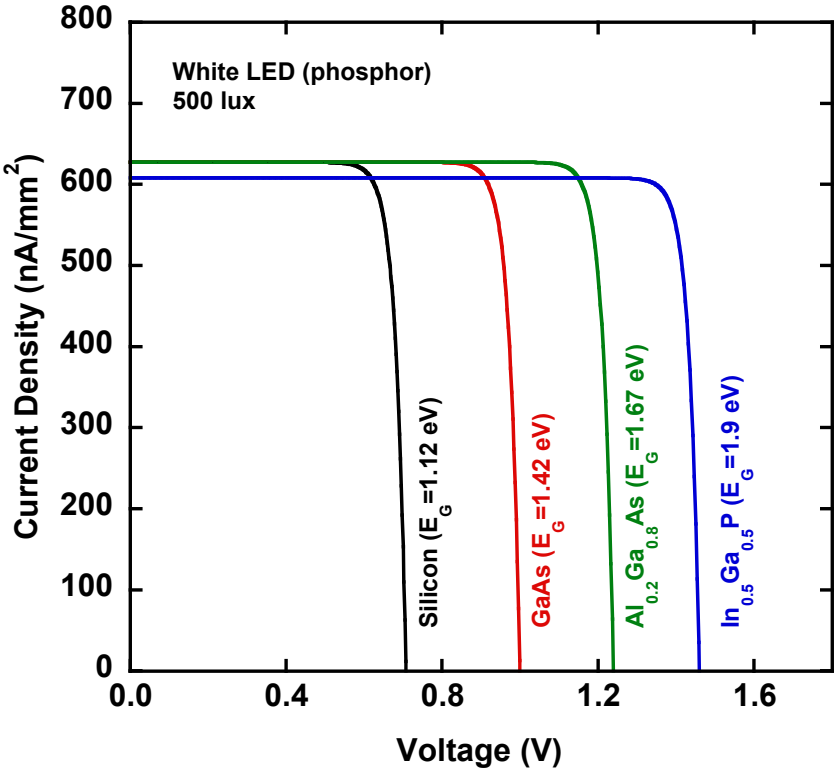

Figure 3.2. Calculated current density versus voltage for various semiconductors under 500 lx illumination.

with sunlight, since the narrower spectral band mitigates transparency losses and thermalization losses associated with the broadband solar spectrum. It should be noted that the conversion efficiency near the peak is relatively independent of the indoor lighting source. While higher conversion efficiency may ultimately be achieved for indoor lighting relative to sunlight, the actual light intensity is significantly lower (1–2 W/m^2). $In_{0.5}Ga_{0.5}P$ has a bandgap energy of 1.9 eV, matching the ideal for indoor photovoltaics. Studies have shown an experimental maximum efficiency under fluorescent lighting of 16% using InGaP photovoltaic cells [38], [41].

The calculated current density versus voltage and power density versus voltage is

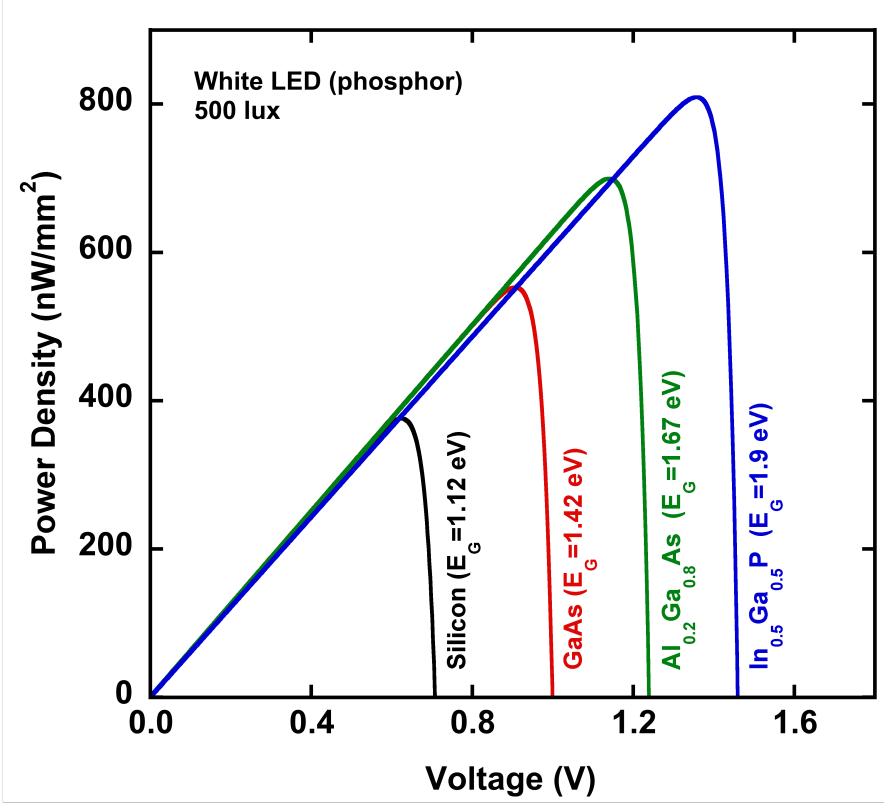

Figure 3.3. Calculated power density versus voltage for various semiconductors under 500 lx illumination.

shown in Figures 3.2 and 3.3, respectively, for select bandgap energies. The selected bandgap energies are those of Si, GaAs, $Al_{0.2}Ga_{0.8}As$, and $In_{0.5}Ga_{0.5}P$ because they are viable options for indoor photovoltaic technologies. All four materials have similar current densities, greater than 600 nA/mm^2, since they absorb all of the photons from the indoor spectra. The larger bandgap materials have larger operating voltages which results in larger maximum power densities of up to 800 nW/mm^2 at 500 lx illumination.

The dependence of power density on indoor lighting illuminance is perhaps the most relevant figure for mm-scale systems. A comparison of maximum achievable power density versus illuminance for select bandgap energies is shown in Figure 3.4. For these

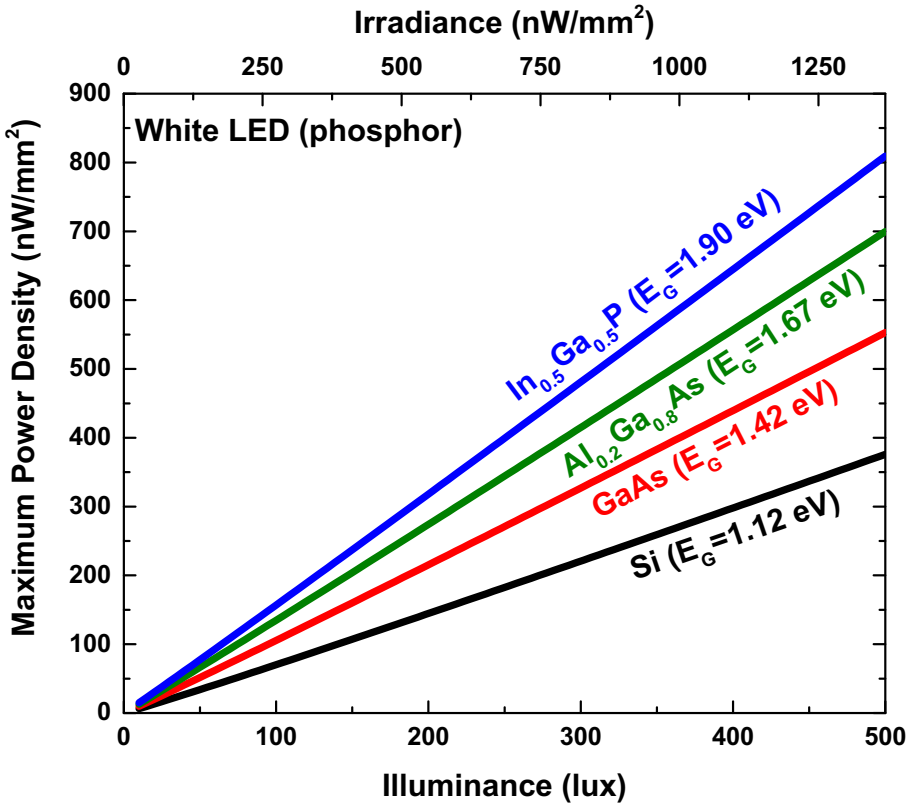

Figure 3.4. Calculated maximum power density versus illuminance for select materials under white phosphor LED illumination, illustrating that target goals of >100 nW in a 1 mm^2 area may be reasonably achieved.

relatively standard indoor lighting conditions, a power density > 100 nW/mm^2 can be obtained. The analysis also underscores the large improvements in energy harvesting that may be achieved by considering materials with larger bandgap energy than silicon. The analysis described assumes perfect optical absorption and carrier collection, and does not consider material-specific parameters and how they would influence device design and conversion efficiency.

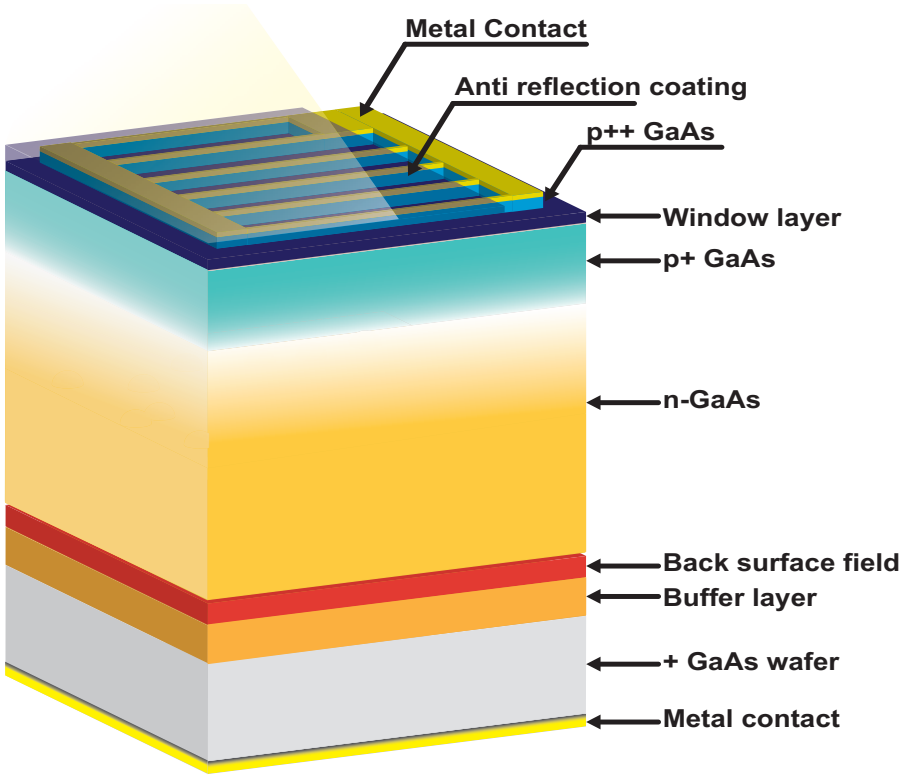

Figure 3.5. Photovoltaic cell structure for the GaAs and $Al_{0.2}Ga_{0.8}As$ devices.

3.3 Experimental Results

The influence of the indoor lighting spectrum on photovoltaic energy conversion efficiency was investigated experimentally for materials with varying bandgap energy, including GaAs, and $Al_{0.2}Ga_{0.8}As$ photovoltaic cells. The fabricated GaAs and $Al_{0.2}Ga_{0.8}As$ cells had an active area of 1 mm^2. GaAs cell design and fabrication has been reported in [49] and is shown in Figure 3.5, where the $Al_{0.2}Ga_{0.8}As$ photovoltaic cells had a similar design, but with the addition of Al to the emitter and base layers. The cells had had a base layer thickness of 0.7 μm with a doping level of 5 x 10^{17} cm^{-3}.

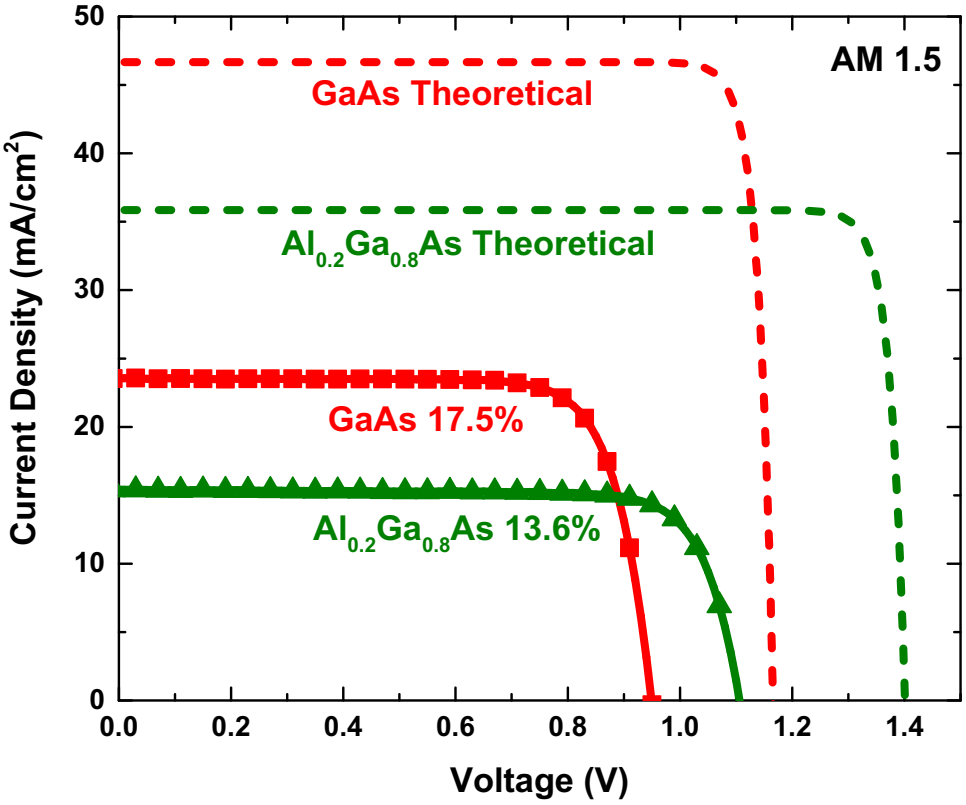

Figure 3.6. Measured and theoretical current density versus voltage of $Al_{0.2}Ga_{0.8}As$ and GaAs cells under AM 1.5 illumination.

The electrical performance of the $Al_{0.2}Ga_{0.8}As$ and GaAs photovoltaic cells was measured under both the simulated AM 1.5 solar spectrum and indoor lighting conditions using a white phosphor LED. All of the measurements were performed at room temperature. The results under one-sun illumination are shown in Figure 3.6 along with the theoretical photovoltaic response. The GaAs cell outperformed the $Al_{0.2}Ga_{0.8}As$ solar cell with power conversion efficiencies of 17.5% and 13.6%, respectively. While these photovoltaic cells by no means have record power conversion efficiency, they possess respectable efficiencies that may be used for qualitative comparison purposes.

The $Al_{0.2}Ga_{0.8}As$ cell performed the best when illuminated with a white phosphor

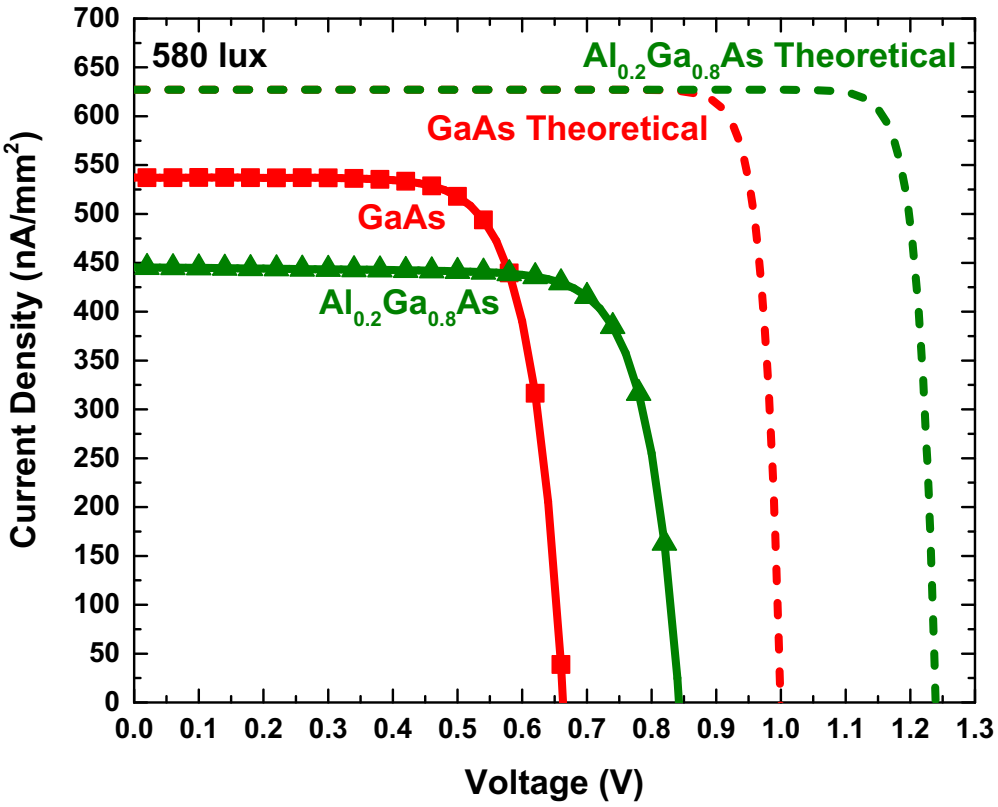

Figure 3.7. Measured and theoretical current density versus voltage of $Al_{0.2}Ga_{0.8}As$ and GaAs cells under white LED illumination.

LED, as shown in Figure 3.7. Measured results demonstrate nearly ideal short-circuit current but show a substantial drop in open-circuit voltage compared with theoretical calculations. The drop in V_{OC} will be further discussed in section 3.4. Maximum power densities > 250 nW/mm^2 were achieved under typical indoor lighting conditions (580 lx), as shown in Figure 3.8. Under these conditions, the $Al_{0.2}Ga_{0.8}As$ cell had the highest power conversion efficiency of 21.1%. To the best of our knowledge, this is the highest reported photovoltaic power conversion efficiency for indoor lighting. The GaAs cell demonstrated a power conversion efficiency value of 19.4%, under LED illumination at 580 lx. The efficiency values were calculated using measured luminous efficacy of

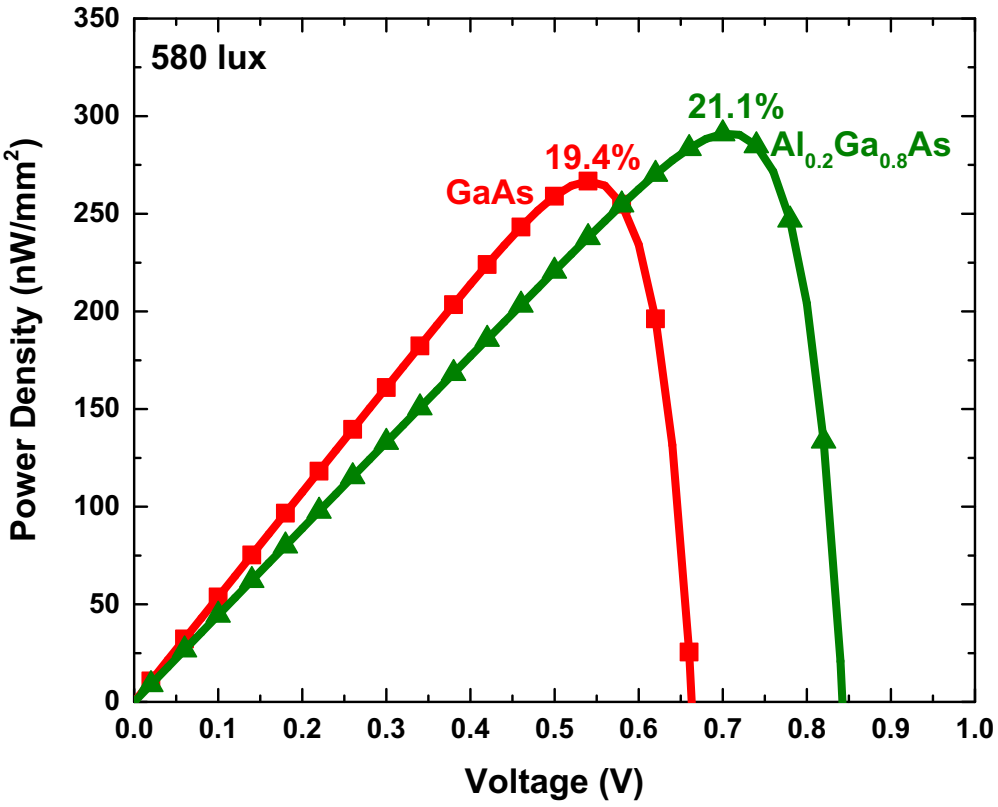

Figure 3.8. Measured power density versus voltage of $Al_{0.2}Ga_{0.8}As$ and GaAs cells measured under white LED illumination.

radiation of the white phosphor LED used for these measurements. The spectral characteristics of the white phosphor LED is shown in Figure 3.9 along with the luminosity function. The luminous efficacy of radiation is calculated by taking the inner product of the irradiance and luminosity function resulting in a value of 420 lm/W for the LED used in these experiments.

The performance of the fabricated photovoltaic cells was compared with commercial silicon (Si) [50] and amorphous silicon (a-Si) [51] solar cells. The maximum power density versus illuminance is shown in Figure 3.10. Under extremely dim lighting conditions (less than 200 lx), the GaAs-based photovoltaic cells achieved power densities

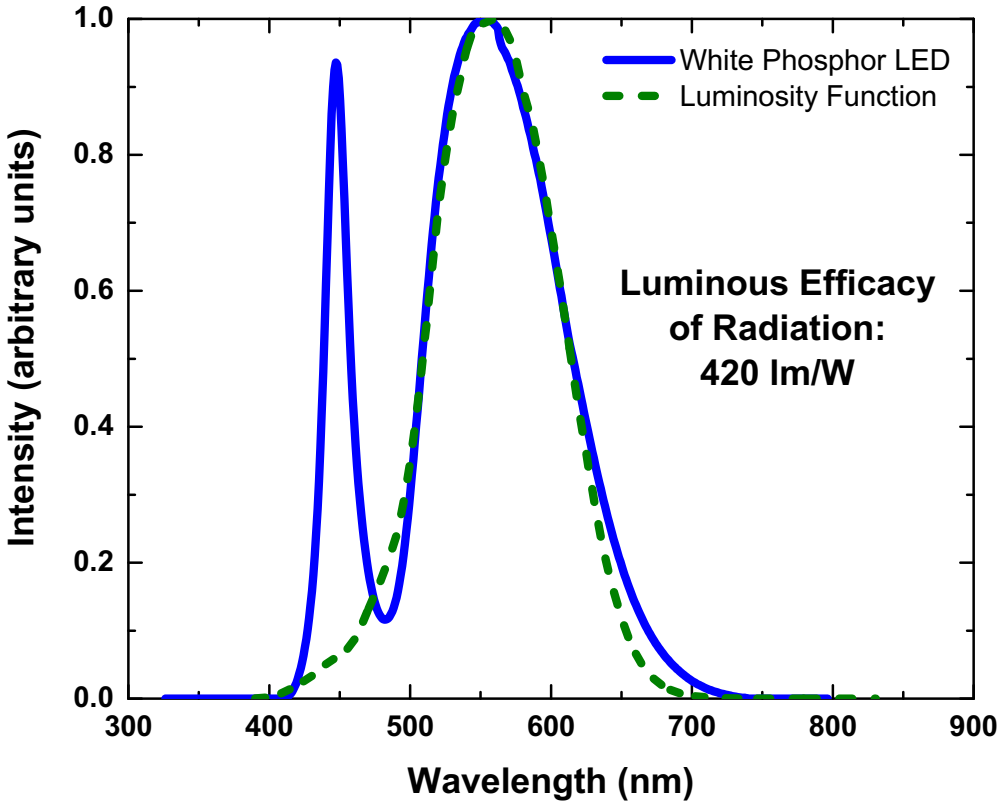

Figure 3.9. Measured spectral content of the white phosphor LED used and luminosity function. The luminous efficacy of radiation is calculated by taking the inner product of the irradiance and luminosity function.

greater than 100 nW/mm^2. The commercial a-Si and Si solar cells required illuminance greater than 500 lx to achieve power densities greater than 100 nW/mm^2. The dependence of illuminance on power conversion efficiency is shown in Figure 3.11. High power conversion efficiency is maintained by the GaAs and $Al_{0.2}Ga_{0.8}As$ photovoltaic cells for dim lighting conditions (greater than 15% at 100 lx). The a-Si and Si solar cells had efficiencies under 10% throughout the measurement range.

The importance of cell performance at low illuminance is illustrated by the dependence of open-circuit voltage (V_{OC}) and fill factor on illumination, as shown in

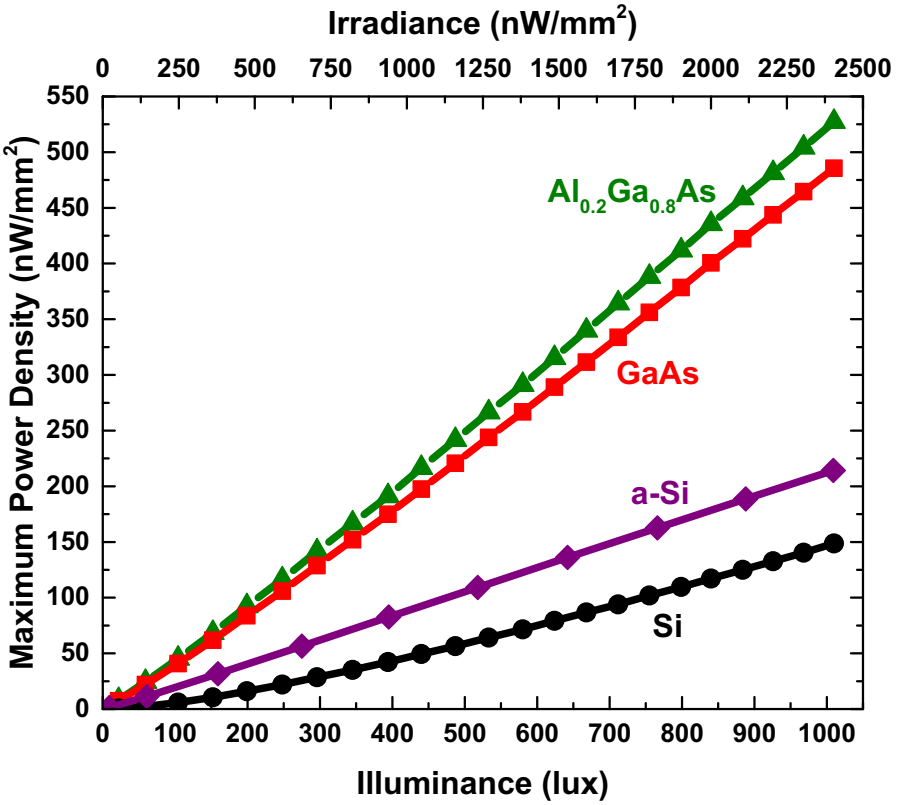

Figure 3.10. Measured maximum power density versus illuminance of $Al_{0.2}Ga_{0.8}As$ and GaAs cells measured under white LED illumination and comparison to commercial a-Si and Si solar cells.

Figure 3.12 and Figure 3.13, respectively. For a drop in illuminance from 1000 to 20 lx, the $Al_{0.2}Ga_{0.8}As$ and GaAs photovoltaic cells exhibit a decrease in V_{OC} of 21% and 26% along with a decrease in fill factor of 6% and 7% respectively. In comparison, the commercial Si solar cell suffers a 75% decrease in V_{OC} and a 52% decrease in fill factor. The commercial a-Si solar cell exhibits a decrease in V_{OC} of 23% but maintains fill factor at lower illumination levels.

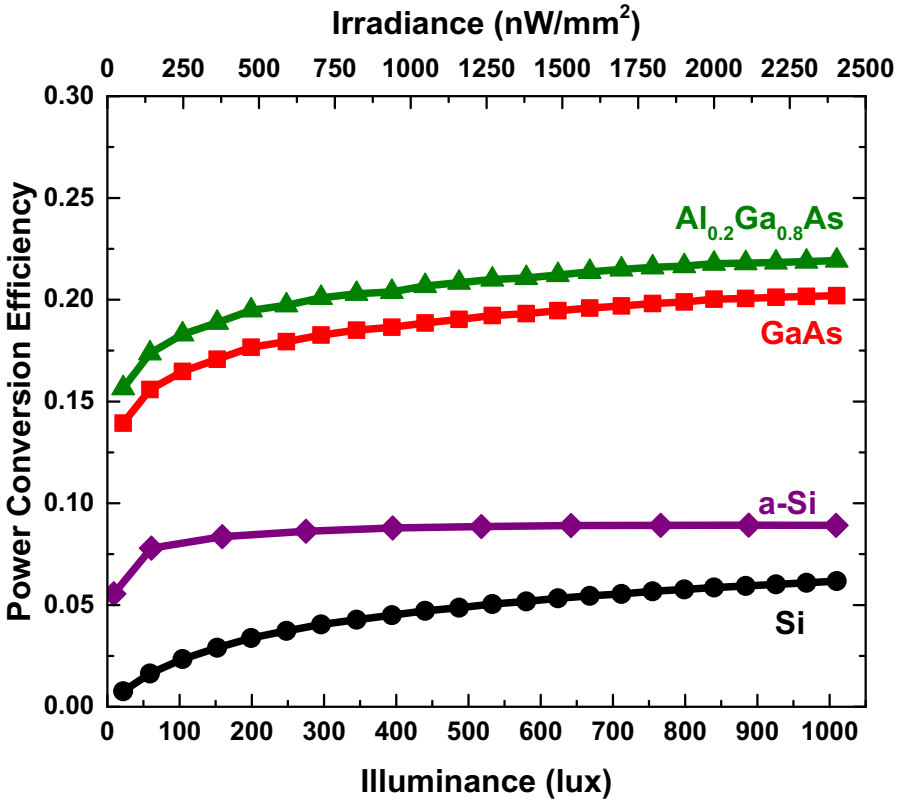

Figure 3.11. Measured power conversion efficiency versus illuminance of $Al_{0.2}Ga_{0.8}As$ and GaAs cells measured under white LED illumination and comparison to commercial a-Si and Si solar cells.

3.4 Discussion

Under typical indoor lighting conditions, the GaAs-based photovoltaic cells outperformed the commercial crystalline Si and amorphous Si solar cells, where there is a dramatic decrease in fill factor and efficiency for the crystalline Si cell for indoor lighting in comparison with one-sun illumination. The four photovoltaic cells demonstrated a relatively similar short-circuit current density (J_{SC}) under indoor conditions relative to AM 1.5 illumination, with some degree of variability related to optical absorption and carrier collection. However, the V_{OC} varies dramatically, following the trend of decreasing V_{OC} with material bandgap energy. The $Al_{0.2}Ga_{0.8}As$

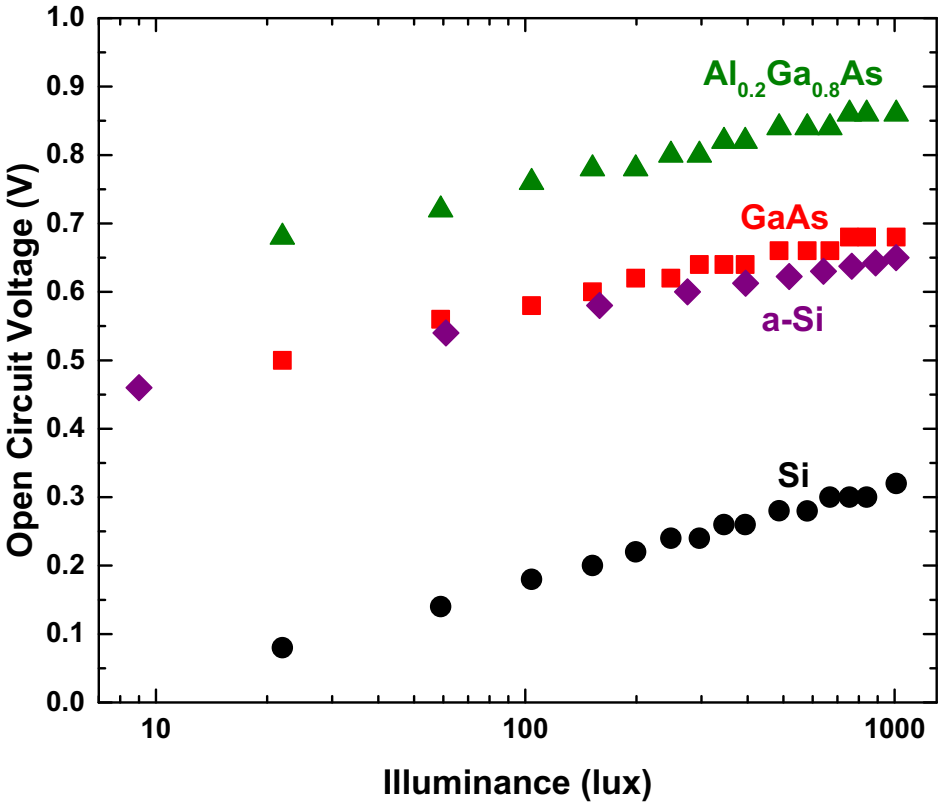

Figure 3.12. Open-circuit voltage versus illuminance of $Al_{0.2}Ga_{0.8}As$ and GaAs cells measured under white LED illumination and comparison to commercial a-Si and Si solar cells illustrating V_{OC} degradation at low illumination due to dark current and shunt leakage.

cell delivered the highest maximum power density and power conversion efficiency primarily due to the larger bandgap energy of the absorber material and similar fill factor to the GaAs cells. The V_{OC} reduction of the crystalline silicon cell with respect to the one-sun condition is dramatically higher than expected based on the logarithmic relation with light intensity. Performance degradation under low-light conditions has similarly been reported for crystalline silicon, and attributed to parasitic shunt current leakage [28]–[32], [37], [38], [41], which is observed in the current silicon cell via the low fill factor, as shown in Figure 3.12.

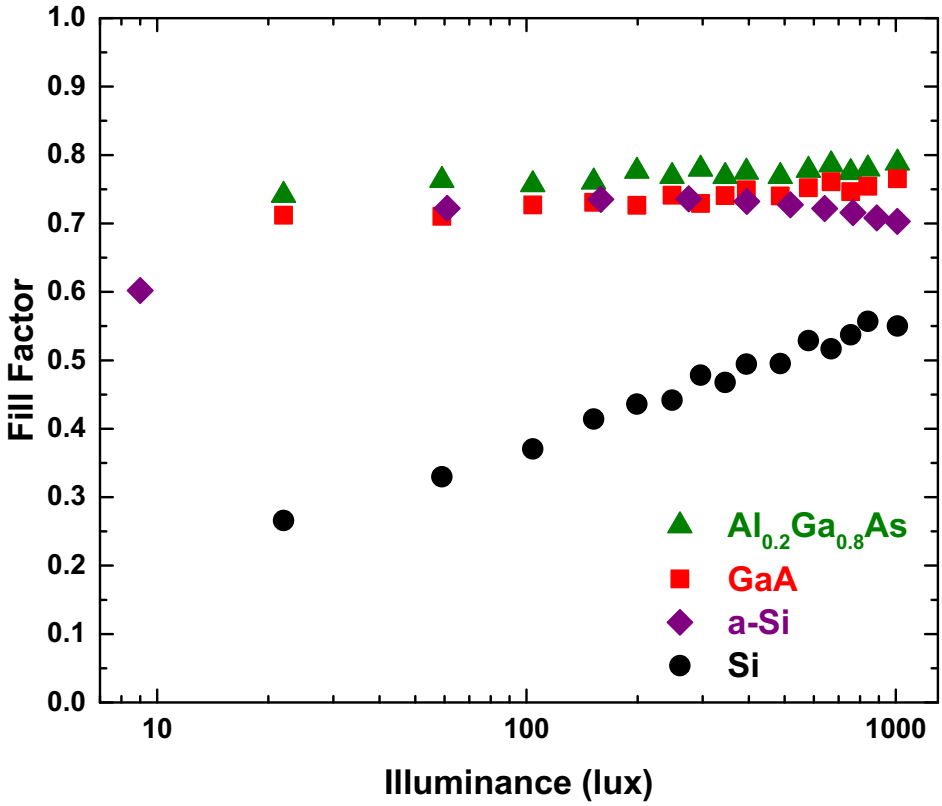

Figure 3.13. Fill factor versus illuminance of $Al_{0.2}Ga_{0.8}As$ and GaAs cells measured under white LED illumination and comparison to commercial a-Si and Si solar cells illustrating FF degradation at low illumination due to dark current and shunt leakage.

Light-harvesting efficiency (LHE) can be reported as standard radiometric power conversion efficiency, or more conveniently, as photometric power conversion efficiency in watt/lumen. These two are related by the luminous efficacy of the light source (420 lm/W in this study). Continued study of photovoltaic indoor light harvesting should also include the development of standardized test conditions analogous to those developed for solar cells. An LHE of 0.1 mW/lm (4.6% power conversion efficiency) or greater would be able to power mm-scale sensors with photovoltaic cells of similar dimensions [24]-[27]. The experimental dependence of LHE on illuminance is shown in Figure 3.13. The

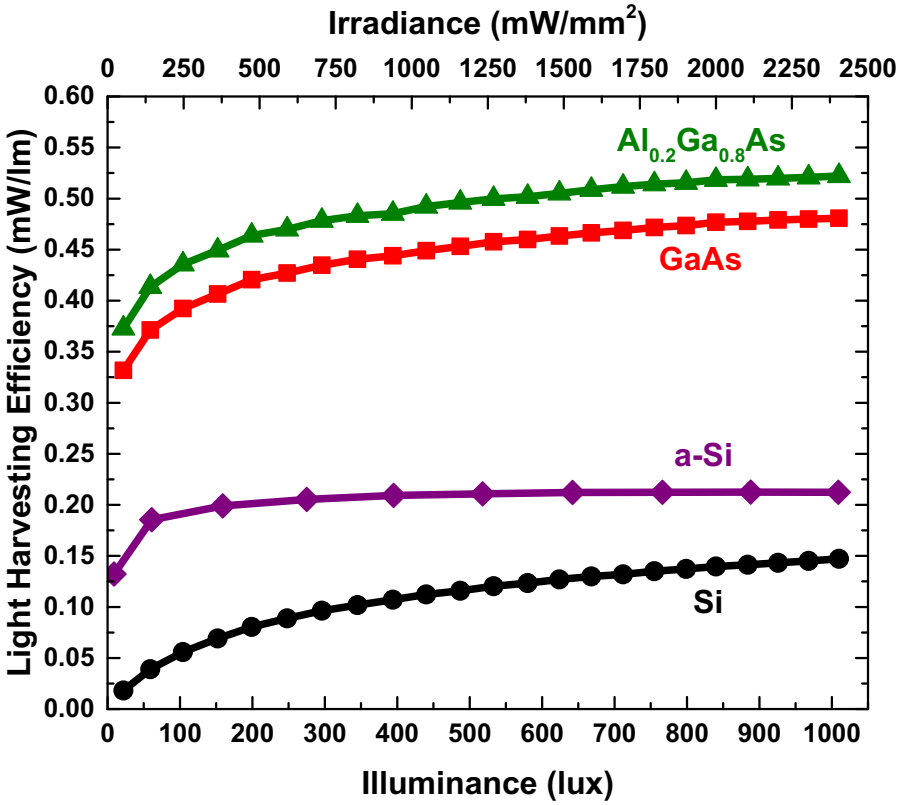

Figure 3.14. Measured LHE versus illuminance of $Al_{0.2}Ga_{0.8}As$ and GaAs cells measured under white LED illumination and comparison to commercial a-Si and Si solar cells.

$Al_{0.2}Ga_{0.8}As$ cell has the highest LHE, followed by the GaAs cell, the commercial a-Si cell, and the commercial Si cell. Reduced cell efficiency at low illuminance can be attributed to either dark current or parasitic shunt current [28]–[32], [37], [38], [41]. The current density voltage relations for a diode photovoltaic cell are described by

$$J = J_L - J_O\left[\exp\left(\frac{qV}{nkT}\right) - 1\right] - \frac{V}{R_{SH}} \tag{3.1}$$

where J is the current density, J_L is the photogenerated current density, J_0 is the dark saturation current density, q is the electron charge, V is the voltage across the cell terminals, n is the diode ideality factor, k is the Boltzmanns constant, T is the

temperature, and R_{SH} is the cell shunt resistance. Under sufficiently high illumination conditions, such as one-sun illumination, the current shunt represented by V/R_{SH} is negligible in comparison with the generated photocurrent, while the dark current is negligible for voltages significantly below V_{OC}. Under low illumination conditions, such as indoor lighting, the proportional decrease in J_L can become comparable with V/R_{SH} and J_0, resulting in a dramatic reduction in V_{OC}, fill factor, and subsequent LHE. Studies have shown a significant perimeter recombination effect in GaAs-based solar cells of large perimeter-to-area ratio (P/A) [52]–[54]. The perimeter recombination effect dominates the dark current component under low illumination, degrading fill factor. Such an effect is expected for the photovoltaic cells in this paper given their large P/A and the low illumination conditions during measurements.

Prior experimental results on photovoltaic cells exhibit a decrease in power conversion efficiency under the reduced intensity of indoor lighting conditions, despite the detailed balance predictions for higher efficiency associated with more efficient utilization of the narrow spectral band of indoor lighting relative to sunlight. The relatively low shunt resistance in crystalline silicon is well known, where materials with high parallel resistance, such as amorphous silicon and CdTe, have been shown to provide improved performance under low-light conditions despite reduced efficiency under one-sun conditions [28]–[31], [37], [38], [41]. However, a-Si and CdTe cells have thus far exhibited a net decrease in power conversion efficiency for indoor lighting with respect to AM 1.5 illumination. The AlGaAs and GaAs cells in this paper exhibit a substantial increase in power conversion efficiency under indoor lighting conditions,

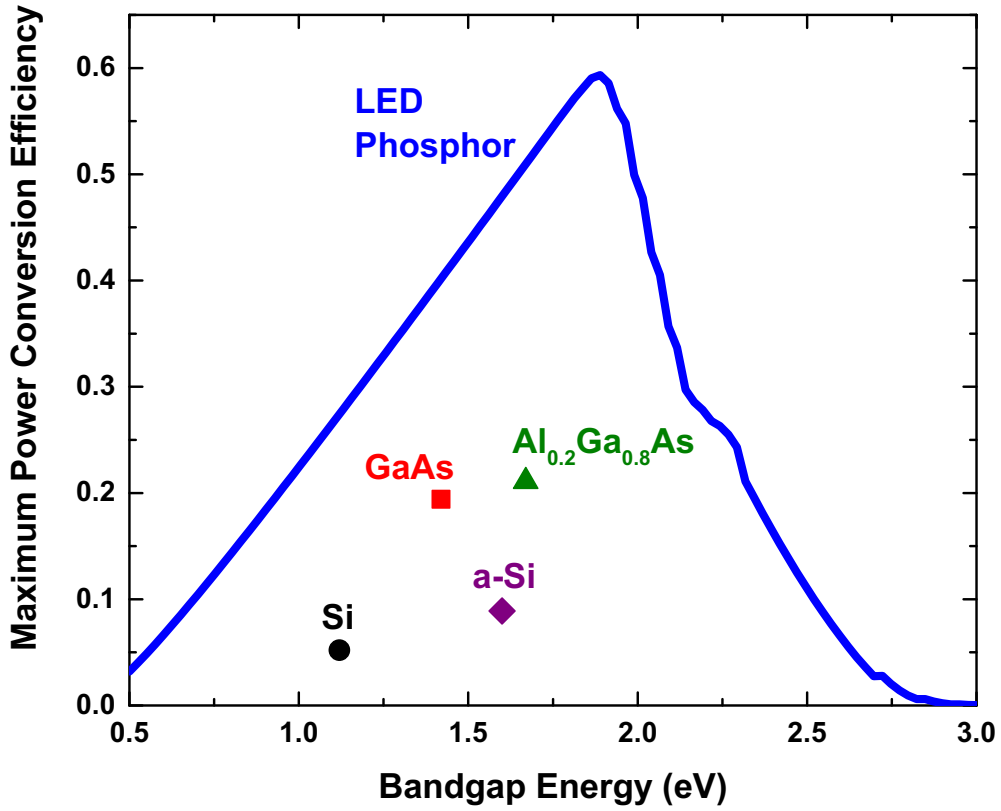

Figure 3.15. Calculated maximum power conversion efficiency versus material bandgap under white LED illumination along with measured efficiencies for fabricated $Al_{0.2}Ga_{0.8}As$ and GaAs cells and commercial a-Si and Si cells.

demonstrating a breakthrough for energy harvesting of indoor lighting. Figure 2.15 shows the measured maximum power conversion efficiencies for the materials in this study along with the calculated theoretical maximum values. The measured power conversion efficiency for the GaAs and AlGaAs cells is still well below the theoretical detailed balance limit (~ 50%), suggesting that there is still substantial opportunity for improvement. This result also underscores the importance of understanding mechanisms for dark current and shunt leakage in these devices and the dependence on material properties and device fabrication processes.

3.5 Summary

Perpetual operation of mm-scale systems that require an average power density of 10 nW/mm^2 can be achieved using photovoltaics for light harvesting under typical indoor lighting conditions. A maximum theoretical power conversion efficiency of 60% can be achieved under typical indoor lighting by a semiconductor with a 1.9-eV bandgap energy. Commercial a-Si, Si, and fabricated GaAs-based photovoltaic cells were measured under typical indoor lighting conditions, demonstrating LHE ~ 0.1 and 0.5 mW/lm, respectively. While crystalline silicon cells exhibit a sharp degradation in efficiency at low illuminance, the GaAs, and $Al_{0.2}Ga_{0.8}As$ cells maintain high efficiency, which can be attributed to low dark current levels and relative insensitivity to shunt current leakage. The $Al_{0.2}Ga_{0.8}As$ cell demonstrated the highest reported indoor power conversion efficiency of 21%. The combination of high power conversion efficiency and insensitivity to low-illuminance conditions suggest that AlGaAs photovoltaics are highly promising for energy harvesting in mm-scale wireless sensor nodes.

Chapter IV

Sources of Loss in Indoor Photovoltaics

4.1 Introduction

In the previous chapter the performance of indoor photovoltaic technologies was studied and compared. A record power conversion efficiency of 21% was obtained using an $Al_{0.2}Ga_{0.8}As$ photovoltaic cell under indoor lighting conditions. This efficiency is enough to power mm-scale systems but is far from the theoretical maximum calculated in the previous chapter. This chapter will explore the sources of loss in indoor photovoltaics by studying the external quantum efficiency (EQE), dark current, and shunt resistance of GaAs and $Al_{0.2}Ga_{0.8}As$ photovoltaic cells. Studying EQE will allow us to identify the deficiencies leading to smaller short-circuit current. By analyzing perimeter/area-dependent measurements of dark current and shunt resistance we will be able to identify which factors affect open-circuit voltage under dim indoor lighting conditions. The effects of perimeter recombination on dark current and shunt resistance will be discussed followed by a discussion on the use of surface passivation technologies in order to reduce perimeter recombination rates.

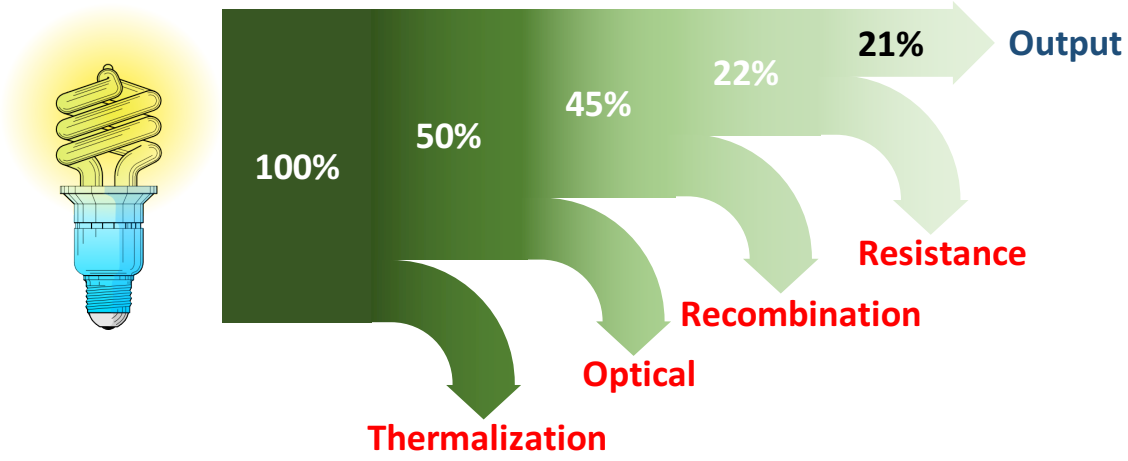

Figure 4.1. Indoor photovoltaic loss mechanisms.

4.2 Sources of Loss

In order to improve the design and performance of GaAs-based indoor photovoltaics, the main mechanisms of loss need to be studied. Figure 4.1 summarizes the main sources of loss in indoor photovoltaics. The energy from the indoor illuminance is denoted on the left by 100%. Four main loss mechanisms reduce the total energy delivered to the output to 21%. The four main loss mechanisms are thermalization, optical, recombination, and resistance. Since the spectra of indoor light is narrow and contains photons with energies greater than the bandgap energies of GaAs and $Al_{0.2}Ga_{0.8}As$, there are no transparency losses in indoor photovoltaics. This is in contrast to traditional solar photovoltaics where transparency losses are crucial.

Thermalization losses result from photons with energies greater than the bandgap

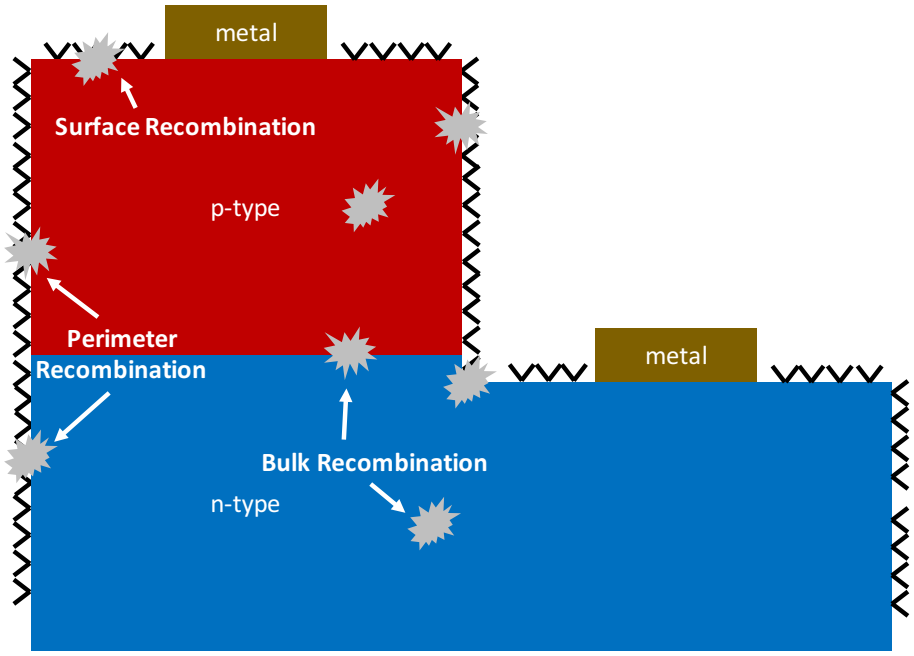

Figure 4.2. Recombination mechanisms in p-n junction photovoltaic cells.

exciting carriers to high energy levels. The excited carriers then release their excess energy through thermal processes. The excess energy is then lost. Optical losses result from the shadowing of active area by metal contacts and the reflection of photons from the front surface. Photons that are blocked and reflected are not absorbed, resulting in a loss of energy.

Figure 4.2 summarizes recombination losses which result from excited carriers recombining before they are collected. Recombination can occur in the bulk of the device but most detrimental recombination mechanisms occur at the surface and perimeter of the device. The influence perimeter recombination currents on GaAs-based photovoltaic devices have been well documented demonstrating a strong degradation in photovoltaic performance for photovoltaic devices with mm-scale active area [52]-[54], [59].

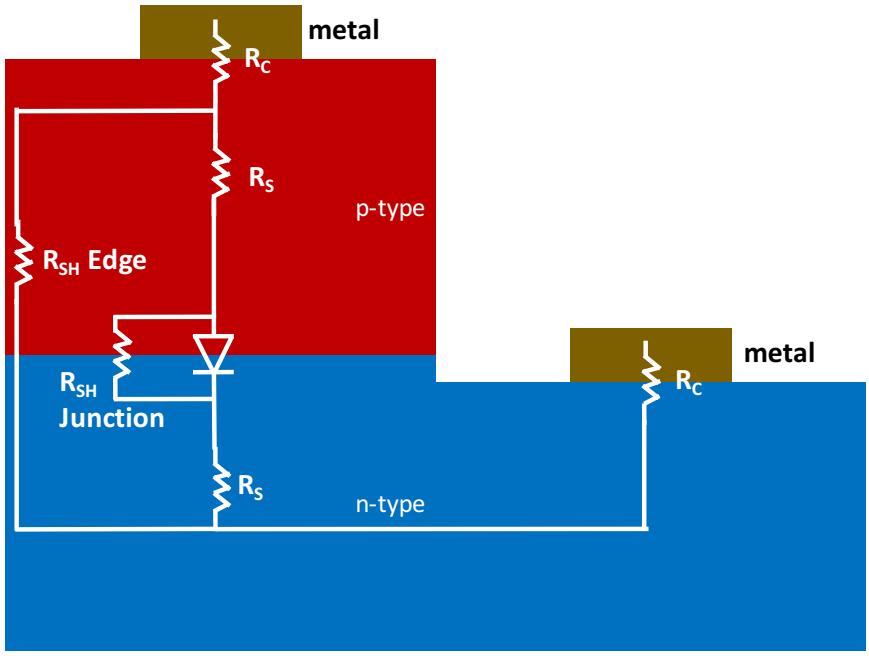

Figure 4.3. Parasitic resistances in p-n junction photovoltaic cells.

Figure 4.3 summarizes resistance losses which result from contact, series, and shunt resistance. Losses resulting from contact and series resistance is minimal for indoor photovoltaics since irradiance levels are low under indoor lighting conditions. Special attention needs to be devoted to studying shunt paths near the edges of the device. A low shunt resistance leads to a degradation in open-circuit voltage and fill-factor.

4.3 External Quantum Efficiency

The external quantum efficiency (EQE) of a photovoltaic cell provides information about the effectiveness of the cell in absorbing incoming photons and collecting the carriers generated. The measured EQE of the $Al_{0.2}Ga_{0.8}As$ and GaAs photovoltaic cell is shown in Figure 4.4. The spectral content of the white LED used for

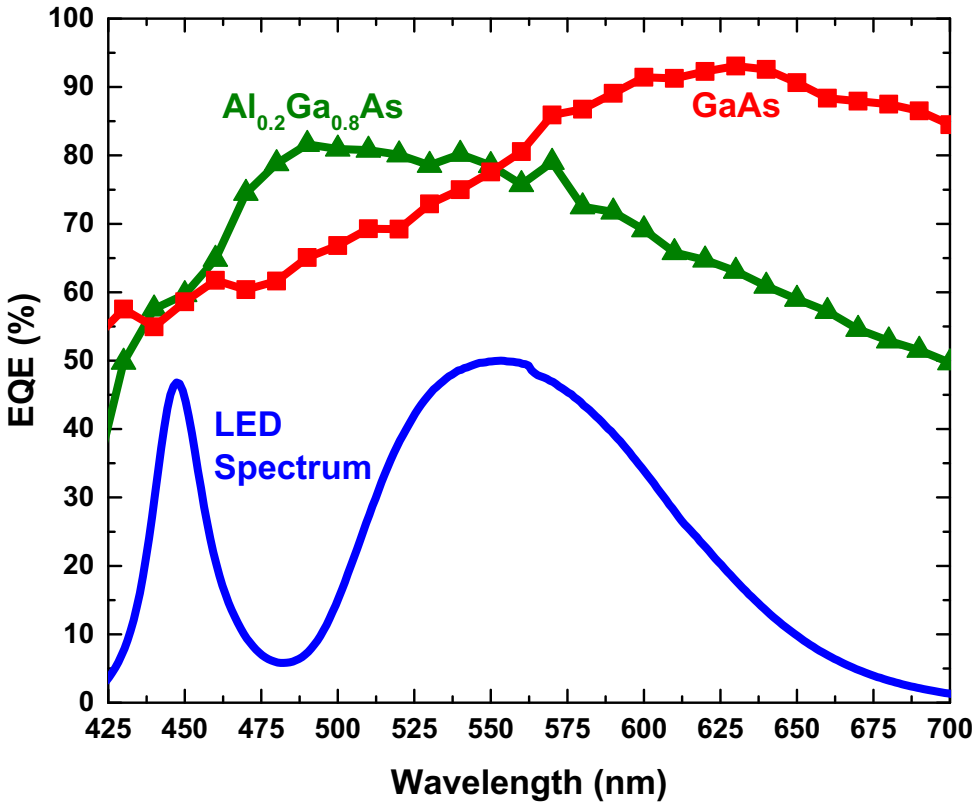

Figure 4.4. Measured external quantum efficiency of $Al_{0.2}Ga_{0.8}As$ and GaAs cells along with the spectral content of the white LED used for indoor measurements.

indoor measurements is also shown in order to highlight the wavelengths of interest for indoor photovoltaic devices. Since most indoor lighting sources have spectra contained within 425 nm to 700 nm, special focus must be placed on the EQE of photovoltaic devices within that wavelength range in order to have high photocurrent under indoor lighting sources. As was discussed in the previous chapter, high short-circuit current values are in agreement with EQE measurements shown in Figure 4.4. Absorption and collection is strong over the wavelengths of interest for both GaAs and $Al_{0.2}Ga_{0.8}As$ photovoltaic cells. Since indoor lighting spectra are contained in the visible portion of the electromagnetic spectrum, the problems associated with rear surface recombination and

reduced absorption at longer wavelengths do not manifest themselves in the performance of indoor photovoltaics. Both cells demonstrate a drop in EQE at short wavelengths due to front surface recombination. EQE at short wavelengths have an increased impact on performance for indoor photovoltaics compared with outdoor photovoltaics. Special attention must be placed on the design of anti-reflection coatings, emitter thickness and doping, and surface passivation. Optimization of these properties will result in indoor photovoltaic cells with short-circuit current close to theoretical maximum.

4.4 Dark Current

The sources of V_{OC} loss were investigated by measuring dark current and extremely dim photovoltaic response on GaAs photovoltaic cells of varying dimension. The perimeter/area (P/A) ratios of the cells used for these measurements range from 100 to 400 cm^{-1}. Dark current measurements under reverse and forward bias are shown in Figure 4.5. In order to extract diode parameters, a detailed analysis of diode behavior under forward bias is required. The dark current measurements under forward bias of GaAs cells of varying dimensions is shown in Figure 4.6 using a log scale for the vertical axis of current. There are three distinct regions in the plot. At low voltages the the current-voltage relationship is linear resulting in a non-linear curve on a semilog plot. At higher voltages the curve becomes linear in a semilog plot since the current becomes dominated by recombination/generation currents. Further increasing voltages results in series resistance dominating current. The forward bias curve can be fitted using the standard diode equation

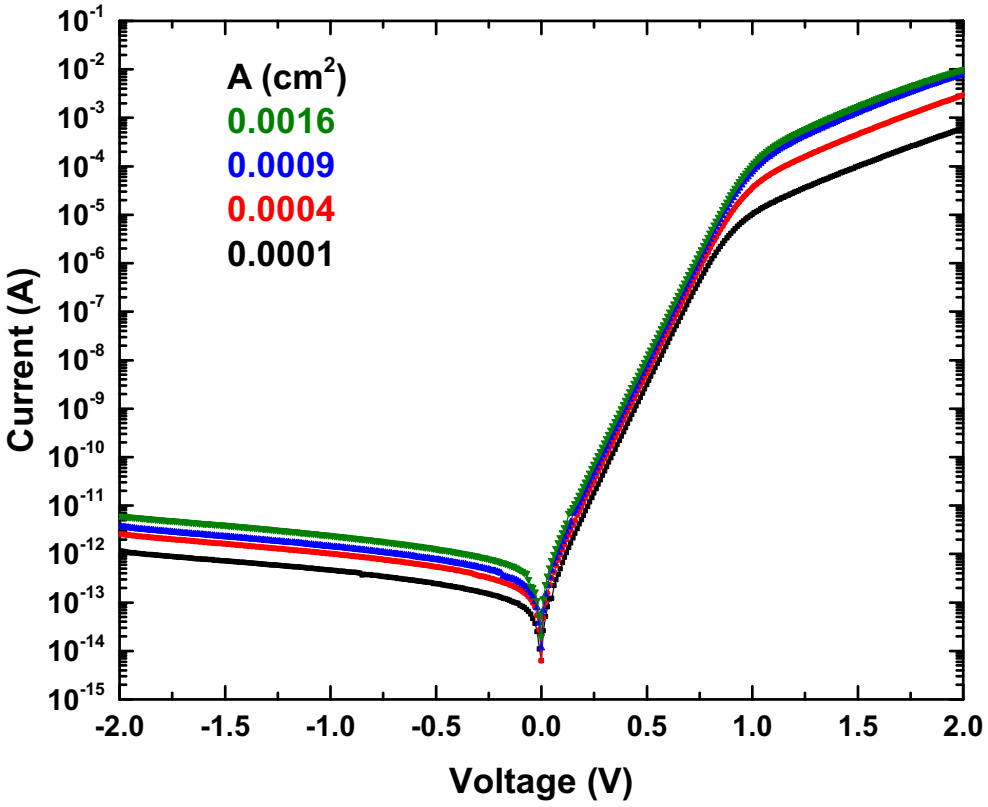

Figure 4.5. Dark current measurements of GaAs cells of varying dimensions from which diode parameters were extracted.

$$J = J_0 \left(\exp\left(\frac{qV}{nkT}\right) - 1 \right) \tag{4.1}$$

where J is the current, J_0 is the reverse saturation current, q is the electronic charge, V is the voltage, n is the diode ideality factor, k is Boltzmann's constant, and T is the temperature of the diode. The extracted parameters I_0 and n are summarized in Table 4.1 for the GaAs cells of varying dimensions. The reverse saturation current ranges from 35 pA/cm^2 to 217 pA/cm^2 with a strong P/A dependence. The diode ideality factor is close to n = 2 indicating a dominant recombination current.

More information can be extracted from the forward bias curve by fitting using an

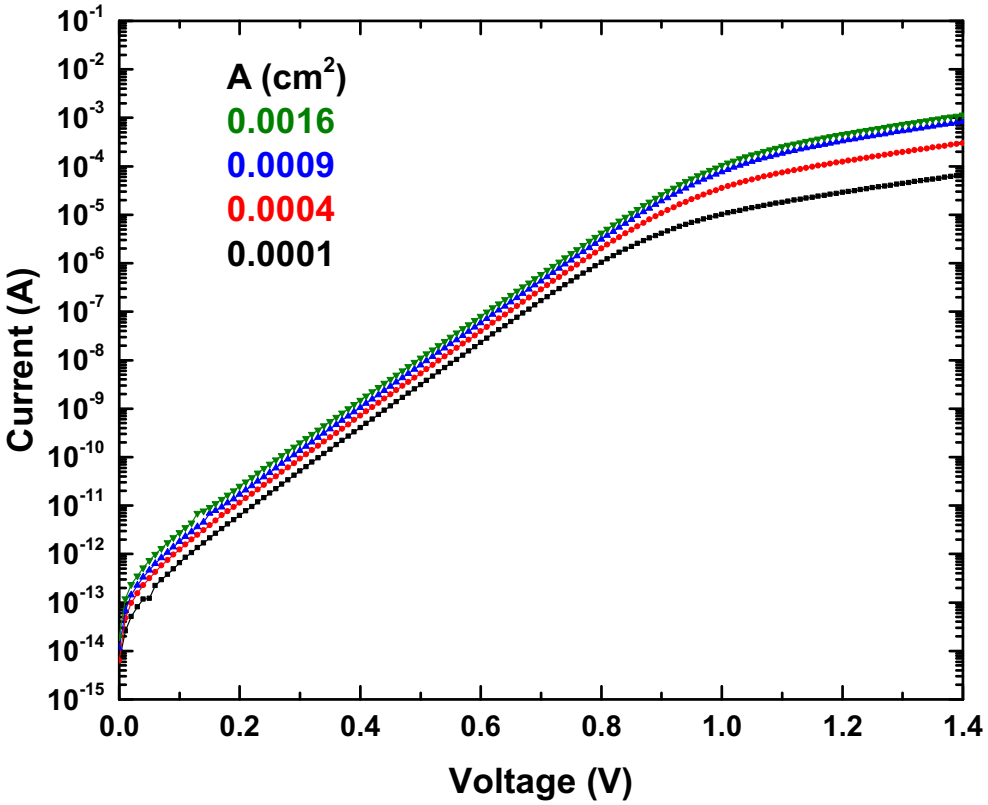

Figure 4.6. Dark current measurements under forward bias of GaAs cells of varying dimensions from which diode parameters were extracted.

expansion of Equation 4.1

$$J = J_{01}\left(\exp\left(\frac{qV}{kT}\right) - 1\right) + J_{02}\left(\exp\left(\frac{qV}{2kT}\right) - 1\right) \tag{4.2}$$

where J_{01} is from diffusion current and J_{02} is from recombination current. The extracted parameters J_{01} and J_{02} are summarized in Table 4.2 for the GaAs cells of varying dimensions.

P/A (cm^{-1})	P (cm)	A (cm^2)	J_0 (pA/cm^2)	n
100	0.16	0.0016	35	1.99
133	0.12	0.0009	43	1.95
200	0.08	0.0004	71	1.93
400	0.04	0.0001	217	1.94

Table 4.1. Extracted parameters using Equation 4.1 from forward bias measurements.

P/A (cm^{-1})	P (cm)	A (cm^2)	J_{01} (pA/cm^2)	J_{02} (pA/cm^2)
100	0.16	0.0016	$1.9x10^{-6}$	51
133	0.12	0.0009	$3.3x10^{-6}$	66
200	0.08	0.0004	$2.5x10^{-6}$	100
400	0.04	0.0001	$5x10^{-7}$	236

Table 4.2. Extracted parameters using Equation 4.2 from forward bias measurements.

The strong P/A dependence of J_{02} is shown in Figure 4.7 where the extracted parameter is plotted versus P/A for GaAs photovoltaic cells of varying dimensions. Following the analysis done in [59], the saturation current density J_{02} can be written as

$$J_{02} = J_{02B} + J'_{02P}\left(\frac{P}{A}\right) \tag{4.3}$$

where J_{02B} (pA/cm^2) is the bulk recombination current density, J'_{02P} (pA/cm) is the perimeter recombination coefficient, P (cm) is the perimeter of the device, and A (cm^2) is the area of the device. The perimeter recombination coefficient can be extracted from the slope of the linear fit from Figure 4.7. The extracted value of J'_{02P} from the slope is 0.626 pA/cm. This value is slightly larger than, but on the order of, the J'_{02P} reported for high efficiency GaAs solar cells [59]. The perimeter recombination coefficient can be written as

$$J'_{02P} = qn_iS_0L_s \tag{4.4}$$

where n_i is the intrinsic carrier concentration, S_0 is the surface recombination velocity, and L_s is an effective surface diffusion length. The product S_0L_s for these devices is 2.19 cm^2/s. High efficiency GaAs solar cells have S_0L_s less than 1 cm^2/s [59]. This result indicates the dominating effects of perimeter recombination currents in photovoltaic devices with mm-scale area.

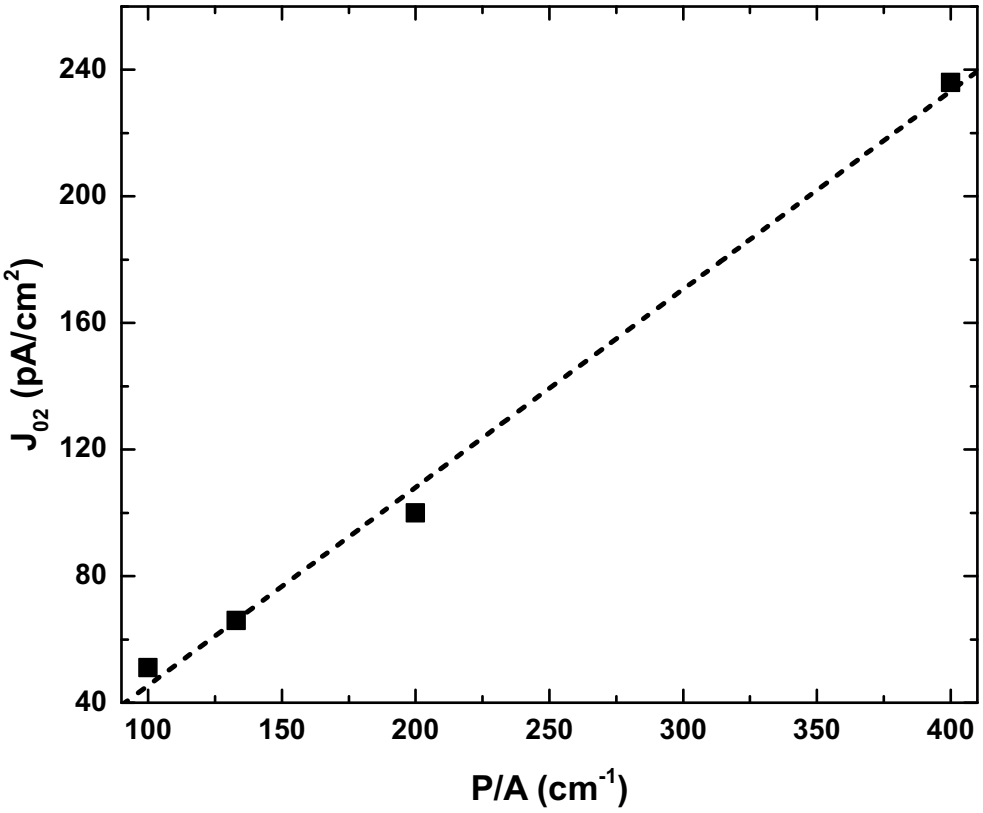

Figure 4.7. Extracted saturation current versus P/A for GaAs cells of varying dimensions.

4.5 Shunt Resistance

Real photovoltaic cells suffer from non-idealities including parasitic resistances and surface recombination currents. Parasitic resistances are split into two categories, series resistance and shunt resistance. Figure 4.8 provides an equivalent circuit model of a photovoltaic cell including series and shunt resistances. Series resistance arises from the resistance of current flow through the photovoltaic cell. Shunt resistance arises from current leakage through the cell. A small series resistance and a large shunt resistance is desired for efficient photovoltaic energy harvesting. When parasitic resistances are

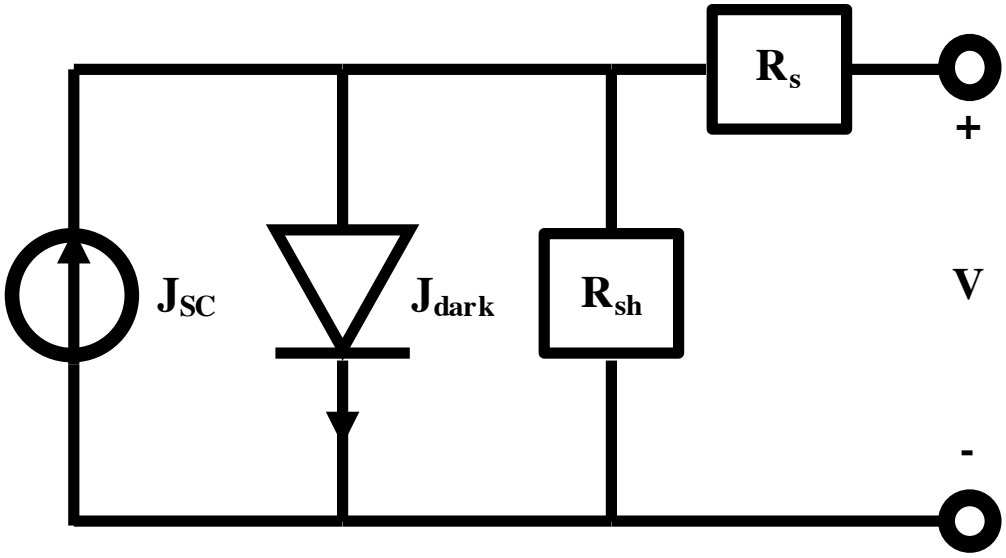

Figure 4.8. Equivalent circuit of a photovoltaic cell with parasitic resistances.

included, Equation 1.2 becomes

$$J = J_{sc} - J_0\left(\exp\left(\frac{q(V+JAR_s)}{kT}\right) - 1\right) - \frac{(V+JAR_s)}{R_{sh}} \tag{4.5}$$

where A is the area and R_s and R_{sh} are series and shunt resistance, respectively. Parasitic resistances have a large effect on fill factor and open circuit voltage.

In order to study the effects of shunt resistance under indoor lighting conditions, current-voltage measurements were made under extremely dim illumination. Measurements of extremely dim photovoltaic response results in a linear relationship between J_{SC} and V_{OC}. Shunt resistance values can be extracted from the slopes of the resulting curves. This technique was developed by Chan and Phang and has been used by others to directly measure the shunt resistance of a solar cell without prior knowledge of solar cell parameters [56]-[58]. The solar cell current-voltage relation can be expressed as

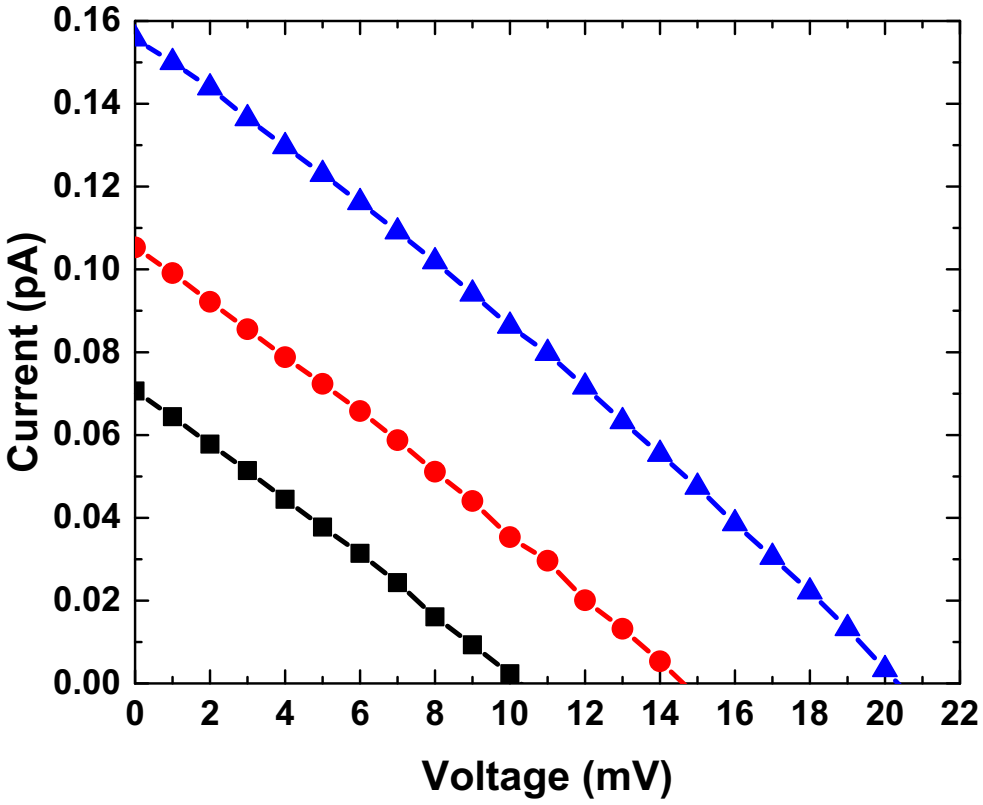

Figure 4.9. Measured current density versus voltage of a GaAs cell under varying levels of extremely dim light.

$$I_{SC}\left(\frac{R_s}{R_{sh}}+1\right)-\frac{V_{OC}}{R_{sh}}=I_s\left[\exp\left(\frac{V_{OC}}{nV_T}\right)-\exp\left(\frac{I_{SC}R_s}{nV_T}\right)\right] \tag{4.6}$$

where I_s is the saturation current, n is the junction ideality factor, V_T is equal to kT/q, V_{OC} is the open-circuit voltage, I_{SC} is the short-circuit current, R_s is the series resistance, and R_{sh} is the shunt resistance. Since R_s is much smaller than R_{sh} and $I_{SC}R_s/nV_T$ is close to unity under extremely dim illumination conditions, Equation 4.6 can be simplified to

$$I_{SC}-I_s\left[\exp\left(\frac{V_{OC}}{nV_T}\right)-1\right]=\frac{V_{OC}}{R_{sh}} \tag{4.7}$$

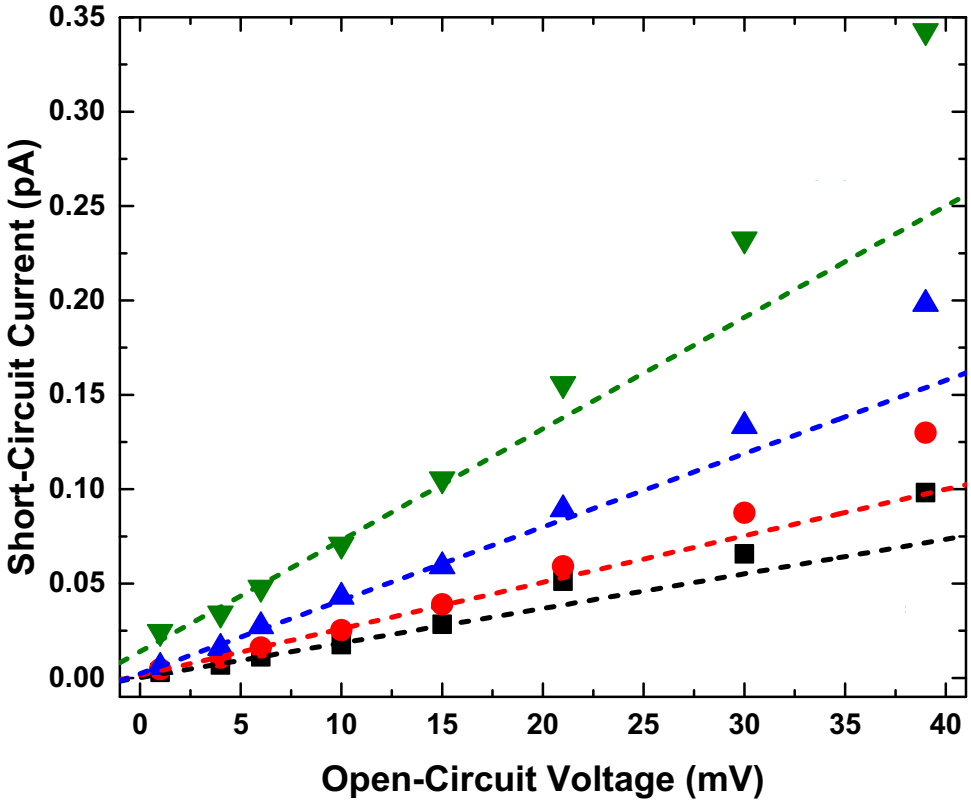

Figure 4.10. Measured short-circuit current versus open-circuit voltage of GaAs cells of varying dimensions under extremely dim conditions from which shunt resistance values were extracted.

Equation 4.7 can be further simplified by recognizing that the term $I_s[\exp(V_{OC}/nV_T)-1]$ can be neglected since V_{OC} is small under extremely dim illumination conditions. This assumption allows Equation 4.7 to be simplified to

$$I_{SC} = \frac{V_{OC}}{R_{sh}} \tag{4.8}$$

P/A (cm^{-1})	P (cm)	A (cm^2)	R_{SH} (MΩ-cm^2)	R_S (mΩ-cm^2)
100	0.16	0.0016	27	130
133	0.12	0.0009	23	90
200	0.08	0.0004	16	110
400	0.04	0.0001	5	150

Table 4.3. Extracted parameters from dark and extremely dim measurements.

resulting in a linear relationship between short-circuit current and open-circuit voltage allowing one to obtain the shunt resistance of a photovoltaic device directly from Equation 4.8. Figure 4.9 demonstrates the linear current-voltage relationship for a photovoltaic device under extremely dim lighting conditions. The short-circuit current and open-circuit voltage values extracted from Figure 4.9 and similar measurements can be plotted as shown in Figure 4.10. Plotting short-circuit current as a function of open-circuit voltage results in linear curves from which shunt resistance values can be extracted from the slope. The shunt resistance values extracted from Figure 4.10 is summarized in Table 4.3. Similar to the saturation current, the shunt resistance of the GaAs photovoltaic cells that were measured demonstrated a strong P/A dependence.

4.6 Discussion

The dark current of the GaAs photovoltaic cells of mm-scale are dominated by n=2 perimeter recombination currents. J_O has a strong P/A dependence ranging from 35 to 217 pA/cm^2. These dark current levels have a strong influence on V_{OC} at low illumination conditions (including typical indoor lighting illuminance). Shunt resistance also showed a strong P/A dependence ranging from 27 to 5 MΩ-cm^2.

In order to study the effects of these shunt resistance levels on V_{OC}, the photovoltaic response under indoor illumination conditions of a GaAs cell with P/A of 400 cm^{-1} and J_0 of 217 pA/cm^2 was simulated with infinite shunt resistance and 5 MΩ-cm^2 shunt resistance. The resulting simulation is shown in Figure 4.11. It is clear from the simulations that shunt resistance levels of MΩ-cm^2 are large enough to prevent shunt

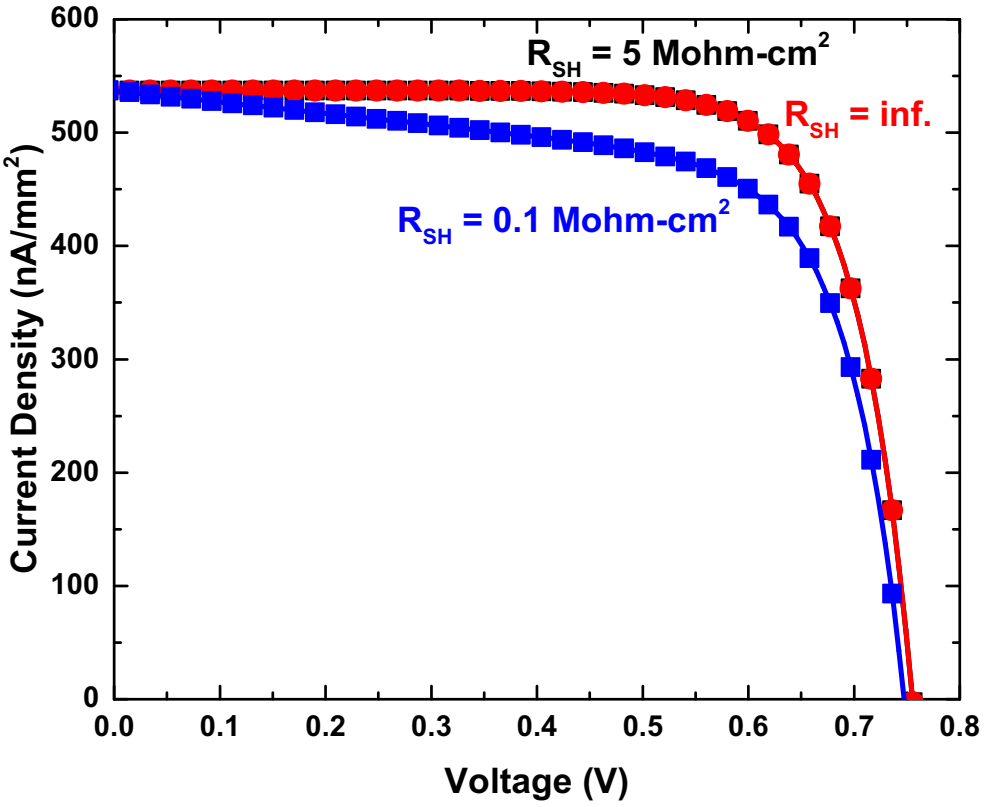

Figure 4.11. Calculated photovoltaic response for three GaAs cells, with infinite, 5 MΩ-cm^2, and 0.1 MΩ-cm^2 shunt resistance.

resistance leakage under indoor illumination conditions.

Dim lighting conditions (including indoor lighting conditions) amplify the effects of perimeter recombination currents since the photocurrent is of the order of the n=2 dark current. The power conversion efficiency versus area of photovoltaic devices of various areas with parameters from Table 4.2 and 4.3 was simulated assuming indoor and AM 1.5 illumination. The resulting simulation is shown in Figure 4.12. Power conversion efficiencies greater than 30% can be achieved under indoor lighting conditions for devices with areas orders of magnitude larger than the ones used in this study. Power conversion efficiency saturates under AM 1.5 at lower areas.

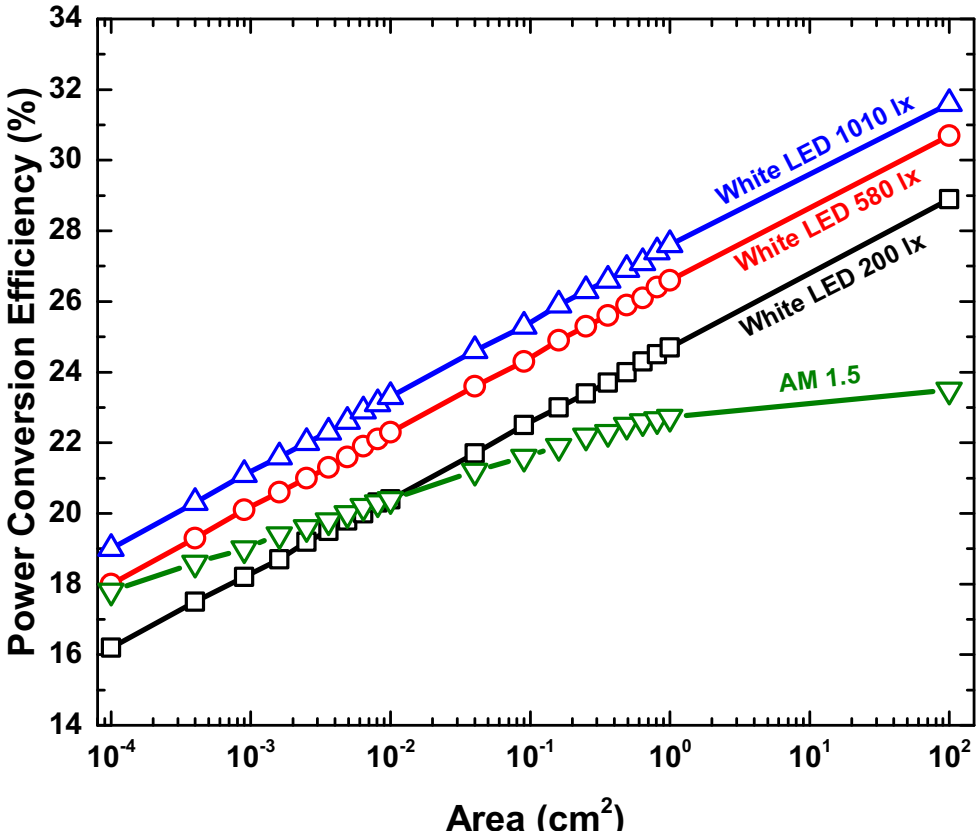

Figure 4.12. Calculated power conversion efficiency for GaAs cells of various areas with parameters from Table 4.2 and Table 4.3 under indoor illumination and AM 1.5.

Improvements in side-wall passivation need to be investigated in order to reduce perimeter recombination currents and improve indoor efficiency of GaAs-based photovoltaics. Chemical studies have shown improvements in the passivation of GaAs surface recombination using sulfides and thiols [60]-[63]. These chemical treatments help passivate dangling bonds on the surfaces of the devices resulting in improvements in open-circuit voltage and overall efficiency.

4.7 Summary

Record indoor power conversion efficiency GaAs and $Al_{0.2}Ga_{0.8}As$ photovoltaic cells demonstrate high EQE over the wavelength range of interest for indoor photovoltaics. Dark perimeter recombination currents have been identified as the major source of V_{OC} and efficiency degradation. Shunt resistance values have been extracted from extremely dim current-voltage measurements and have been shown to be large for indoor lighting conditions. The extracted ideality factor of n=2 is a result of surface recombination currents. Improvements in chemical passivation of photovoltaic devices is necessary for increasing open-circuit voltage and overall power conversion efficiency.

Chapter V

Summary and Future Work

5.1 Summary of Thesis Work

This thesis provides an in-depth study of spectrum-dependent energy harvesting technologies. These technologies require increased attention as mm-scale electronics become ubiquitous in our society. Traditional solar cell devices are not optimized for photovoltaic energy harvesting because they are designed for high-intensity solar illumination. New materials and device designs are required for high-efficiency photovoltaic energy harvesting.

Chapter 1 provides derivations for fundamental figures of merit such as short-circuit current, open-circuit voltage, fill-factor, and power conversion efficiency. An understanding of these figures of merit are necessary for analyzing photovoltaic device performance. The derivation of solar irradiance and indoor illuminance is also provided. The differences between the two are discussed in addition to the differences in spectra of outdoor and indoor illumination sources. A derivation of detailed balance theory for a p-n junction solar cell is provided. The solution is used throughout the dissertation in order to

calculate photovoltaic performance under different lighting conditions.

Chapter 2 focuses on the ZnTe solar cells and the various heterojunction devices studied in order to realize the ZnTeO intermediate band solar cell. Previous results of the p-ZnTe/n-GaAs heterojunction solar cell is presented in order to motivate the importance of the quality of the heterojunction formed in the photovoltaic device. Evidence of intermediate band behavior is present in the photovoltaic response, photoluminesense, and external quantum efficiency. The n-ZnSe/p-ZnTe/p-GaSb heterojunction solar cell is introduced in order to study the effects of improved lattice-matching to the substrate and window layer. Improved photovoltaic response is observed due to a reduction in dark current and increased external quantum efficiency at high wavelengths. In order to study the effects of heterojunction grading, the p-ZnTe/n-ZnTeSe/n-GaAs heterojunction solar cell is introduced. Improvements in photovoltaic response is observed due to a reduction in threading dislocations at the junction. Despite the improvements in performance, the open-circuit voltage is still low compared with theoretical values. Concentration measurements at low temperature were performed revealing limitations on open-circuit voltage due to the heterojunction band lineup instead of the bandgap of ZnTe.

Chapter 3 introduces the reader to energy harvesting technologies such as photovoltaic, thermoelectric, and piezoelectric among others. A summary of previous work done on indoor photovoltaics is provided. Theoretical calculations were performed revealing a maximum indoor power conversion efficiency of 60% for an indoor photovoltaic cell with a bandgap of 1.9 eV. GaAs and $Al_{0.2}Ga_{0.8}As$ photovoltaic devices were fabricated with device design optimized for indoor illumination. A record indoor

power conversion efficiency of 21.1% was realized with the $Al_{0.2}Ga_{0.8}As$ photovoltaic cell. The open-circuit voltage and fill-factor of the fabricated photovoltaic cells was compared with commercial a-Si and Si solar cells. Finally, light harvesting efficiency was introduced as a new figure of merit for indoor photovoltaic devices.

In Chapter 4, non-idealities of photovoltaic devices are described. In particular, series resistance, shunt resistance, and ideality factor. The measurement techniques and analysis used for investigating the sources of loss in indoor photovoltaic devices under dim lighting conditions are described. The external quantum efficiency revealed strong absorption and collection for the GaAs and $Al_{0.2}Ga_{0.8}As$ photovoltaic devices throughout the wavelength range of interest for indoor photovoltaics. Dark current and shunt resistance measurements demonstrate a strong perimeter/area dependence, emphasizing the need for improved sidewall passivation technology.

5.2 InGaP Indoor Photovoltaics

$In_{0.5}Ga_{0.5}P$ is a semiconductor with a bandgap of 1.9 eV making it the ideal candidate for high efficiency indoor photovoltaics. Preliminary work has been done in order to realize the potential of $In_{0.5}Ga_{0.5}P$ indoor photovoltaics. Various measurements were done on an $In_{0.5}Ga_{0.5}P$ solar cell. The photovoltaic response of the $In_{0.5}Ga_{0.5}P$ solar cell is shown in Figure 5.1 along with the photovoltaic response of the indoor photovoltaic cells used in chapters 3 and 4. The $In_{0.5}Ga_{0.5}P$ solar cell has a open-circuit voltage of 0.9 V. The short-circuit current of the $In_{0.5}Ga_{0.5}P$ solar cell is smaller than the

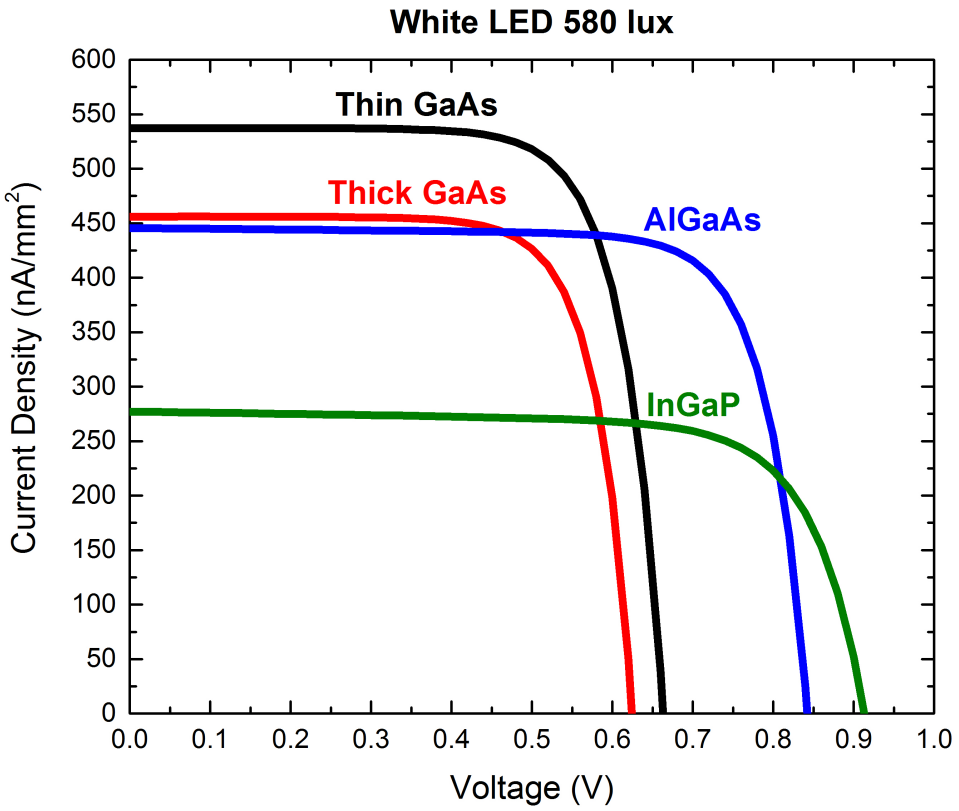

Figure 5.1. Measured photovoltaic response for GaAs, AlGaAs, and InGaP photovoltaic devices under white LED illumination.

short-circuit current of the GaAs and AlGaAs photovoltaic cells. This is due to un-optimized photovoltaic design for indoor illumination. In addition, the $In_{0.5}Ga_{0.5}P$ solar cell did not have an anti-reflection coating optimized for indoor illumination. The power density versus voltage is shown in Figure 5.2. The $In_{0.5}Ga_{0.5}P$ solar cell had a maximum power density of 186 nW/mm^2. Figure 5.3 demonstrates the maximum power density versus illuminance for the $In_{0.5}Ga_{0.5}P$ solar cell. Maximum power densities greater than 100 nW/mm^2 can be achieved at 300 lux for the $In_{0.5}Ga_{0.5}P$ photovoltaic cell. These results indicate that, with proper optimization, $In_{0.5}Ga_{0.5}P$ can be the ideal semiconductor material for indoor photovoltaics. Device thickness, emitter and base doping, and anti-

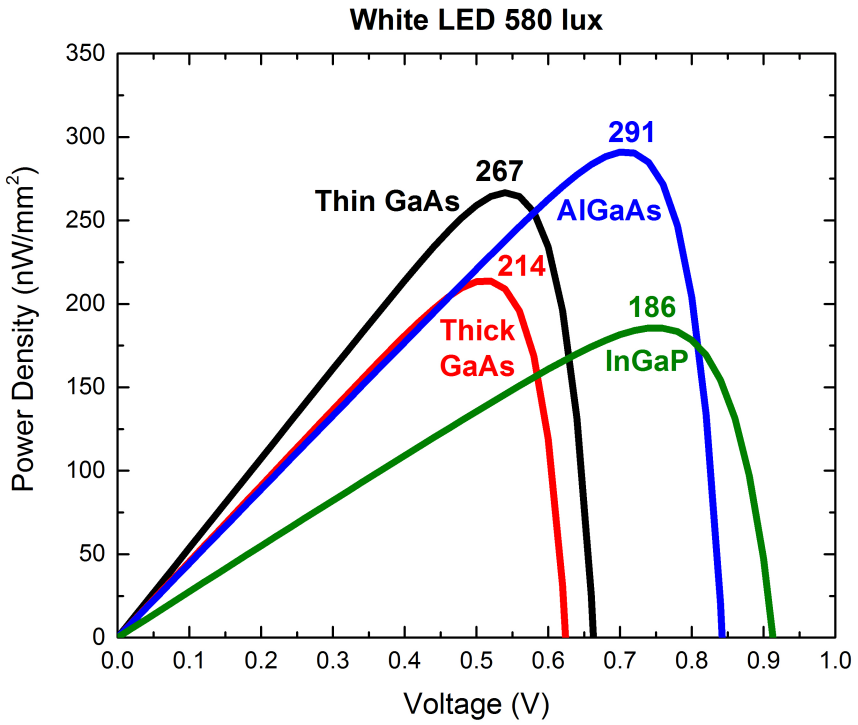

Figure 5.2. Measured power density versus voltage for GaAs, AlGaAs, and InGaP photovoltaic devices under white LED illumination.

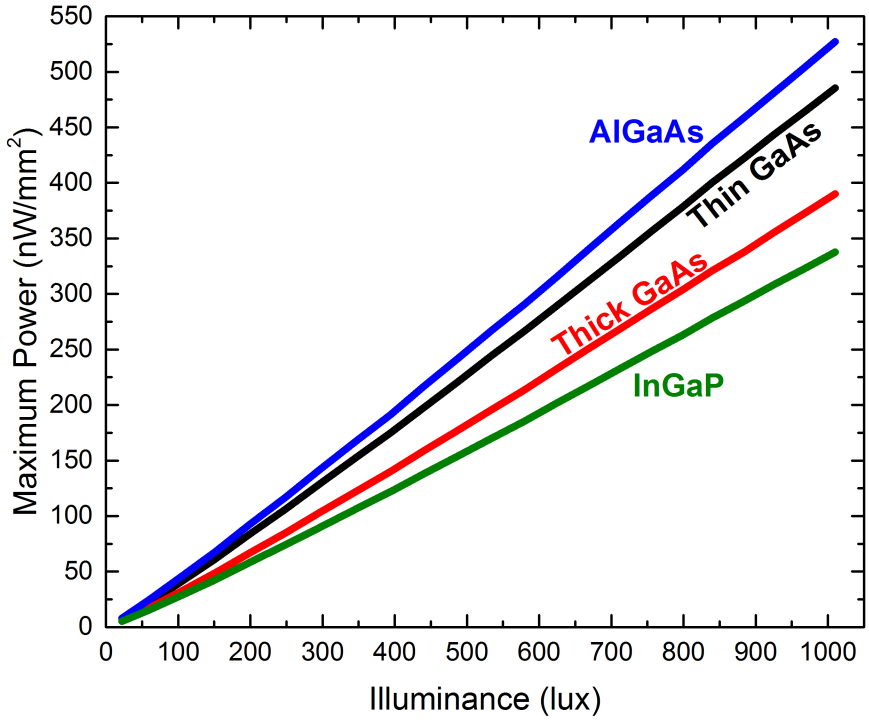

Figure 5.3. Measured maximum power density versus illuminance for GaAs, AlGaAs, and InGaP photovoltaic devices under white LED illumination.

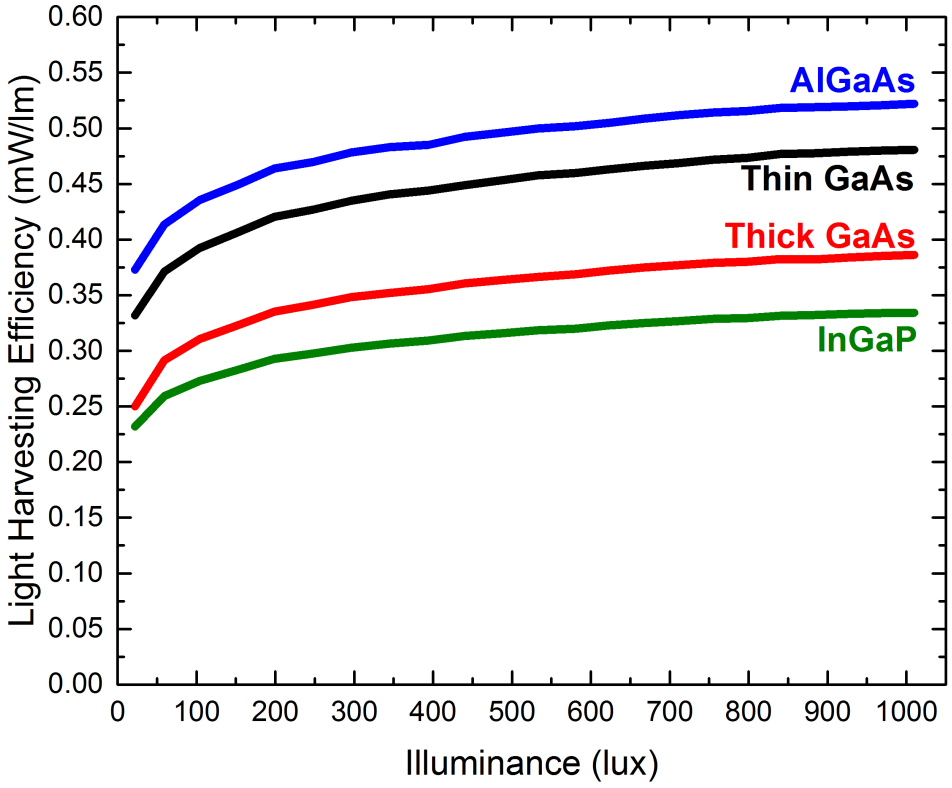

Figure 5.4. Measured light harvesting efficiency versus illuminance for GaAs, AlGaAs, and InGaP photovoltaic devices under white LED illumination.

reflection coating need to be designed for indoor lighting conditions. The $In_{0.5}Ga_{0.5}P$ solar cell also demonstrated strong light harvesting efficiency at dim lighting conditions as shown in Figure 5.4. Maintaining light harvesting efficiency at low lighting conditions is crucial for the successful implementation of light harvesting for mm-scale electronics.

5.3 Modular Energy Harvesting

Energy harvesting using photovoltaic devices requires up-conversion of the output voltage of the photovoltaic cell in order to charge the battery on the mm-scale sensor. The up-conversion process is not efficient and, therefore, requires more power

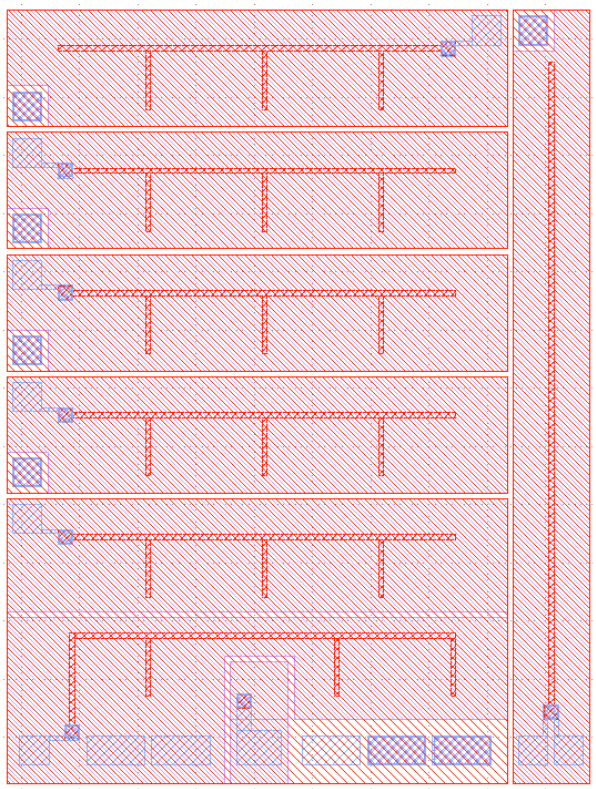

Figure 5.5. Small modular energy harvesting design with seven photovoltaic cells with equal active area.

collection from the photovoltaic device in order to make up for the efficiency loss. A modular energy harvesting design is proposed in order to eliminate the need for a voltage up-converter. A small modular photovoltaic design is shown in Figure 5.5. The design allows for up to seven photovoltaic cells to be connected in series. The configuration is can be changed depending on the light intensity. Photovoltaic cells have a larger operating voltage at higher light intensity. The number of photovoltaic cells that need to be stacked in order to match up with the battery charging voltage can, therefore, be different. Two designs are proposed with total active area of approximately 1 mm^2 and 10 mm^2. The 1 mm^2 design is shown in Figure 5.5 while the 10 mm^2 design is shown in

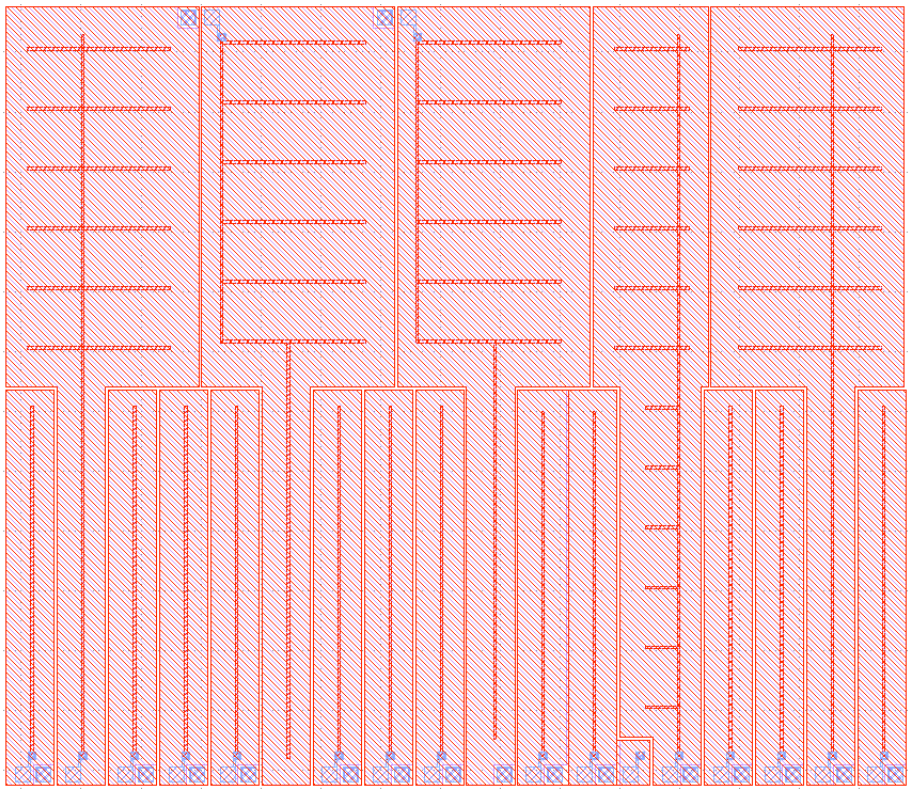

Figure 5.6. Large modular energy harvesting design with seven photovoltaic cells with equal active area.

Figure 5.6. The large design allows for increased flexibility in photovoltaic stacking configuration.

5.4 Subcutaneous Energy Harvesting

Recently, advances in material science have allowed for increased integration and functionality of electronic devices with human skin [64]-[67]. Figure 5.6 demonstrates conformal electronic films attached to human skin. These electronic skins allow for precise measurements of temperature at the epidermis. The limitations of these electronic films is their inability to provide relevant medical information of the area underneath the

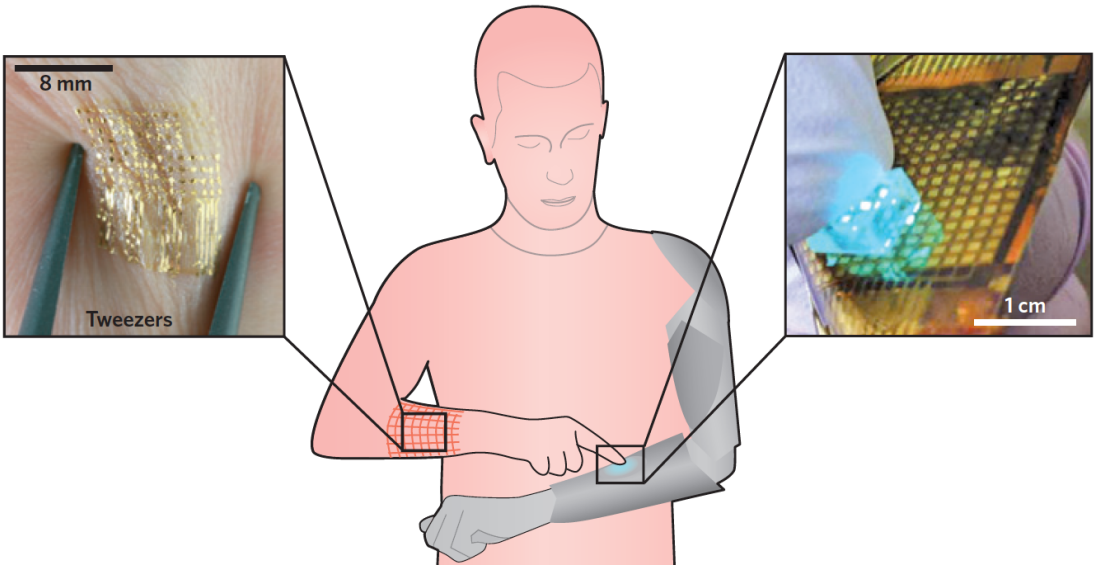

Figure 5.7. Demonstrations of electronic films attached to skin allowing for precise measurement of temperature (adopted from [64]).

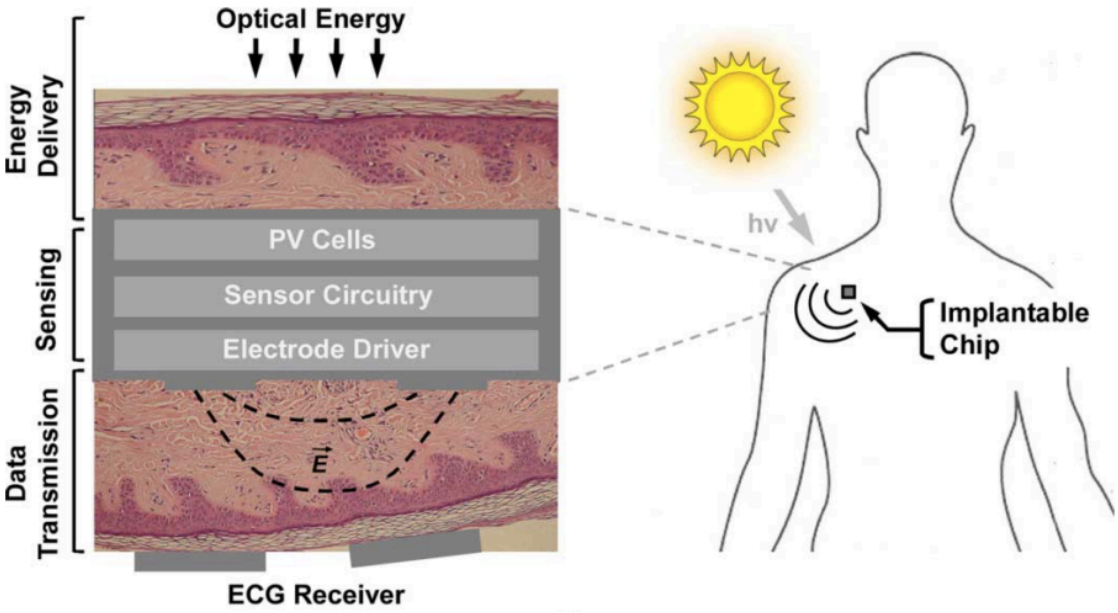

Figure 5.8. Example of subcutaneous sensor that is powered by a photovoltaic device after implantation (adopted from [68]).

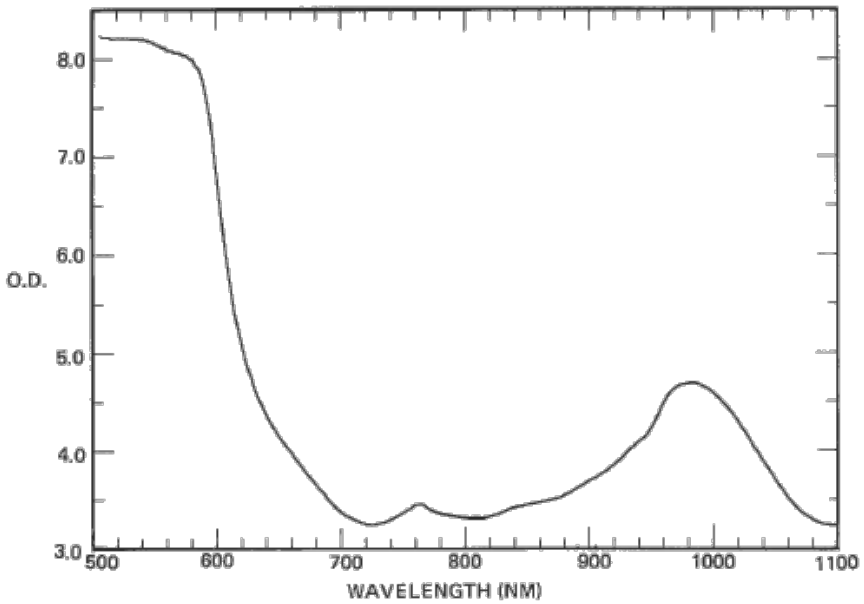

Figure 5.9. Absorption spectrum of a human hand (adopted from [69]).

skin. Subcutaneous sensors have been proposed as shown in Figure 5.8 [68]. These sensors would be powered by energy harvesting technologies such as photovoltaic devices.

In order to have adequate power collection from subcutaneous photovoltaic energy harvesting the photovoltaic cell must be design for optimal absorption of light that penetrates through the human skin. Figure 5.9 shows the absorption spectrum of a human hand. The skin allows a good portion of infrared light to penetrate the skin. The wavelength range that is not completely filtered is 700-900 nm. In order to absorb infrared light in that wavelength range the photovoltaic device must be designed with a thicker base in comparison to the base thickness of indoor photovoltaic devices.

Preliminary studies have been done on subcutaneous energy harvesting by fabricating a GaAs photovoltaic device with an adequate base thickness for absorption of

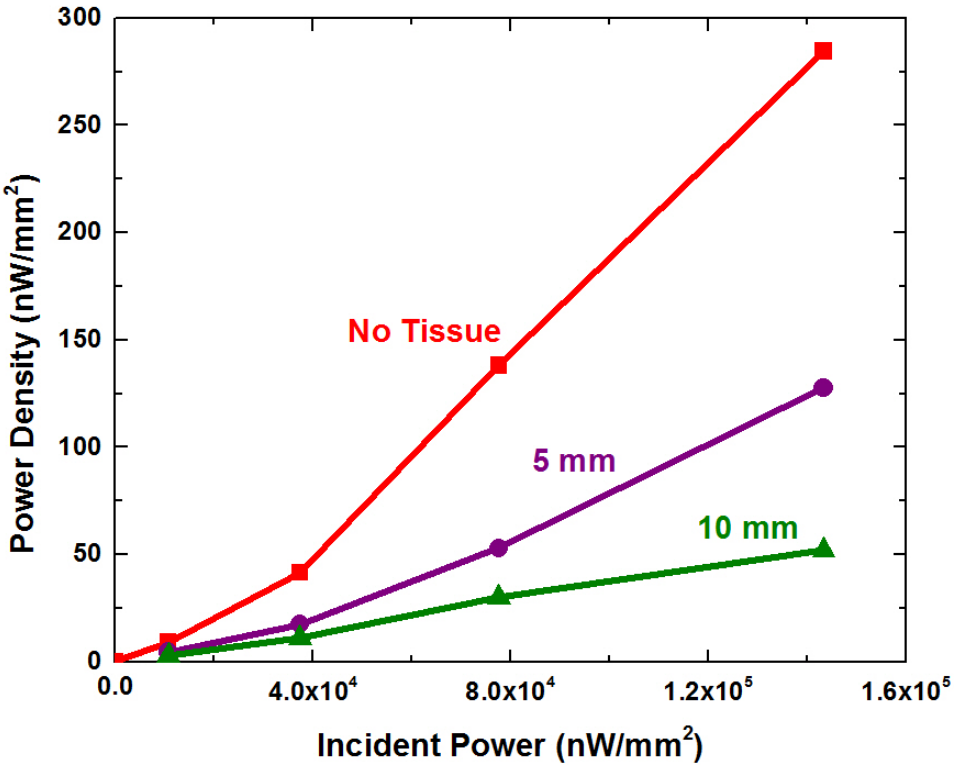

Figure 5.10. Measured power density versus incident power for a GaAs photovoltaic device under infrared illumination and pork tissue of various thickness.

infrared light in the 700-900 nm range. The performance under the skin was simulated by covering the GaAs photovoltaic device with pork tissue of various thicknesses. The measurements are shown in Figure 5.10. An infrared power source was used to observe the dependence on incident power. Power densities greater than 100 nW/mm^2 were achieved for an incident power density of 60 μW/mm^2. Under 5 mm of pork tissue the photovoltaic cell required incident power density greater than 120 μW/mm^2 in order to provide a power density of 100 nW/mm^2. Doubling the pork tissue thickness further reduced the power generated from the photovoltaic cell. These results indicate that the implantation of mm-scale sensors with GaAs photovoltaic harvesting should be within 10

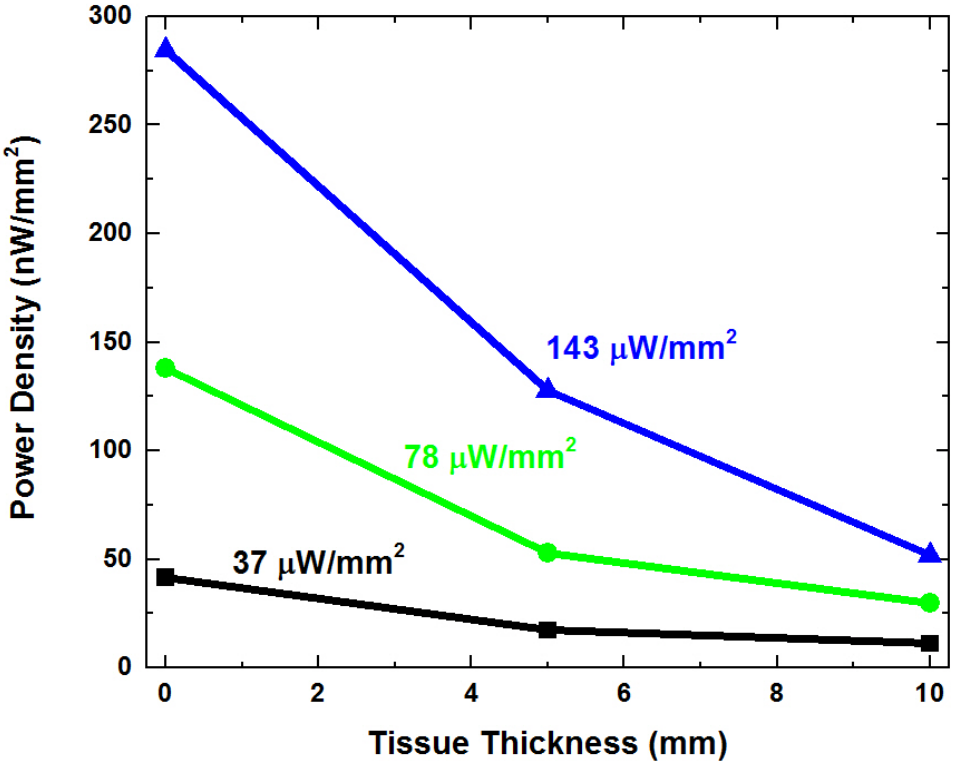

Figure 5.11. Measured power density versus tissue thickness for a GaAs photovoltaic device under infrared illumination with various incident power.

mm of the skin. This is emphasized in Figure 5.11 showing measured power density versus tissue thickness. Sufficient power can be harvested from GaAs photovoltaic cells to power mm-scale sensors.

5.5 Summary of Future Work

Three future works have been proposed to continue the work done in the thesis. An InGaP photovoltaic device has been proposed to improve the efficiency of indoor photovoltaics due to the larger bandgap of the semiconductor material. Preliminary measurements of an InGaP solar cell demonstrate a higher operating voltage compared

with AlGaAs but a lower power conversion efficiency. Improvements in device design and fabrication can increase efficiency. In addition, a modular photovoltaic harvesting design has been proposed that utilizes series configurations of photovoltaic cells to match with the charging voltage of a battery. This modular design allows for bypassing the DC-DC converter, improving the overall efficiency of the system. Finally, a subcutaneous photovoltaic device has been proposed to be used with implantable mm-scale electronics. Infrared light in the 700-900 nm range can be harvested through skin and with sufficient energy to power mm-scale sensors.

BIBLIOGRAPHY

BIBLIOGRAPHY

[1] M.A. Green, *Progress in Photovoltaics: Research and Applications*, **9**, 123-135 (2000).

[2] G. Bell, *Communications of the ACM*, **51**, 1, 86-94 (2008).

[3] W. Shockley and H.J. Queisser, *J. Appl. Phys.* **32**, 510-519 (1961).

[4] P.G. Linares, A. Marti, E. Antolin, I. Ramiro, E. Lopez, E. Hernandez, D.F. Marron, I. Artacho, I. Tobias, P. Gerard, C. Chaix, R.P. Campion, C.T. Foxon, C.R. Stanley, S.I. Molina, and A. Luque, *Sol. Energy Mater. Sol. Cells,* **108**, 175-179 (2012).

[5] J.D. Dow, R. Hong, S. Klemm, S.Y. Ren, M.H. Tsai, O.F. Sankey, and R.V. Kasowski, *Phys. Rev. B,* **43**, 5, 4396-4407 (1991).

[6] W. Wang, A. Lin, and J.D. Phillips, *J. Electron. Mater.,* **37**, 8, 1044-1048 (2008).

[7] W. Wang, A. Lin, and J.D. Phillips, *Appl. Phys. Lett.*, **95**, 011103-1-011103-3 (2009).

[8] W. Wang, J.D. Phillips, S.J. Kim, and X. Pan, *J. Electron. Mater.,* **40**, 8, 1674-1078 (2011).

[9] T. Tanaka, K.M. Yu, A.X. Levander, O.D. Dubon, L.A. Reichertz, N. Lopez, M. Nishio, and W. Walukiewicz, *Jpn. J. Appl. Phys.,* **50**, 0823041-1-082304-3 (2011).

[10] T. Tanaka, M. Miyabara, Y. Nagao, K. Saito, Q. Guo, M. Nishio, K.M. Yu, and W. Walukiewicz, *Appl. Phys. Lett.,* **102**, 052111-1-05211104 (2013).

[11] T. Tanaka, M. Miyabara, K. Saito, Q. Guo, M. Nishio, K.M. Yu, and W. Walukiewicz, *Mater. Sci. Forum.,* **750**, 80-83 (2013).

[12] J. Phillips, A. Teran, C. Chen, E. Antolin, I. Ramiro, E. Lopez, E. Hernandez, I. Artacho, C. Tablero, A. Marti, and A. Luque, *Proc. 39th IEEE Photovoltaic Spec. Conf.,* 1640-1643 (2013).

[13] T. Tanaka, M. Miyabara, Y. Nagao, K. Saito, Q. Guo, M. Nishio, K.M. Yu, and W. Walukiewicz, *IEEE J. Photovoltaics*, **4**, 1, 196-201 (2014).

[14] M. Yamaguchi, A. Yamamoto, and T. Itoh, *J. Appl. Phys.*, **59**, 5, 1751-1753 (1986).

[15] W. Wang, A.S. Lin, J.D. Phillips, and W.K. Metzger, *Appl. Phys. Lett.,* **95**, 261107-1-261107-3 (2009).

[16] T. Tanaka, S. Kusaba, T. Mochinaga, K. Saito, Q. Guo, M. Nishio, K.M. Yu, and W. Walukiewicz, *Appl. Phys. Lett.*, **100**, 011905-1-011905-3 (2012).

[17] E. Antolin, C. Chen, I. Ramiro, J. Foley, E. Lopez, I. Artacho, J. Hwang, A. Teran, E. Hernandez, C. Tablero, A. Marti, J.D. Phillips, and A. Luque, *IEEE J. Photovoltaics*, **4**, 4, 1091-1094 (2014).

[18] E.A. Fitzgerald, Y.H. Xie, M.L. Green, D. Brasen, A.R. Kortan, J. Michel, Y.J. Mii, and B.E. Weir, *Appl. Phys. Lett.*, **59**, 7, 811- 813 (1991).

[19] J. Singh, *Electronic and Optoelectronic Properties of Semiconductor Structures*. Cambridge, U.K.: Cambridge University Press, 2003.

[20] R. Passler, E. Griebl, H. Riepl, G. Lautner, S. Bauer, H. Preis, W. Gebhardt, B. Buda, D.J. As, D. Schikora, K. Lischka, K. Papagelis, and S. Ves, *J. Appl. Phys.,* **86**, 8, 4403-4411 (1999).

[21] S. Kasap and P. Capper, *Springer Handbook of Electronic and Photonic Materials.* New York, NY, USA: Springer, 2007.

[22] S.J. Fonash, *Solar Cell Device Physics,* Burlington, MA, USA: Elsevier, 2010.

[23] S. Roundy , P.K. Wright , and J.M. Rabaey, *Energy Scavenging for Wireless Sensor Networks,* 2004.

[24] Y. Lee, S. Bang, I. Lee, Y. Kim, G. Kim, M.H. Ghaed, P. Pannuto, P. Dutta, D. Sylvester, and D. Blaauw, *IEEE J. Solid-State Circuits*, **48**, 1, 229-243 (2013).

[25] M. Fojtik, D. Kim, G. Chen, Y. Lin, D. Fick, J. Park, M. Seok, M. Chen, Z. Foo, D. Blaauw, and D. Sylvester, *IEEE J. Solid-State Circuits*, **48**, 3, 801-813 (2013).

[26] W. Jung, S. Oh, S. Bang, Y. Lee, Z. Foo, G. Kim, Y. Zhang, D. Sylvester, and D. Blaauw, *IEEE J. Solid-State Circuits*, **49**, 12, 2800-2811 (2014).

[27] S. Hanson, M. Seok, Y. Lin, Z. Foo, D. Kim, Y. Lee, N. Liu, D. Sylvester, and D. Blaauw, *IEEE J. Solid-State Circuits*, **44**, 4, 1145-1155 (2009).

[28] J.F. Randall and J. Jacot, *World Renew. Energy Congr. VII Expo*, 2002.

[29] J.F. Randall and J. Jacot, *Renew. Energy*, **28**, 12, 1851-1864 (2003).

[30] J.F. Randall, *Designing Indoor Solar Products: Photovoltaic Technologies for AES*. Chichester, U. K.: Wiley, 2005.

[31] N.H. Reich, W.G.J.H.M. van Sark, E.A. Alsema, S.Y. Kan, S. Silvester, A.S.H. van der Heide, R.W. Lof, and R.E.I. Schropp, *Proc. 20th Eur. Photovolt. Solar Energy Conf. Exhibit.,* 6-10 (2005).

[32] G.E. Bunea, K.E. Wilson, Y. Meydbray, M.P. Campbell, and D.M. De Ceuster, *Proc. IEEE 4th World Conf. Photovolt. Energy*, 1312-1314 (2006).

[33] A. Nasiri, S.A. Zabalawi, and G. Mandic, *IEEE Trans. Ind. Electron.,* **56**, 11, 4502-4509 (2009).

[34] K. Ruhle, S.W. Glunz, and M. Kasemann, *Proc. 38th IEEE Photovolt. Specialists Conf.*, 2588-2591 (2012).

[35] K. Ruhle, M. Freunek, L.M. Reindl, and M. Kasemann, *Proc. 9th Int. Multi-Conf. Syst., Signals, Devices*, 1-5 (2012).

[36] K. Ruhle, M. Rauer, M. Rudiger, J. Giesecke, T. Niewelt, C. Schmiga, S.W. Glunz, and M. Kasemann, *Proc. 2nd Int. Conf. Crystal. Silicon Photovolt.*, **27**, 406-411 (2012).

[37] S. Beeby and N. White, *Energy Harvesting for Autonomous Systems.* Norwood, MA, USA: Artech House, 2010.

[38] M. Freunek, M. Freunek, and L.M. Reindl, *IEEE J. Photovolt.*, **3**, 1, 59-64 (2013).

[39] M. Kasemann, K. Ruhle, K.M. Gad, and S.W. Glunz, *Proc. SPIE, Smart Sens., Actuators, MEMS VI*, **8763**, 87631T (2013).

[40] K. Ruhle and M. Kasemann, *Proc. 39th IEEE Photovolt. Specialists Conf.*, 2651-2654 (2013).

[41] M. Freunek, *Solar Cell Nanotechnology*. Beverly, MA, USA: Scrivener Publishing, 2014, 203-222.

[42] W.S. Wang, T. O'Donnell, L. Ribetto, B. O'Flynn, M. Hayes, and C. O'Mathuna, *Proc. 1st Int. Conf. Wireless Commun., Veh. Technol., Inf. Theory, Aerosp. Electron. Syst. Technol.*, 36-41 (2009).

[43] Y.K. Tan and S.K. Panda, *IEEE Trans. Ind. Electron.*, **58**, 9, 4424-4435 (2011).

[44] I. Mathews, G. Kelly, P.J. King, and R. Frizzell, *Proc. 40th IEEE Photovolt. Specialists Conf.*, 510-513 (2014).

[45] A. Sacco, L. Rolle, L. Scaltrito, E. Tresso, and C.F. Pirri, *Appl. Energy*, **102**, 1295-1302 (2013).

[46] Y. Ohno, *Proc. SPIE, 4th Int. Conf. Solid State Lighting*, **5530**, 88-98 (2004).

[47] Y. Ohno, *Opt. Eng.*, **44**, 11, 111302-1-111302-9 (2005).

[48] W. Davis and Y. Ohno, *Proc. SPIE, 5th Int. Conf. Solid State Lighting,* **5941**, 59411G (2005).

[49] J. Hwang, A.J. Martin, K. Lee, S. Forrest, J. Millunchick, and J. Phillips, *Proc. IEEE 39th Photovolt. Specialist Conf.,* 3191-3194 (2013).

[50] (2015). IXYS IXOLAR SolarBIT KXOB22-12x1. [Online].

[51] (2015). CYMBET CBC-PV-02. [Online].

[52] P.D. DeMoulin, S.P. Tobin, M.S. Lundstrom, M.S. Carpenter, and M.R. Melloch, *IEEE Electron Device Lett.*, **9**, 8, 368-370 (1988).

[53] A. Belghachi and S. Khelifi, *Solar Energy Mater. Solar Cells*, **90**, 1, 1-14 (2006).

[54] P. Espinet-Gonzalez, I. Rey-Stolle, M. Ochoa, C. Algora, I. Garcia, and E. Barrigon, *Prog. Photovolt., Res. Appl.,* 1-9 (2014).

[55] D.K. Schroder, *Semiconductor Material and Device Characterization*. Hoboken, NJ, USA: John Wiley & Sons, Inc. 2006.

[56] D.S.H. Chan and J.C.H. Phang, *IEEE Trans. Electron Devices,* **ED-31**, 3, 381-383 (1984).

[57] D.S.H. Chan, J.R. Phillips, and J.C.H. Phang, *Solid-State Electronics,* **29**, 3, 329-337 (1986).

[58] D.H. Neuhaus, N.-P. Harder, S. Oelting, R. Bardos, A.B. Sproul, P. Widenborg, and A.G. Aberle, *Solar Energy Mater. Solar Cells*, **74**, 225-232 (2002).

[59] T.B. Stellwag, P.E. Dodd, M.S. Carpenter, M.S. Lundstrom, R.F. Pierret, M.R. Melloch, F. Yablonovitch, and T.J. Gmitter, *Proc. IEEE 21st Photovolt. Specialist Conf.,* 442-447 (1990).

[60] S.R. Lunt, G.N. Ryba, P.G. Santangelo, and N.S. Lewis, *J. Appl. Phys.*, **70**, 12, 7449-7467 (1991).

[61] C. Kirchner, M. George, B. Stein, W.J. Parak, H.E. Gaub, and M. Seitz, *Adv. Funct. Mater.*, **12**, 4, 266-276 (2002).

[62] C.N. Eisler, M.T. Sheldon, and H.A. Atwater, *Proc. IEEE 38th Photovolt. Specialist Conf.,* 937-940 (2011).

[63] M.T. Sheldon, C.N. Eisler, and H.A. Atwater, *Adv. Energy Mater.*, **2**, 339-344 (2012).

[64] S. Bauer, *Nature Materials*, 1-2 (2013).

[65] C. Wang, D. Hwang, Z. Yu, K. Takei, J. Park, T. Chen, B. Ma, and A. Javey, *Nature Materials*, **12**, 899-904 (2013).

[66] R.C. Webb, A.P. Bonifas, A. Behnaz, Y. Zhang, K.J. Yu, H. Cheng, M. Shi, Z. Bian, Z. Liu, Y.S. Kim, W.H. Yeo, J.S. Park, J. Song, Y. Li, Y. Huang, A.M. Gorbach, and J.A. Rogers, *Nature Materials*, **12**, 938-944 (2013).

[67] J.W. Jeong, W.H. Yeo, A. Akhtar, J.J.S. Norton, Y.J. Kwack, S. Li, S.Y. Jung, Y. Su, W. Lee, J. Xia, H. Cheng, Y. Huang, W.S. Choi, T. Bretl, and J.A. Rogers, *Advanced Materials*, **25**, 6839-6846 (2013).

[68] S. Ayazian, V.A. Akhavan, E. Soenen, and A. Hassibi, *IEEE Transactions on Biomedical Circuits and Systems*, **6**, 4, 336-343 (2012).

[69] K.H. Norris, *The Science of Photobiology*, New York, Plenum Publishing Corp, 1977.